University of Kent

Division of Natural Sciences

School of Physical Sciences (SPS)

Riboflavin Derivatives for Sustainable Redox Flow Batteries

By

Koray Gumus

Thesis for the Master of Science by Research

Supervisor: Dr Ewan Clark

Table of Contents

Abstract

Demand for renewable energy, electric vehicles, and sustainability is rapidly increasing, and this demand for more sustainable solutions is driven by the progressively increasing climate issues worldwide. Redox flow batteries (RFBs) are found within renewable energy sources such as wind farms, hydroelectric, and solar power plants where they aid in storing power produced from these sources and distributing it out to the grid when required. Of these, the most commonly used is the vanadium redox flow battery (VRFB) which have been demonstrated to work on an industrial scale since the mid 1980s. However, these systems are now majorly outdated and use harmful and toxic active compounds employed as their electrolytes. These cells can be replaced by newer, more sustainable systems using organic compounds as their redox active electrolytes. With organic redox flow batteries (ORFBs) the scalability and tuneability can go a long way, as the organic active material can easily be adapted to required specifications and parameters a cell requires. This project targeted the synthesis of novel, redox active organic molecules from a biological source (riboflavin) tailored to work in acidic aqueous conditions, with the goal of them being used as a stable and robust electrolyte within a flow cell.

The target molecules were synthesized and studied using electrochemical testing methods including cyclic voltammetry (CV) and flow cell testing to evaluate them as potential electrolytes in an RFB environment, with a sulphonated derivative of riboflavin identified as a promising lead candidate. The research reported here suffered from multiple issues regarding synthesis complication and equipment failure;

these were overcome by adopting alternative methods and principles, as well as a collaboration with an external research group working on similar flow cell studies.

Acknowledgments

First and foremost, I'd like to thank parents, family, and friends for supporting me throughout these challenging 16 months, and specifically to Oni and Orielia for always answering my lab-based questions and providing great company throughout my studies. Thank you to Dr. Alex Murray for providing me with the opportunity to start this project and introducing me to the realm of organic redox flow chemistry. I'd like to give a special appreciation to my supervisor, Dr. Ewan Clark, for always being present and going above and beyond to help me with a problem, no matter how trivial. A massive thank you to Dr. Jennifer Hiscock and her lab group for allowing me to join their weekly small group meetings and providing me with clarity on foggy days. I'd like to thank Hazel and the teaching laboratory for always providing me with equipment and chemicals when I needed them the most. And finally, a huge thank you to Dr. Ana Sobrido and Gengyu Tian at Queen Mary University London for allowing me to work alongside them in their laboratory and for allowing the opportunity of our collaboration.

Abbreviations

^{1}H	Proton (NMR)
^{13}C	Carbon (NMR)
A	Amperes
ACN	Acetonitrile
AORFB	Aqueous organic redox flow battery
C	Coulombs
COSY	Correlated Spectroscopy (NMR)
CV	Cyclic voltammetry
d	Doublet (NMR)
D_2O	Deuterium oxide
DCM	Dichloromethane
DEPT	Distortionless enhancement by polarisation transfer (NMR)
DMF	Dimethylformamide
DMSO	Dimethyl sulfoxide
DMSO-d_6	Deuterated dimethyl sulfoxide
Eqv	Equivalence
Et_2O/ether	Diethyl ether
EV	Electric vehicle
FTIR	Fourier transform infrared (spectroscopy)
g	Grams
HMBC	Heteronuclear multiple bond correlation (NMR)
HSQC	Heteronuclear single quantum coherence (NMR)

Hz	Hertz
h	Hour(s)
IPA	Isopropyl alcohol/2-propanol
J	Coupling constant (NMR)
KO^tBu	Potassium tert-butoxide
LC-MS	Liquid chromatography – Mass Spectroscopy
m	Multiplet (NMR)
mAh	Milliamp hours
MEP	1-Ethyl-1-methylpyrrolidinium bromide
MHz	Megahertz
mol	Mole(s)
mV	Millivolts
m/z	Mass to charge ratio (Mass spectroscopy)
NMP	N-Methyl-2-pyrrolidone
NMR	Nuclear magnetic resonance spectroscopy
RFB	Redox flow battery
RT	Room temperature
s	Singlet (NMR)
t	Triplet (NMR)
THF	Tetrahydrofuran
TLC	Thin layer chromatography
UV-Vis	Ultraviolet light visible spectroscopy
V	Volts
VRFB	Vanadium redox flow battery

W Watts

1. Introduction

1.1 Background of Electrochemistry

Electrochemistry is a discipline of the sciences which dates back to the 18th century,[1] and it is concerned with the association between electrical and chemical events. An electrochemical cell is a device which can transfer charge from one interface (electrode), to another, forming an electrical circuit (see *Figure 1*).[2] Unlike a chemical reaction, the electrons (also including resulting ions) within electrochemical reactions are not transferred directly between molecules but rather *via* their respective conducting circuits.

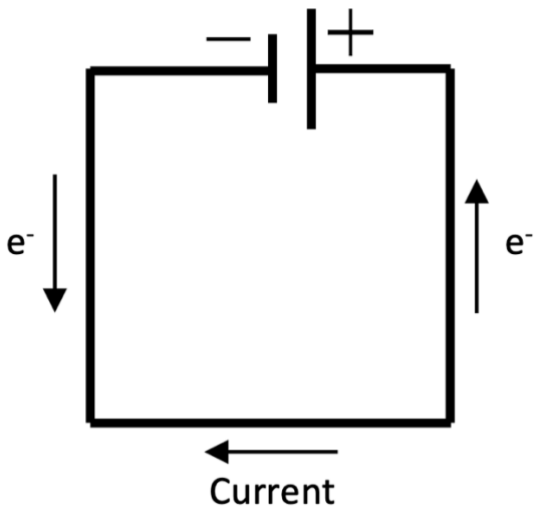

Figure 1 – Figure showing a simplified layout of an electrical circuit (cell), note that the electrons (negative to positive) in a circuit move in the opposite direction along the wire to the applied current (positive to negative).

Electrochemistry studies the chemical phenomena associated with charge separation, and often this is accompanied by a charge transfer in which a cell is complete. Charge transfer can occur homogenously in solution, or heterogeneously *via* electrode surfaces. In practice, for any single ionic solution the sum of negative electrical charges attracted equal the sum of positive charges (electroneutrality), two or more charge transfer half-reactions take place in opposing directions.[3]

1.2 Thermodynamics & Kinetics

Half-reactions are what occurs at the electrodes of a cell, and each half reaction has its own standard electrode potential, $E^{\ominus}$, measured with respect to the normal hydrogen electrode (NHE). By convention, $E^{\ominus}$ is expressed as a reduction potential and describes the ability for a species to reduce that of another species. The cell potential, E_{cell}, is calculated *via* the respective half-reaction using the formula:

$$E_{cell} = E_{right} - E_{left} \quad (Equation\ 1)$$

Where E_{right} and E_{left} are the respective half-reactions occurring at their electrodes, by convention E_{left} is considered to be the 'oxidation' value and E_{right} to be the 'reduction' value. The individual E_{cell} values are calculated from the Nernst equation, which relates the $E^{\ominus}$ with the thermodynamic activities of the redox active species to give an electrode potential, E. The Nernst equation is as follows:

$$E = E^{\theta} - \frac{RT}{nF} lnQ \quad (Equation\ 2)$$

Where, R is the gas constant (8.314 $J.K^{-1}.mol^{-1}$), T is the temperature of the species in Kelvin, n is the stochiometric number of electrons transferred for the calculated process. F is the Faraday constant (96485 $C.mol^{-1}$) and Q is the reaction quotient, which describes the composition of the reaction studied and the relative amounts of products and reactants present at any given time.

The standard potential of a cell, $E^{\ominus}$, can be related to the Gibbs free energy, $\Delta G^{\ominus}$, as follows:

$$\Delta G^{\theta} = -nFE^{\theta} \quad (Equation\ 3)$$

Where all reactants are under standard conditions. The $\Delta G^{\ominus}$ indicates whether any given electrochemical reaction will proceed spontaneously; a negative $\Delta G^{\ominus}$ value indicate a spontaneous reaction.[3]

1.3 Background of Batteries

There are two main categories of batteries (cells): primary and secondary. Primary batteries are single use and undergo an irreversible electrochemical reaction during discharged. Secondary batteries, on the other hand, are re-chargeable; when a reverse current is applied to them in the discharged state, they return to their original charged state. A popular secondary battery found in many aspects of day-to-day life is the Lithium-ion (Li-ion) cell. This class of batteries has been highly engineered and tuned over the years to increase their cycling-life and power densities while reducing

their size to fit in millimetre thin smartphones and other electronic devices. Lithium is a limited natural resource and with the exponential increase in demand since 2010, it is only a matter of time until this finite resource is no longer sufficient to meet demands. For instance, the recent increase in demand for Li-ion batteries for use in electric vehicles (EVs) - which is no doubt a positive step forward towards a greener future enabling a move away from pollutive combustion engines, but this means an increase in demand for the finite lithium sources.[4] In 2017, Tesla was contracted to supply Hornsdale, South Australia with, at the time, the world's largest Li-ion battery (100-megawatt system), with the intended use as an electrical energy storage (EES) device for renewable power sources in the area. Engineering accomplishments like this are extremely impressive, yet the excessive use of a limited resource such as lithium should be preserved for other electronic applications which require a higher power:weight ratios (*e.g.*, EVs and smartphones) when alternative, more sustainable systems, such as redox flow batteries (RFBs) are available for grid scale operations.

1.4 Energy Storage and Redox Flow Batteries

RFBs fall under the category of secondary batteries, as one of their main advantages is that they can be charged and discharged time and time again. The main difference between common secondary cells (such as Li-ion and lead-acid cells) and RFBs is that RFBs work on a liquid electrolyte basis, with the reductive and oxidative electrolyte solutions stored in separate tanks with a membrane divider only allowing useful ions of exchange to crossover. Furthermore, with correct maintenance RFBs can essentially last indefinitely as the only perishable components are the electrodes and membranes. Another benefit which RFBs have over other common secondary

cells (such as Li-ion and lead-acid cells), is that such batteries have the potential to survive a much longer lifespan (10+ years) in their charged, discharged, or in-between (intermediate) states, with no ill effects.[5] This is possible as the electrolytes can be tailored to be stable in both their reduced and oxidized forms. These factors argue for the preferred use of RFBs for static EES devices over that of other conventional storage devices in this category.

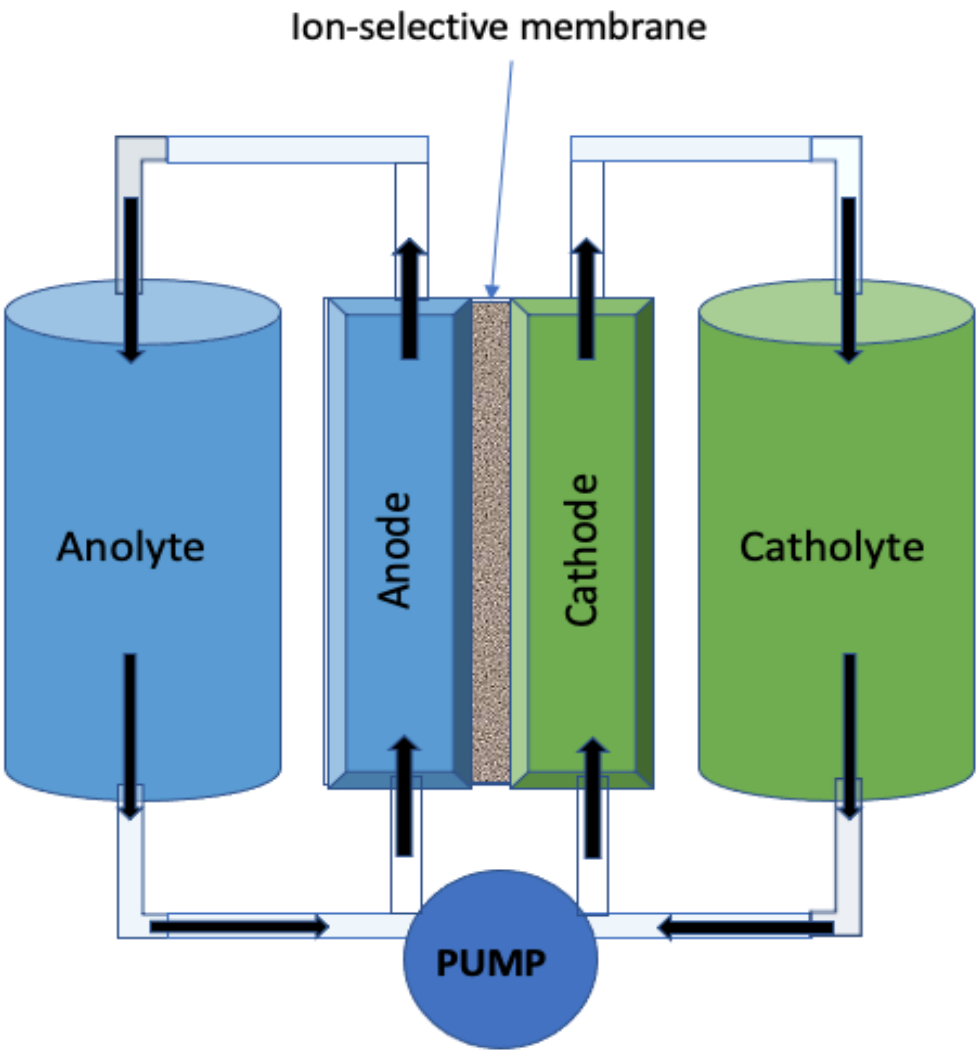

Figure 2 – Schematic showing a simplified layout of a typical RFB.

Solar, wind, and hydroelectric generators are some of the main candidates in the 21st century for renewable, sustainable, and environmentally clean power sources. RFBs are commonly found within these energy source facilities where they act as EES devices. Renewable energy sources are prone to having uneven output electricity due to their irregular and intermittent nature. This is where the benefits of EES devices come into play, serving to stabilize the power output produced and helping to combat power surges from the grid and other sources, ensuring that households and business consumers are supplied with a continuous uninterrupted supply of electricity.

The basic set up of a RFB contain: the positive and negative electrolytes, an ion-selective membrane, current collectors, and electrodes (see *Figure 2*). One of the most enticing attributes of RFBs are that they are fully tuneable and configurable to the environment in which they are stored and used. With these systems, the electrolyte tanks can be enlarged or reduced in size to determine the correct energy capacity and, depending on solubility values, the electrolyte concentration can be adjusted to allow a range of power outputs; this allows for great scalability within these systems. Another appealing attribute is that fluctuations in power demand do not have a negative impact on the RFBs as they can allow charge and discharge rates at variable currents and timeframes. The first mentions of post-prototype RFBs in literature is in the 1970s, by National Aeronautics Space Administration (NASA) which had founded the Lewis research centre with the focus on researching electrically rechargeable redox flow systems.[6] Other appealing attributes of redox flow systems is that they do not require high operating temperatures, they are not limited by cycle

life, and that the reactions are electrochemically reversible unlike that of primary battery systems.

1.5 Vanadium Flow Batteries

The most common RFB found in grid-scale EES facilities are vanadium redox flow batteries (VRFBs). There are predominantly two widely used variations of VRFBs: 1) the all-vanadium cell and 2) the vanadium/bromine cell.[5,7] The all-vanadium system has the advantage that it is of a symmetric cell and so chemical crossover from the positive to negative terminals or *vice versa* does not affect the battery lifetime (see *Figure 3*). The first mentions of a successful working all-vanadium flow battery in literature dates back to 1988, by the university of New South Wales, Australia.[8] This is only the beginning for what has been a long road in progress for the world of robust EES devices. An advantageous attribute of an all-vanadium redox flow system is that the electrolyte tanks can be accidentally mixed and without causing long-term damage as the electrolyte is the same on both sides. Furthermore, the system can be left for extensive periods of time in charged or discharged states without sustaining any adverse effects such as degradation; this is due to the stability of the reduced and oxidized forms of the electrolyte. Though these systems have appealing characteristics for use as EES devices, very few advances have been made to them (with regards to their electrochemical and sustainability properties) since their inception, and modern applications require more environmentally friendly and sustainable alternatives. VRFBs electrolytes are derived from either vanadyl sulphate ($VOSO_4$) or vanadium pentoxide (V_2O_5); these are chemicals which both pose significant health and environmental hazards. They are toxic to the environment with

prolonged exposure and can build up through bioaccumulation of vanadium, a harmful metal in high doses.

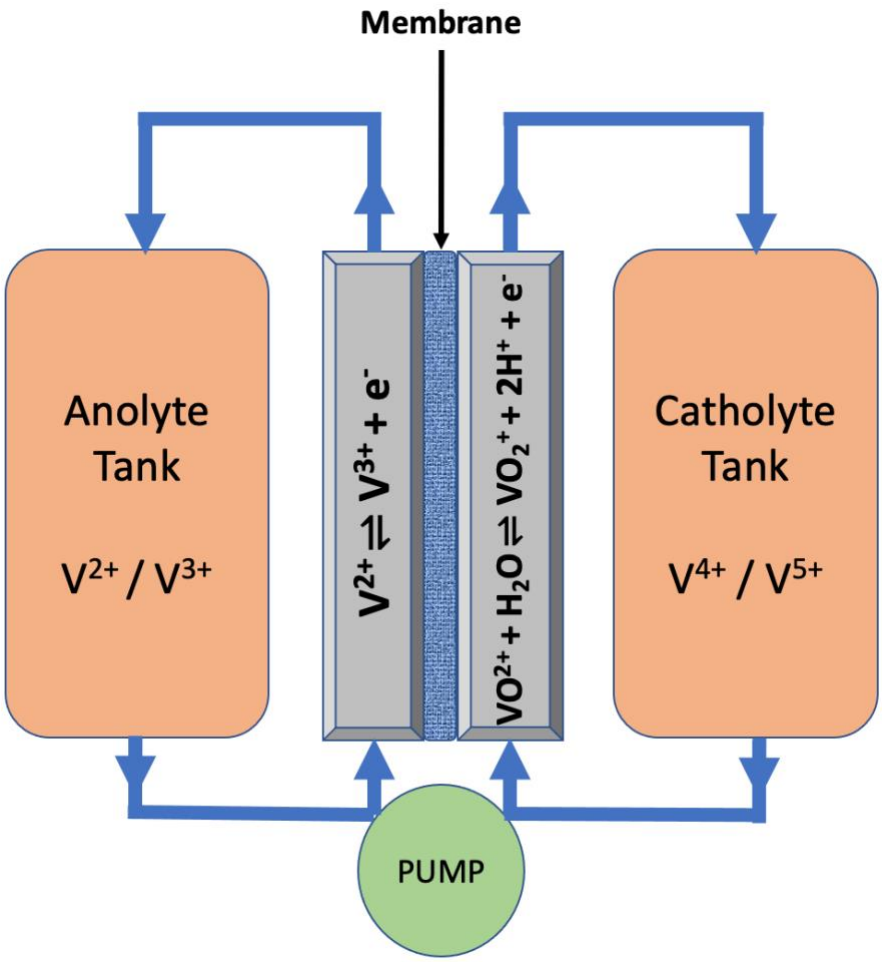

Figure 3 - Simplified Schematic of a VRFB system.

One of the main disadvantages of a RFB system is that they have a lower power density (~10-30 W.h.kg^{-1} for VRFBs)[9] to that of their counterparts (e.g., Li-ion, nickel-cadmium and nickel-metal hydride batteries which are in the region of ~60-265 W.h.kg^{-1}. Li-air batteries have phenomenal theoretical specific energy densities (3505 W.h.kg^{-1}) but these systems only have reported specific energy densities of >500 W.h.kg^{-1} in practice. While these figures are much higher than those of VRFBs and

other lithium-based cells, they require many factors to be controlled for optimal working conditions such as the presence of a gas-handling system to provide dry air for the cell, and the insulation of Li_2O_2 at the positive electrode which have been significant obstacles to optimisation of these systems. Due to challenges of operating in air these systems are usually performed under pure $O_{2(g)}$ conditions (essentially making them Li-O_2 cells).[10] To combat the issue aforementioned for the insulation of the Li_2O_2 electrode, redox active molecules (RAMs) can be employed to the Li-air/Li-O_2 systems to act as a redox mediator/barrier to the air-sensitive electrodes. Organic RAMs are commonly used as redox mediators, typically aromatic or heterocyclic molecules are used as their delocalised π systems have significant stability when undergoing redox processes.[10] The first successful organic RAM mediator in the literature reported a tenfold increase in the capacity life of a Li-O_2 cell with 100 % coulombic efficiency.[11]

1.6 Organic Redox Flow Systems

Moving away from metal based RFBs and into the realm of the more sustainable, aqueous organic redox flow batteries (AORFBs) are seen as greener alternatives.[9] AORFBs use the same principle as that of a VRFBs but replace the metal salts with organic compounds such as vitamin derivatives,[12] quinones,[13,14] and viologens[15,16] (see *Figure 4* for example structures) which tend to possess redox active sites. AORFB systems have only been mentioned in literature from 2010 onwards and represent a new branch of electrochemistry.

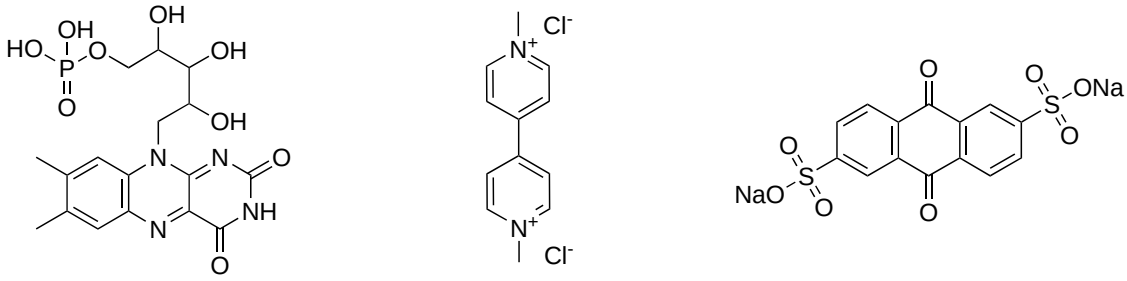

Figure 4 - Flavin mononucleotide (vitamin B_2 derivative), methyl viologen, and anthraquinone disulfonate (AQDS), respectively.

One major advantage of AORFBs over their metal-based predecessors is that organic compounds are highly tuneable and can be tailored to many required parameters. One of these parameters is the supporting electrolyte used in the flow cell, potentially allowing cells to function at a near-neutral or neutral pH, and in a less environmentally damaging electrolyte such as $NaCl_{(aq)}$ rather than the more commonly used strong acids, strong bases, adding to the sustainability aspect of these systems. An example of tuneability and optimization of organic redox compounds is the use of an ion exchange column to replace sodium counter ions with protons to enable an increase in solubility in water. In the literature[17–19] it was found for quinone species (see *Figure 5*) which underwent proton exchange, they could be used at higher concentrations all while producing stable results within the flow cell; this allows the cell to have a much higher power density per litre of electrolyte used.

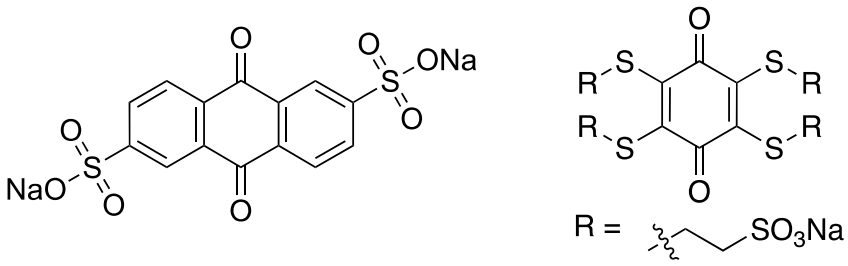

Figure 5 - Aforementioned quinone species from literature, AQDS and MESNa, respectively.

1.7 Electrolytes

The main differences between aqueous and non-aqueous supporting electrolytes for RFBs is that the aqueous conditions are constrained to operate at lower voltages comparted to those of non-aqueous systems; this is due water splitting at higher voltages (<~1.5 V). Non-aqueous systems can perform at much higher voltages (usually between 2 – 4 V and beyond) but suffer the drawback that these systems have poorer ionic conductivity, compared to aqueous systems, and therefore have lower power densities.[20] As with any redox flow system, the ion selective membrane used needs to be suitable for the electrolytes employed, and the nature of the supporting electrolyte solvent used. In non-aqueous systems membranes are often exposed to more harsh conditions to that of aqueous conditions, this in turn has a major impact on the lifetime of the RFB, therefore incurring higher maintenance or initial set up costs for more durable membranes.[21] Building on the challenge of sustainability and greener systems, non-aqueous, organic electrolytes (*e.g.*, THF, DCM, and ACN) tend to be more toxic and hazardous to humans and the environment and therefore using aqueous solvents is safer in this regard.

1.8 Flavins

Riboflavin (see *Figure 6*), more commonly known as vitamin B_2, is an organic compound that is harmless to livestock and the environment. It is commonly found in many foods such as: eggs, almonds, milk, spinach, and various meats. In many countries around the globe, it is a legal requirement that foods such as cereals, breads and flours are enriched with doses of vitamin B_2 to ensure their population receive a healthy recommended dosage of the vitamin.[22]

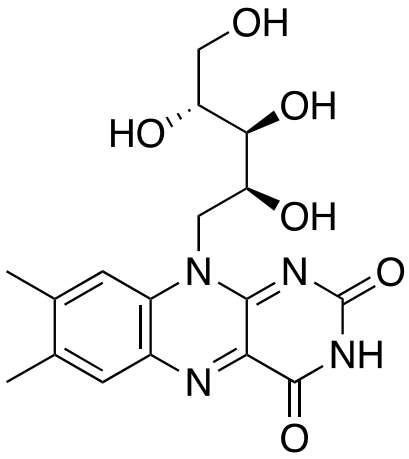

Figure 6 – Chemical structure of riboflavin (vitamin B_2).

The use of riboflavin is not only confined to the world of food processing and nutrition, it has been investigated for cancer treatment - specifically, acting as a mediator of leukaemia cell death.[23] Beyond this, research within the world of electronics has been focused on the use of derivatives of the vitamin in OLEDs (organic light-emitting diodes). It has been shown that a derivative of riboflavin (lumichrome) displays the effective properties in a continuously smooth thin film, a key component within an OLED.[24]

The word ‘flavin’ originates from the Latin word, flavus, meaning “yellow”. This is a very fitting name for this family of compounds as they generally possess a bright yellow/orange colour; this is true for all the compounds synthesized throughout this project (see *Figure 7*).

Figure 7 – Image of lumichrome, a derivative of riboflavin being filtered under vacuum.

1.9 Aims for Project

Consistently active within the field of organic redox flow chemistry are the Aziz group from Harvard university, Massachusetts (USA).[12,14,16,25–28] This project initially aimed at extending their published work, building upon their 2016 Nature Energy paper on RFB systems with an alloxazine based electrolyte.[27] Based on their reports,

initial plans were made to follow this line of research to synthesise novel analogues of alloxazine and lumichrome to produce highly water soluble redox active compounds to be used within a flow cells. This was highly attractive as lumichrome can be readily synthesised from Riboflavin; using a common vitamin source as a potential electrolyte for a RFB would demonstrate powerful sustainability. The initial plans for the 12-month lab period were to synthesise highly water-soluble lumichrome and alloxazine derivatives and study their electrochemical properties with the ultimate goal of producing highly stable and sustainable RFBs. The synthesis of the target derivatives proved more difficult than expected with challenges encountered in pushing reactions to completion and characterization complicated by isomeric compounds and their intricate NMR spectra.

1.10 Aziz Research Group

The Aziz group have a keen background when it comes to the domain of AORFBs. A compound frequently studied within this research group is AQDS (see *Figure 5*) and its derivatives.[25–27] These anthraquinone derivatives possess two carbonyl/hydroxyl positions at which the compound can undergo redox and be utilised as stable soluble couples for RFBs. These derivatives closely marry with the intended research of this project as they have the similarities of both being water-soluble organic species with two redox active sites, which undergo proton coupled electron transfer (PCET). Another great attribute of these organic species is that they can be finely tuned and tailored to the cell conditions, allowing for more freedom of research.[25,27]

Viologen (see *Figure 4*) and ferro/ferricyanide (see *Figure 8*) couples are also studied within this group. Both these compounds undergo single electron redox, varying slightly from the two electron PCET of AQDS, tiron and other similar organic species. Viologen couples can operate at near-neutral pH levels (pH 9) [16] as they do not require proton or hydroxide transfer during redox, allowing organic flow cell couples to present themselves as more environmentally friendly, non-evasive, and adding to the sustainability factor. The organometallic ferricyanide couple also has the potential to be tuned, for example by exchanging potassium counterions with ammonia cations, increasing its aqueous solubility by roughly double, at pH 7.[25]

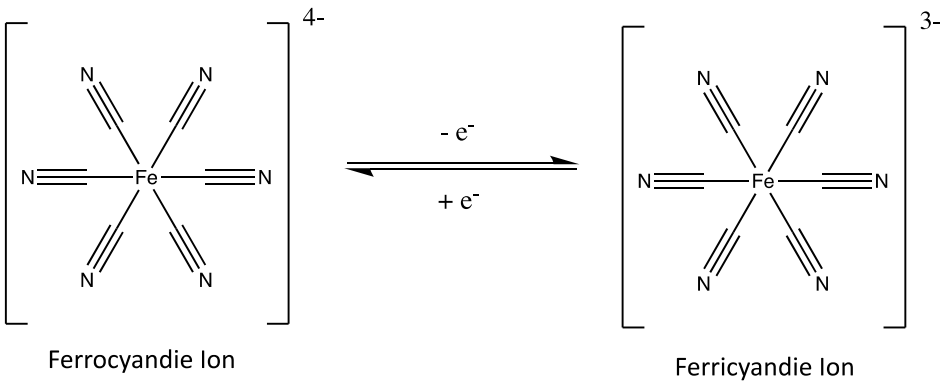

Figure 8 – The structures and redox chemistry of the ferro/ferricyanide ions.

With this group researching both, all-organic cells, as well as organic-inorganic cells, this allowed for various flow cell trails for the target couples synthesised in this project. The HBr inorganic couple [28] was closely followed for flow cell testing, as well as ideas from the organic quinone derivatives.[26,28] The 2016 Nature Energy paper on alloxazine derivates was a key focus on suitable pathways and ideas for synthesizing alloxazine and riboflavin derivatives throughout this project.[27]

1.11 Electrochemical Testing Methods

The key electrochemical testing methods used in this project were cyclic voltammetry (CV) and flow cell testing. CV measures the current response of redox active species in solution to a linearly cycled potential sweep between two or more set values. This method can provide a great understanding of the redox properties of an analyte, determining the rate of electron transfer (current response) and the potential (voltage) at which the compound undergoes an electrochemical change. Voltammetry can be used to determine the electrochemical reversibility of redox processes for tested compounds by analysing the shape and symmetry of the positive and negative sweeps. A typical CV graph of a redox active species presents a 'duck' shaped curve (see *Figure 9)*, this is due to the relationship between the species in question at an electrochemical equilibrium and the Nernst equation (see equation 5 below). Take A and A^+ in redox equilibrium as an example.

$$A \rightleftharpoons A^+ + e^- \quad (Equation\ 4)$$

The Nernst equation describes the equilibrium of the redox species by relating the potential of electrochemical cell (E) to the standard potential of the species (E^θ) and the relative activities of the oxidised (Ox) and reduced (Red) species in the system at equilibrium.

$$E = E^\theta - \frac{RT}{nF} ln \frac{(Ox)}{(Red)} \quad (Equation\ 5)$$

E^{θ} constantly changes as the current sweep is taking place during a CV experiment giving rise to the curve shape formed indicating the potential reduction and oxidation curves (see *Figure 9*). [29,30]

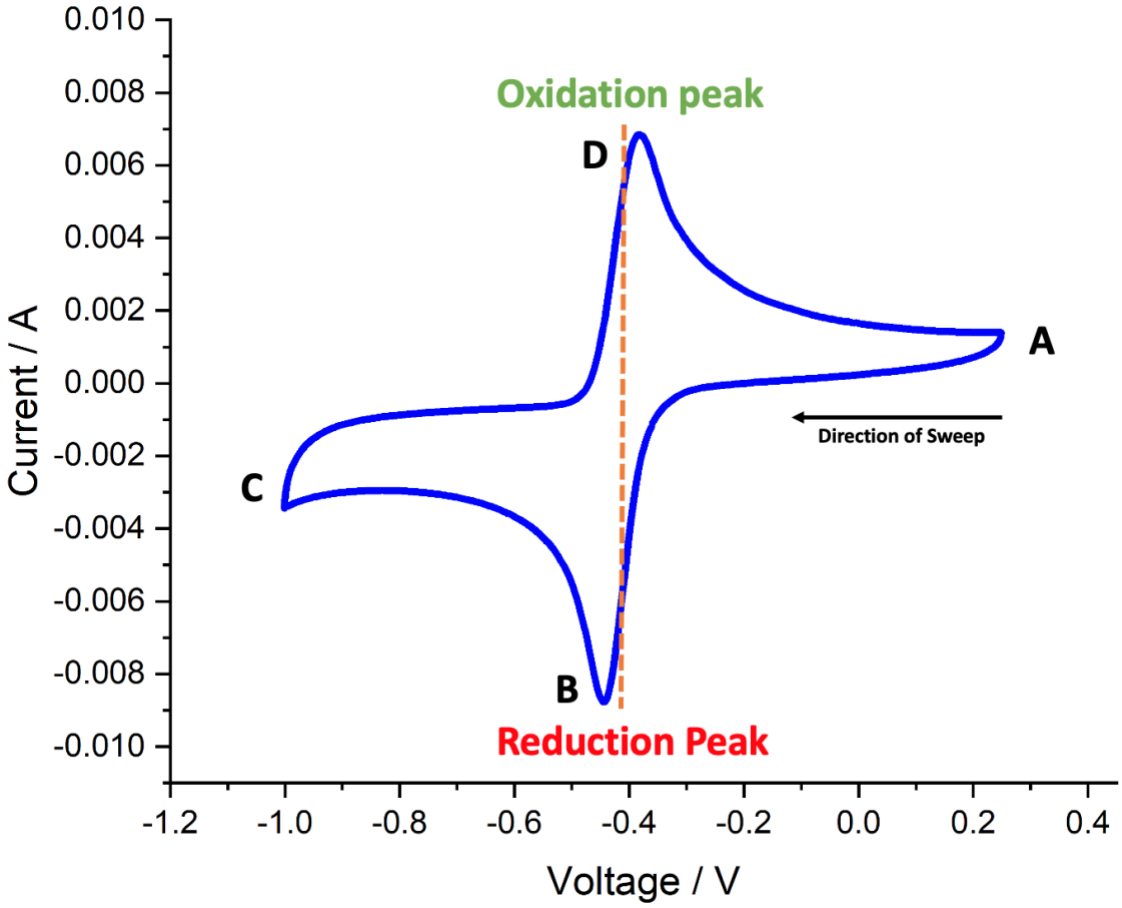

Figure 9 – Example CV graph of an electrochemically reversible species.

Figure 9 illustrates how a redox species behaves during a CV, from point **A** to point **C** the potential sweep is positive (anodic) and carrying on from the example previously, this would illustrate the reduction of A^{+} to A. At point **C** the potential switches to a negative sweep, from point **C** back to point **A** there is a negative potential sweep which would indicate the oxidation of A to A^{+}. The orange dashed line is the half-way point between the turning point of the reduction and oxidation peaks which gives the voltage potential of the analyte. All cyclic voltammetry in this project was

performed using the traditional 3 electrode set-up with a polished glassy carbon working electrode, Ag/AgCl reference electrode, and a platinum wire as the counter electrode (see *Figure 10*).

The difference in potential between the reduction and oxidation peaks is of particular interest when performing CVs, and following the Butler-Volmer and Cortell equations,[31] for an ideal system the equation is given by:

$$E_{Reduction} - E_{Oxidation} = \frac{56.5\ mV}{n} \quad (Equation\ 6)$$

Where n is the number of the electrons exchanged in the analyte, and E_x is the potential observed (in mV) at the turning of the reduction and oxidation peaks respectively.

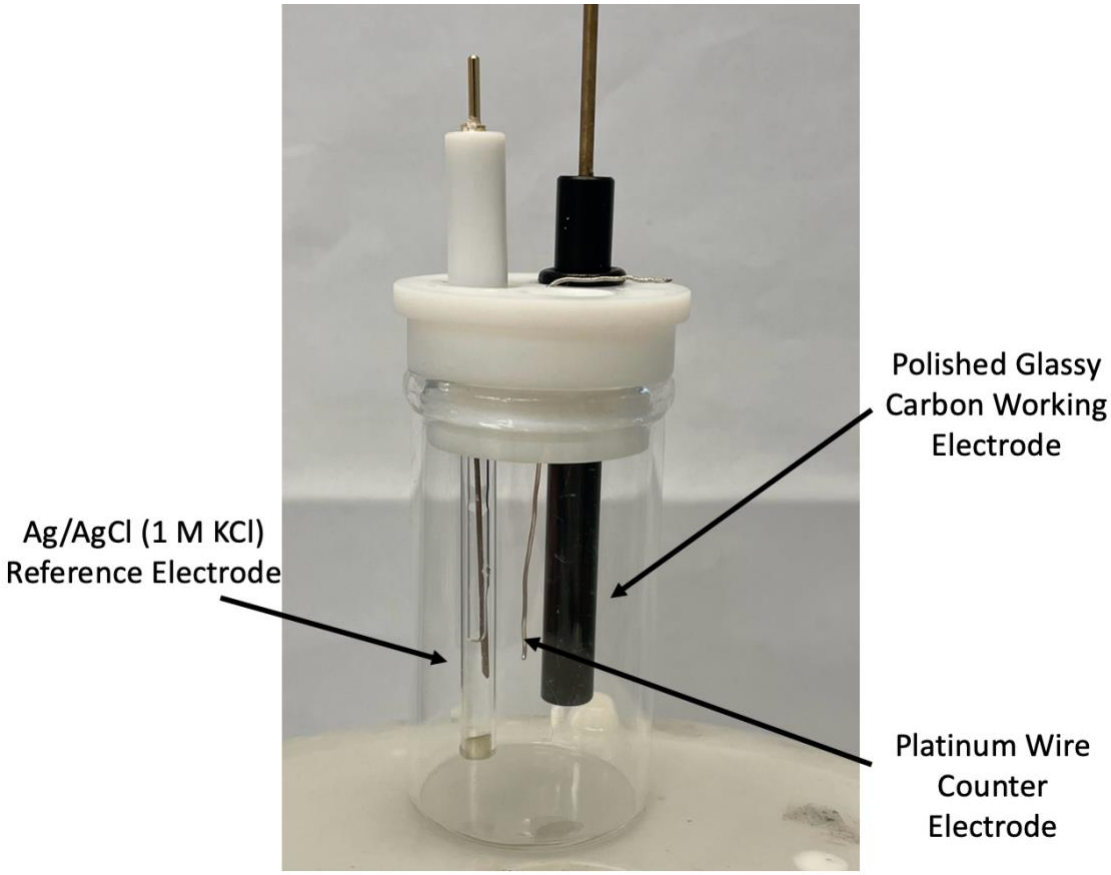

Figure 10 – Image of 3-electrode CV set up used throughout this project.

The other electrochemical testing method used in this project, flow cell testing, works by using a potentiostat to apply a positive and negative currents to the cell which results in the flow cell charging and then discharging respectively. During this time, the applied potential and current are recorded which allows the capacity of the cell and response to load to be determined. (See Chapter 3 and *Figure 23* for detailed information of the system). A useful characteristic determined from a flow cell test is the coulombic efficiency which is the percentage proportion of discharge time over charge time for a cell operating at constant current; for a well performing cell this value should be as close to 100 % as possible during all cycles. Another characteristic

is the observed capacity compared to that of the calculated theoretical value, this can be calculated in coulombs per gram ($C.g^{-1}$) of active material using the equation:

$$Q_{theoretical} = \frac{nF}{MW} \quad (Equation\ 7)$$

Where n is the number of electrons being transferred, F is the Faraday constant, and MW is the molecular weight of active redox substance being used in the cell. This is a highly important factor to consider for economically viable RFBs as the closer the experimental value is to the theoretical value, the more efficient and cost effective the flow cell will be.

2. Experimental and Synthesis

2.1 Synthetic Routes to Obtaining Lumichrome

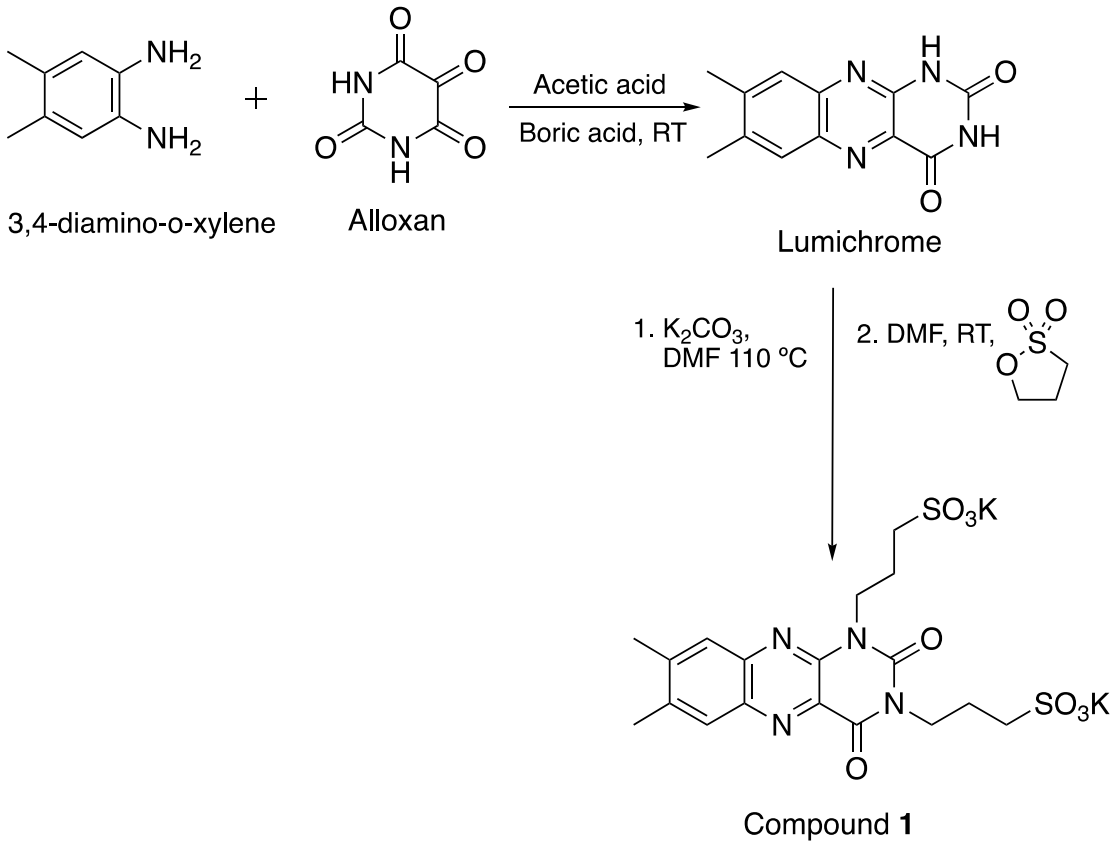

*Figure 11 – initial synthetic method used in attempts to synthesise compound **1**.*

From the literature[32] it is known that the synthesis of lumichrome from alloxan and 3,4-diamino-o-xylene (see *Figure 11*) has shorter reaction times (~12 hours) than that of cleaving the sugar chain of riboflavin using $NaIO_4$ (~18 hours). However, the alloxan synthetic route is a more expensive one with alloxan at ~£325/mol and 3,4-diamino-o-xylene at ~£1247/mole. The cleaving of the riboflavin sugar chain is more cost effective and has proven to consistently give high yields of ~85 % (see methods section below) and only takes an extra 5-6 hours in theory. Furthermore, in practice, the alloxan route was found to be difficult to drive to completion and required

resubjecting the crude product to additional starting materials to push it to completion, making this route unattractive. Lumichrome is commercially available as a reagent, but it can cost around £26,645 per mole, which is a very high price point. Rather, by synthesizing lumichrome *via* the cleaving of riboflavin's sugar chain in water (see *Figure 12*), costs can be kept down as the only costly reagent is $NaIO_4$ at ~£215/mol and riboflavin at ~£131/mol, see methods section of **lumichrome** for detailed methodology.

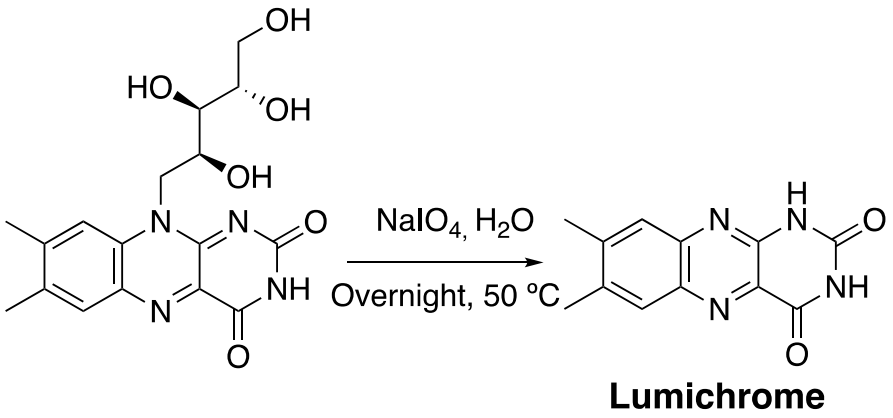

Figure 12 – Synthetic route for sugar chain cleavage of ribflaovin to give lumichrome.

Obtaining lumichrome from riboflavin is not just limited to traditional chemical reactions, it can also be synthesized *via* an enzymatic reaction of bacteria at a neutral pH with a high yield of 96 %.[33] Another possible route of obtaining lumichrome is through the photodegradation of riboflavin,[34] making these two alternative routes a more sustainable and effective way of obtaining lumichrome from the vitamin source and possibly eliminating the use of $NaIO_4$ which is the most costly reagent used in our synthesis of lumichrome.

2.2 Initial Synthetic Ideas

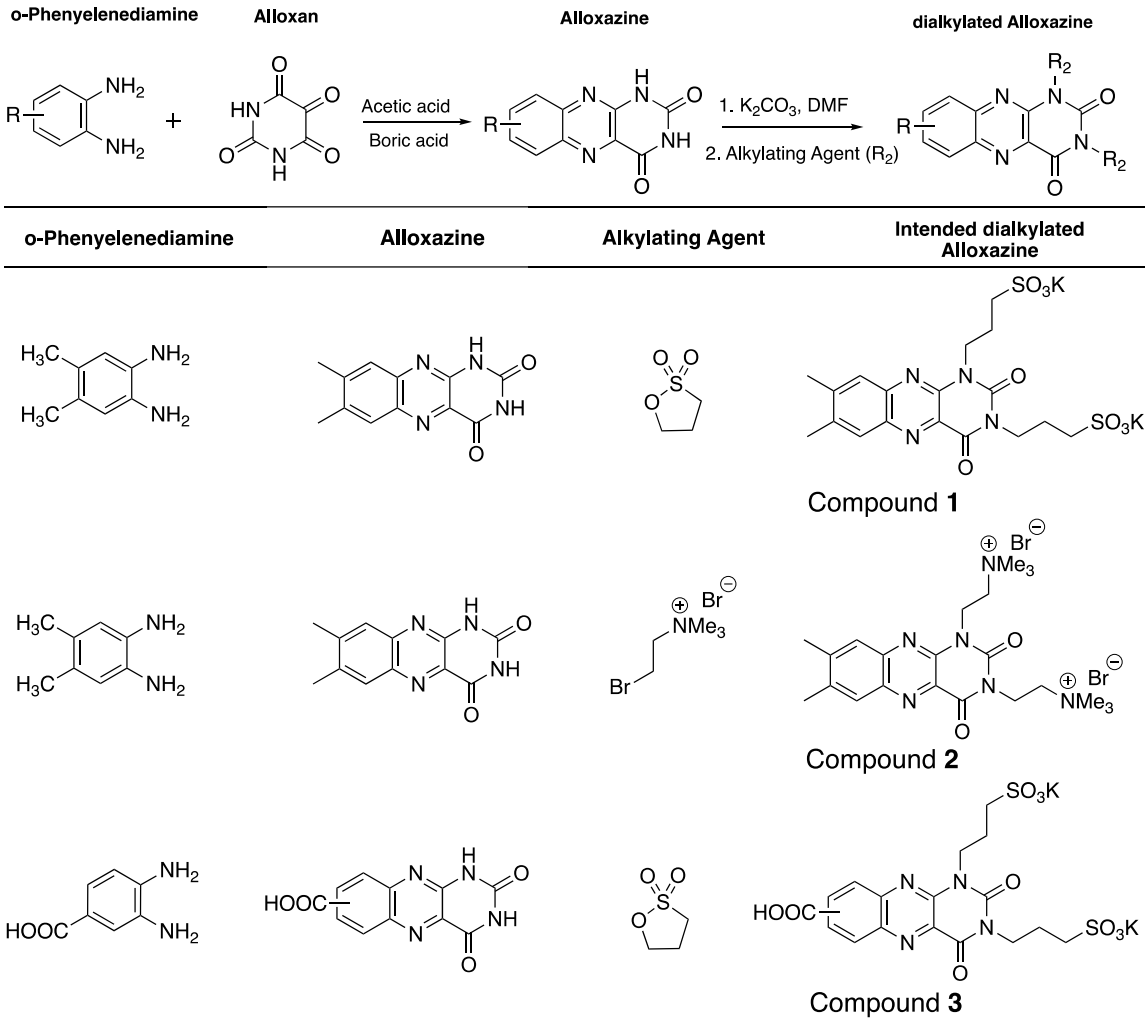

Figure 13 – Initial proposed synthetic routes to follow for scope of the project.

Previous work in the group towards another water-soluble, dialkylated derivative of lumichrome explored the use of bromocholine bromide (see compound **2**, *Figure 13*).[35,36] This synthetic route followed the same methodology and conditions for that of the alkylation with propane sultone (see compound **1**, *Figure 11*). This had the same issue with the final step in which the alkylation did not go to completion and the residual lumichrome intermediate could not be easily removed with a simple hot ethanol wash. Given early success with Soxhlet extraction for **1**, the same process was

repeated for this one. However, post Soxhlet extraction, attempts to analyse the product by NMR sample were unsuccessful as the results were insoluble in D_2O (compound **2** is highly soluble in water); d^6-DMSO was instead required. From this, it was concluded that the product is not thermally stable. Upon further analysis, the NMR spectrum recorded in d^6-DMSO confirmed the loss of the alkyl chains as the spectrum was identical to that of the lumichrome intermediate. Earlier attempts to speed up the formation of **2** by heating the reaction at around 50 °C for the final alkylation step were unsuccessful; this may provide the reason.

Compound **3** was another derivative inspired by the synthetic methodology of Lindén *et al*.[37] Characterization of this compound was complicated by the existence of two isomers (see *Figure 13*). Furthermore, the same issue of incomplete reaction was found in this case as well. However, as the two isomers are not synthesized in an equal ratio, the NMR spectra are very complex with overlapping signals, making it hard to determine whether the reaction had gone to completion, or if there were still partially alkylated intermediates present. This issue was intensified for the final alkylation step with propane sultone. For these reasons, and following identification of a cheaper and more time-effective route towards the lumichrome backbone, this synthetic idea was not continued.

Initial attempts to synthesise the lumichrome derivative, **1**, which formed the focus of this project followed the synthetic methods from the literature.[32,36,38] This initially started with a 3-step reaction of synthesizing lumichrome *via* alloxan (see compound **1,** *Figure 13*), followed by deprotonating the lumichrome intermediate

with K_2CO_3, and finally a simple dialkylation of the sulfonic acid chains with propane sultone. This route proved to be problematic in several ways. Firstly, it was found that neither the 1st nor 3rd steps of the reaction were going to completion, and so the crude products were consistently having to be resubjected to the reaction conditions, consuming further reagents and solvent. Prolonged reaction eventually allowed the first step to go to completion after roughly six days of a stirred reaction, but issues persisted with the final step of the reaction which did not go to completion. NMR analysis of the product consistently showed ~15 % of lumichrome intermediate still present in the crude product, and this was not being alkylated regardless of how much excess propane sultone was used (up to 12 eqv).

2.3 Cleaning Procedures

During initial attempts to remove the unwanted lumichrome intermediate, the powder was washed with copious amounts of hot EtOH following the literature precedent.[36] This procedure was unsuccessful, removing only a small quantity of intermediate impurity (<1%). As simple washing was unsuccessful, a Soxhlet extraction was attempted. After Soxhlet extraction in EtOH for 48 Hours, NMR analysis indicated that this cleaning process was slowly working giving about a 2 % improvement in purity. The extraction process was repeated a further two times with similar results each time attending with around 10% impurity remaining. Repetition of the Soxhlet extraction this time with a 4:1 mix of EtOH:MeOH over 4 days was attempted. This process was more successful and removed a further ~4 % of the impurity (~ 6 % impurity remaining) and was repeated for a further 10 days until the NMR spectrum showed a <1 % amount of the lumichrome intermediate. While this

Soxhlet extraction with a 4:1 ratio of EtOH:MeOH worked, it was a highly wasteful and time-consuming route, requiring a 3-week period of constant reflux and ~3 litres of solvent for only 5 g of product cleaned; an alternative route was needed.

As well as the residual partially alkylated intermediate impurity, upon further analysis of the NMR spectra, peaks were identified which did not correlate to any solvents or reagents used within the reaction; these were unaffected by the alcohol extraction. Initially, small, test-scale washes were attempted with common bench-top solvents such as IPA, THF, hexane, chloroform, acetonitrile, MeOH, ether and toluene. These were not successful in removing the impurity, nor allowing it to be isolated for independent analysis. The solvents were individually combined with a sample of the crude powder in a vial, heated gently and sonicated to see the effects if any the solvents had on the powder. ^{1}H NMR spectra of both the solid and residual solvent from each test sample were taken, yet none of the acquired spectra showed any positive indications that the impurity was being washed out and that all the solvents were mostly immiscible with the crude powder.

2.4 Impurity Troubleshooting

Given unsuccessful isolation of the impurity, the NMR of the mixture was carefully studied to identify the impurity and how it formed. The impurity gave rise to highly coupled aliphatic signals, and initially it was expected to form from propane sultone ring opening or DMF decomposition. Notably, the impurity gave rise to a sharp singlet around 3.1 ppm (see *Figure 14*) which could have been due to the presence of

a HN-C**H₃** or **H₃**C-NC**H₃** fragments. However, the signals of the relevant impurity peaks did not match the splitting pattern for that of an alkyl chain.

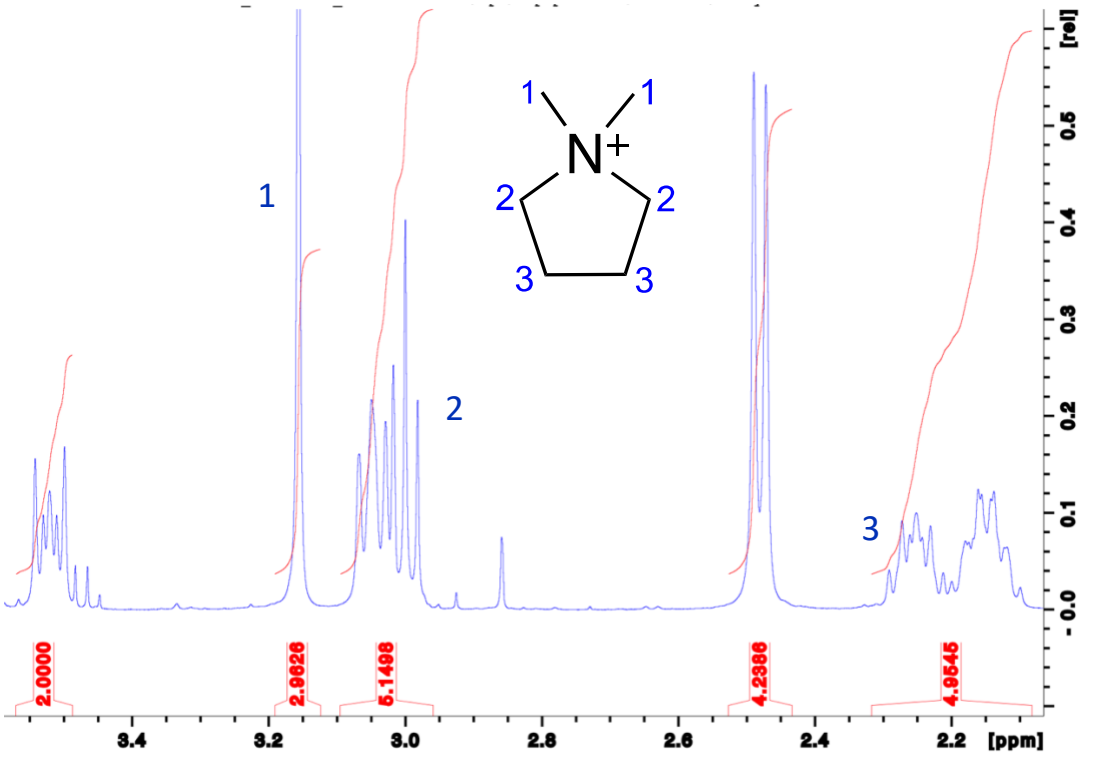

*Figure 14 – Magnified ^{1}H NMR spectra of crude compound **1** including overlapping impurity peaks.*

As DMF is known to be nucleophilic at oxygen, the possibility that DMF was undergoing alkylation by propane sultone was considered. However, this was ruled out as a reaction of propane sultone in DMF was tested under the same conditions and showed no reaction. However, a reaction of DMF and propane sultone with base, K_2CO_3, led to formation of all relevant impurity peaks in the correct integration pattern. The unwanted impurity is thus formed by a base-induced reaction between propane sultone and DMF. The coupling pattern was found to be consistent with the formation of the N,N-dimethylpyrrolidinium cation (see *Figure 15*); the ^{1}H and ^{13}C NMR are consistent with the literature.[39]

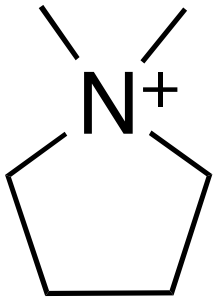

Figure 15 – Structure of suspected impurity formed due to DMF, propane sultone and base interaction.

2.5 Optimising Reaction Conditions

Having identified the cationic impurity, it was recognised that excess K_2CO_3 from the initial deprotonation step was likely the root cause. The synthetic route was known to retain considerable K_2CO_3 (see *Figure 11*) as DMF is not able to wash out the excess base. Water would dissolve the residual base, but this was not an option as the deprotonated intermediate was highly water soluble. The organic-solvent soluble base, KO^tBu, was chosen as a strong, non-nucleophilic base with good solubility in DMF and it is also highly soluble in alcohols such as IPA and EtOH which could easily be used to wash out excess base from the intermediate. It was hoped that this method would eradicate the issue with the base-inducted reaction of DMF and propane sultone. As this was a strong base, the issue of the addition of it to the reaction conditions was highly exothermic and so it had to be added slowly and portion-wise, especially for large-scale reactions. The initial test reactions using 2 equivalents of KO^tBu did not go to completion but use of 3 equivalents did, and the final step of the alkylation was performed. Unfortunately, the cyclic impurity could still be seen in the NMR spectrum coupled with large amounts of singly alkylated product. It was concluded that the base is thus necessary for complete alkylation and that the issue

was the use of DMF; it also suggested that the deprotonation and alkylation could be carried out in a single step, streamlining the synthesis.

Attempts to replace DMF with DMSO as a polar, aprotic solvent were unsuccessful – during an initial test reaction using DMSO and KO^tBu, the base reacted violently with the solvent forming a viscous black solution. The next attempt with DMSO was a one-pot, *in-situ* deprotonation with K_2CO_3 heated at 60 °C for 10 days. Since both the intermediate and product are DMSO soluble, EtOH was used to precipitate the product, and this was advantageous as the product would normally be washed EtOH. This reaction was successful, with all the relevant peaks present within the ^1H NMR spectrum, but there were issues of excess DMSO remaining in the product.

As DMSO has a higher price point than most common bench-top solvents and given the need for large quantities (20+ grams) of **1**, an alternative solvent to DMF and DMSO was sought. NMP was chosen as belonging in the same class of polar, aprotic solvents, and of low cost as it is frequently used for many industrial-scale purposes.

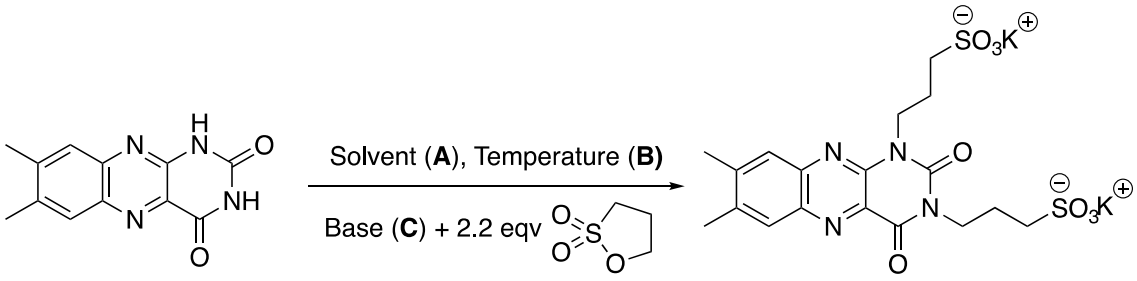

Lumichrome Compound **1**

Solvent (A)	Temp / °C (B)	Base (C)	Outcome
DMSO (15 cm^3)	60	K_2CO_3 (2.2 eqv)	Successful, 5 % intermediate and 3% singly alkylated form observed in NMR. Wet with solvent.
Reline (10 cm^3)	60	K_2CO_3 (2.2 eqv)	Unsuccessful, no relevant peaks observed in NMR
NMP (10 cm^3)	60	K_2CO_3 (2.2 eqv)	Successful, 3 % of singly alkylated form observed in NMR. Wet with solvent.
NMP (1 cm^3)	60	K_2CO_3 (2.2 eqv)	Unsuccessful, ~50 % singly alkylated form observed, insufficient solvent.
NMP (2 cm^3)	60	K_2CO_3 (2.2 eqv)	Successful, 3 % of singly alkylated form observed in NMR. Wet with solvent.
NMP (2 cm^3)	60	KO^tBu (2.2 eqv)	Successful, 10 % of singly alkylated form observed in NMR. Wet with solvent.
NMP (3 cm^3)	90	K_2CO_3 (2.2 eqv)	Successful, but unknown impurities observed.
NMP (3 cm^3)	60	KO^tBu (3 eqv)	Successful, 3 % of singly alkylated form observed in NMR. Wet with solvent. Product appeared to be 'burnt'. Dark brown in colour.
DMSO (3 cm^3)	75	KO^tBu (3 eqv)	Successful, wet with solvent, ~1 % singly alkylated form observed, Product appeared to be 'burnt'. Dark brown in colour

Figure 16 – Table presenting reactants and results of one-pot, NMR-scale test reactions performed on lumichrome.

Many NMR-scale reactions were trialled at various conditions (see *Figure 16*) using different solvents, different reaction conditions and quantities of reagents each time; all test reactions were performed on a 100 mg lumichrome scale and reacted overnight. From these results it can be seen that DMSO and NMP are suitable replacements for DMF, and that the reaction can be carried out in one pot with no need for a separate deprotonation step, reducing the reaction time by hours. KO^tBu was found to be unsuitable in both the NMP and DMSO based reactions as the base reacted violently when added and essentially 'burned' the final product. From these experiments, it was also found that for NMP, 2 cm^3/100 mg of lumichrome was the minimum amount of solvent needed. Although both the DMSO and NMP reactions were successful with both bases, ultimately NMP with K_2CO_3 route was used for two reasons. Firstly, NMP is much cheaper than DMSO; at time of test reactions DMSO was ~£110/litre and NMP was ~£25/litre, allowing for huge financial savings on scale-up. Secondly, the use of K_2CO_3 over KO^tBu was decided as while both were proven to successfully deprotonate lumichrome, using K_2CO_3 meant there was no issue of a highly exothermic reaction when adding the base. Furthermore, there is no need to slowly add K_2CO_3 portion wise, saving over an hour of time on a bulk-scale reactions.

Having solved the issue of formation of DMF-derived by-products, attention was turned to removing the remaining singly alkylated impurity. Since a simple solvent wash of the crude powder did not remove this impurity, and nor did a Soxhlet extraction, alternative cleaning methods were attempted. Despite extensive testing of common laboratory solvents and mixtures, no separation was observed by TLC, and

it was concluded that the two compounds that were too alike to be separated out through a column. Recrystallisation conditions were thus sought.

As synthesizing the product in DMSO and precipitation with EtOH did not remove the presence of singly alkylated product, DMSO was determined not to be suitable for recrystallization. This left water as the only solvent in which the product was appreciably soluble. Attempted recrystallisation in the minimum amount of water at reflux was unsuccessful, and the same impurities were observed when the compound recrystallized. Since it was known that both the impurities and desired product have limited solubility in MeOH and EtOH, a recrystallization with the aid of antisolvent (with respect to the desired product, compound **1**), to keep the impurity in that solvent environment was trialled. This was successful, exploiting EtOH as the anti-solvent used, with MeOH used to help fully remove any residual K_2CO_3. Furthermore, the use of water to recrystallise compound **1** was beneficial as it is fully miscible with NMP and so helps to remove the high boiling point solvent very easily.

2.6 Methods

Lumichrome:

Lumichrome was prepared using a modification of the literature route.[38] Riboflavin (12.00 g, 31.89 mmol) and $NaIO_4$ (19.10 g, 89.30 mmol) in H_2O (480 cm^3) were stirred at 50 °C overnight (~18 hours). The reaction mixture was left to cool and sodium sulphite (approx. 18 g) was added portion wise to the stirred dark brown solution until the colour had changed to a bright orange solution. The solid was isolated by filtration and washed with H_2O (50 cm^3) and MeOH (50 cm^3). The solid was

dried oven-top to give lumichrome as a yellow powder (6.3 g, 82 %). This method varies from the literature [38] by removing iodine with sodium sulphite rather than washing with large quantities of MeOH. ^{1}H NMR matches that of the literature [40] (see *Figure 54* for ^{1}H spectrum).

Compound **1:**

Lumichrome (2.50 g, 10.32 mmol) and K_2CO_3 (3.54 g, 25.58 mmol) were combined in NMP (55 cm^3) and stirred at 60 °C for 30 minutes. Propane sultone (2.26 cm^3, 25.80 mmol) was added to the stirred reaction mixture and stirring continued at 60 °C for a further 18 hours. The suspension was quenched with MeOH (30 cm^3), filtered, and the isolated solid washed with hot MeOH (10 cm^3). The crude solid was dissolved in minimal amount of H_2O to afford a saturated solution (approx. 2 cm^3/g) and heated to reflux for 5 minutes. MeOH (15 cm^3) was added to the stirred solution and H_2O was added dropwise until all the solid was fully dissolved. EtOH was then added portion wise (approx. 40 cm^3) until slight turbidity was observed; at which point a few more drops of H_2O were added to give complete redissolution. The solution was maintained at reflux for a further 10 minutes, after which the heating and stirring were turned off and the solution allowed to attain room temperature slowly. Once cool, the flask was then stored at 4 °C overnight to induce recrystallisation. The resultant suspension was filtered and air dried, and the cleaning process proceed was repeated once more. The isolated solid was washed with hot EtOH (25 cm^3) and was dried under vacuum at 100 °C to give **1** as a yellow solid (2.90 g, 5.15 mmol, 49.9 %). ^{1}H NMR (400 MHz, 26.9 °C, D_2O) δ: 2.08 (m, 4H), 2.40 (s, 3H, ArC**H$_3$**), 2.42 (s, 3H, ArC**H$_3$**), 3.00 (m, 4**H**), 4.10 (t, *J* = 7.03 Hz, C**H$_2$**), 4.23 (t, *J* = 7.03 Hz, C**H$_2$**), 7.56 (s, 1H, Ar**H**), 7.57 (s, 1H,

Ar**H**); ^{13}C {^{1}H} NMR (100 MHz, 26.9 °C, D_2O) δ: 19.41 (s, CH_3), 20.07 (s, CH_3), 22.45 (s, CH_2), 22.56 (s, CH_2) 41.30 (s, CH_2), 41.35 (s, CH_2), 48.48 (s, CH_2), 48.53 (s, CH_2) 126.00 (s, **C**-CH_3), 127.02 (s, CH-**C**-N), 127.24 (s, **C**-CH_3), 137.54 (s, CH-**C**-N), 141.66 (s, CH), 141.71 (s, CH), 143.50 (s, N-**C**-C=O), 147.13 (s, N-**C**-N), 150.41 (s, N-C-**C**=O), 160.30 (s, C-N-**C**=O) (see *Figure 48-49* for full NMR characterization spectra of **1**). FTIR: ν = 3482 (water stretch), 1715, 1668 (conjugated C=O stretch), 1553, 1479, 1460 (aromatic C=C stretch), 1387 (methyl C-H stretch), 1360, 1180 (sulfonic acid S=O), 1042 (N-H stretch), 791, 733 (aromatic C-H stretch) (see *Figure 56* for spectrum). Mass Spec (ESI^-): m/z, [MH^-] calc 485.1, found 484.9 (See *Figure 57).* UV-Vis data for **1** show in appendix 1 below (see *Figure 58*).

CHN analysis was performed on **1**, the results are shown below at *Figure 55*, showing that **1** recrystallises from water with 3.5 waters of crystallisation. Mass spectrometry showed the parent ion and fragments are consistent with the loss of one and both alkyl chains. The melting point of **1** is greater than 300 °C and so the true melting point data is not available as the apparatus used to determine this value only ramped up to 300 °C.

3. Testing of Electrochemical Properties

3.1 Redox Background of Compound **1**

Once the novel riboflavin derivative, **1**, was successfully synthesized and free of impurities, its electrochemical properties were tested to see how it would behave as an electrolyte in an AORFB system and perform under battery-like conditions as a negative couple. Compound **1**, like AQDS, a disulfonic acid analogue of anthraquinone (see *Figure 27*) undergoes a 2-proton, 2-electron, proton coupled electron transfer (PCET) (see *Figure 17*) making it a potential candidate to be the anolyte (negative couple) for a flow cell.

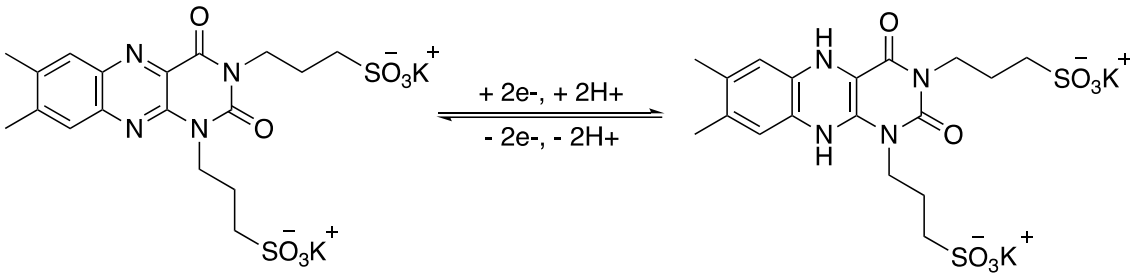

*Figure 17 – Illustration of the PCET electrochemical process **1** undergoes.*

A crucial aspect which needed to be taken into consideration when choosing a couple to partner with **1**, is that for every electron and accepted on one electrode there must be a corresponding number of electrons donated from the opposite electrode, two electrons in this case. The same rule applies for the number of protons accepted to protons donated during a redox process (see *Figure 17*).

3.2 CV Testing of Compound 1

This voltametric procedure reveals if the reduction of **1** is electrochemically reversible, and if so, gives the voltage (potential) at which this process occurs. This is highly useful information when deciding what type of couple **1** can be used against and determines the potential window for the full flow cell and where the voltage cut-off will need to be set for flow cell testing.

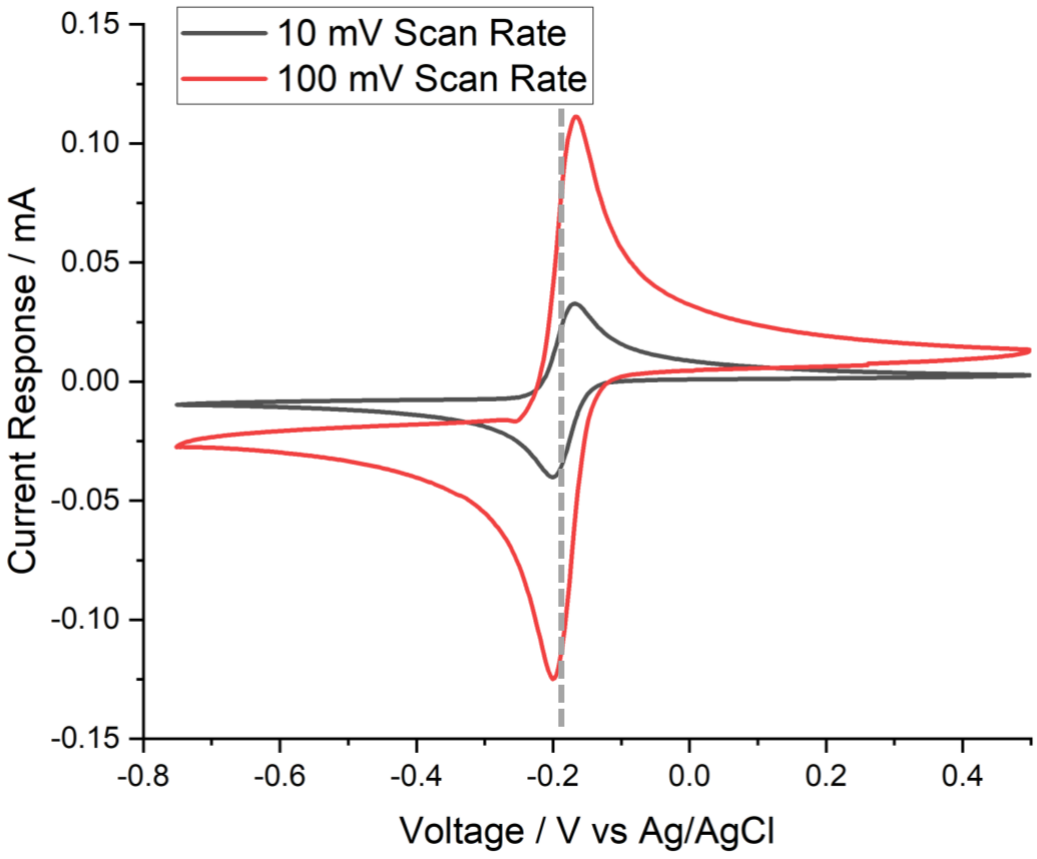

*Figure 18 – CV graph of 0.005 M **1** (0.028 g) in 1 M H_2SO_4 (10 cm^3) degassed with $N_{2(g)}$ at two different scan rates.*

CV data *(Figure 18)* shows that **1** is electrochemically reversible in an acidic supporting electrolyte solution (at ~pH 0), with both the oxidation and reduction peaks in the CV appearing to be highly symmetrical and with minimal separation (34

mV separation between redox peaks, close to the ideal value of 28 mV for a 2-electron process), indicating that **1** would be a good redox couple in a flow cell. From the graph it can be seen that **1**'s redox potential in a 1 M H_2SO_4 environment (~pH 0) is - 0.183 V *vs* Ag/AgCl (1 M KCl), which is 0.052 V *vs* NHE, comparing this directly to a CV of AQDS in 1 M H_2SO_4 which has a reported potential of ~0.2 V *vs* NHE.[41]

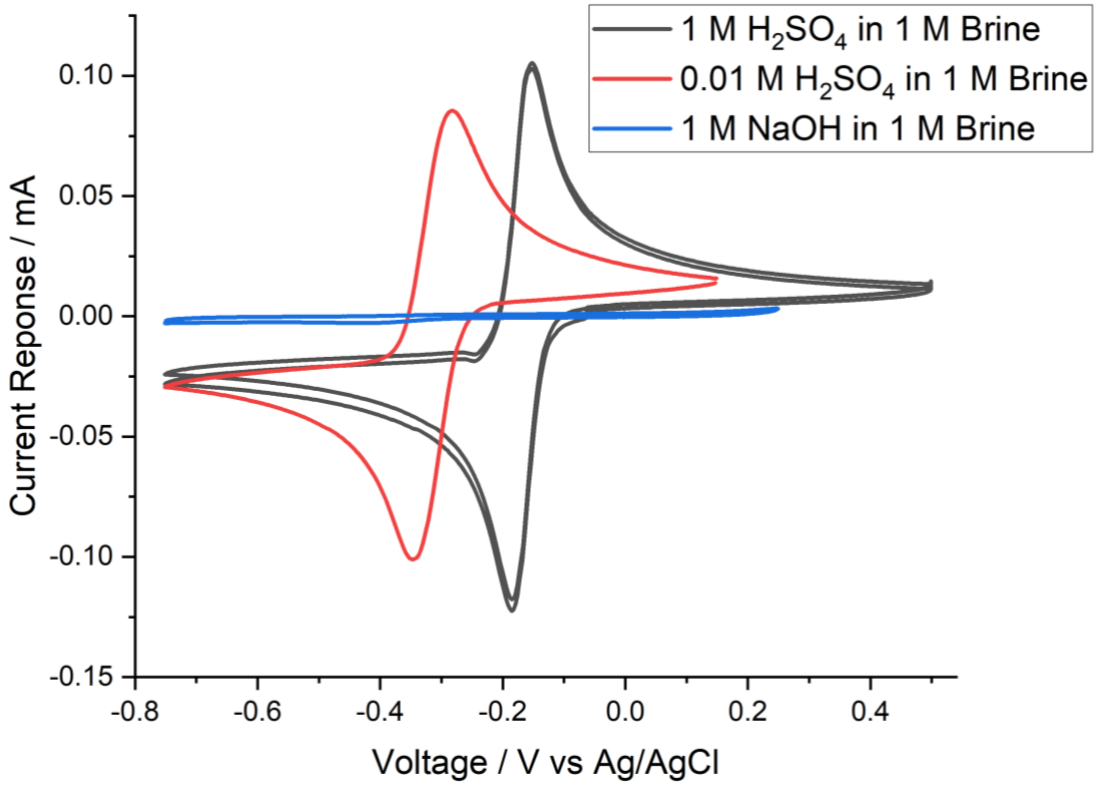

*Figure 19 – Multiple CV graph, all containing 0.005 M **1** (0.028 g) degassed with $N_{2(g)}$ taken at 100 mV/s scan rate.*

Attempts to perform CV studies for **1** across a full pH range (pH 0 – pH 14) to determine how it behaves at different pH levels were hindered by a faulty pH meter; the study will be conducted by other group members prior to publication. In place of this, a CV study of **1** in acid (1 M H_2SO_4 in 1 M $NaCl_{(aq)}$), brine (1 M $NaCl_{(aq)}$) and base (1 M NaOH in 1 M $NaCl_{(aq)}$) was performed. As it can be seen from the graph (*Figure*

19) no oxidation or reduction peaks were visible in the CV of the brine solution with NaOH. Instead, the brine with NaOH test was spiked with a small amount of the acid solution to see what effect this would have on the voltammogram. As expected, the led to reappearance of the reduction wave because **1** undergoes a PCET (see *Figure 17*), a reasonable concentration of free protons in the supporting electrolyte is therefore essential for the species to undergo reversible reduction. It can be seen from the plot that **1** in this electrolyte (approximate pH 4) has a more negative redox potential than that of it at pH 0 (the black lined CV), as expected from the Nernst equation. As for the NaOH test, there is no presence of an oxidation peak, but a small hump can be seen in the reduction peak region for it. Given the lack of a reversible reduction wave at neutral pH, this is unlikely to arise from **1** itself. This may therefore indicate that **1** has undergone an undesirable chemical change, likely reaction with the base resulting in dealkylation and cleavage of the sulfonic acid chains of **1**, possible *via* the Hoffman elimination,[42] commonly seen with strong bases.

In order to understand what chemical changes may have been happening with **1** when in basic conditions (NaOH), timed NMR experiments with **1** in 1 M and 0.01 M NaOH in 1 M NaCl were analysed, with **1** in 1 M NaCl solution and lumichrome in a 1 M NaOH solution as controls (see methods below for detailed methodology). It was apparent from the ^{1}H NMR spectra of the 1 M NaOH timed sample that **1** was undergoing an adverse reaction as the 2 aryl proton peaks were disappearing and 4 new peaks in the aryl region were appearing, along with other changes in peaks in the alkyl region.

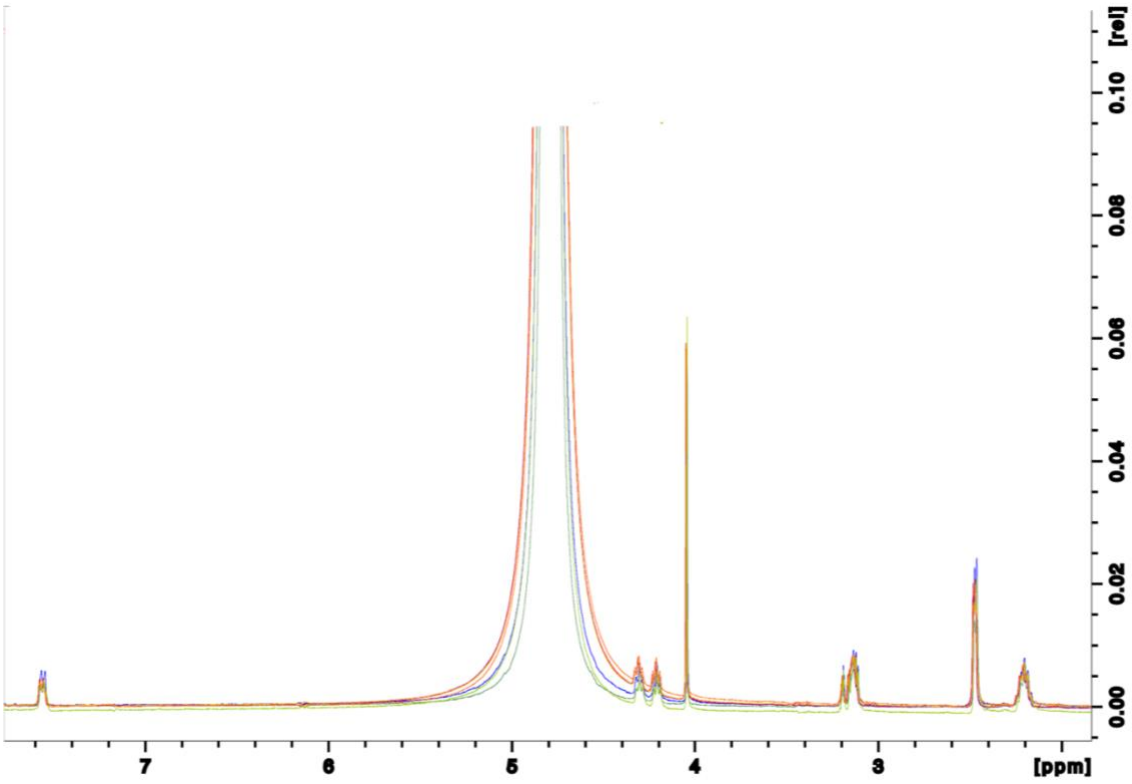

*Figure 20 – ^{1}H NMR spectra of **1** in 0.01 M NaOH in 1 M NaCl at; 0.5, 1, 1.5, 2, 3, 5, and 8 Hours respectively.*

As it can be seen from *Figure 20,* the ^{1}H NMR spectra of **1** had not changed over the 8-hour period, and the spectra were consistent with that of the NaCl control spectrum.

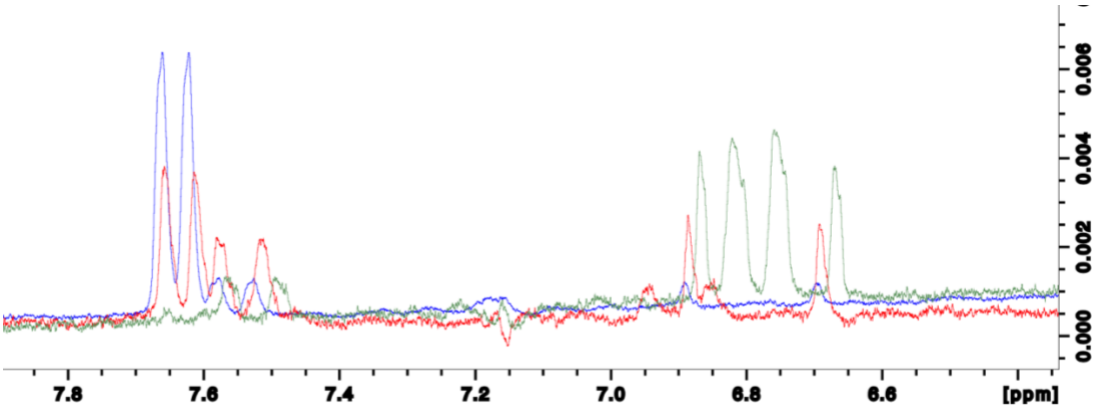

*Figure 21 – ^{1}H NMR spectra of **1** in 1 M NaOH; at 0.5 (blue line), 2 (red line), and 8 (green line) hours respectively. Zoomed in on the aryl proton region.*

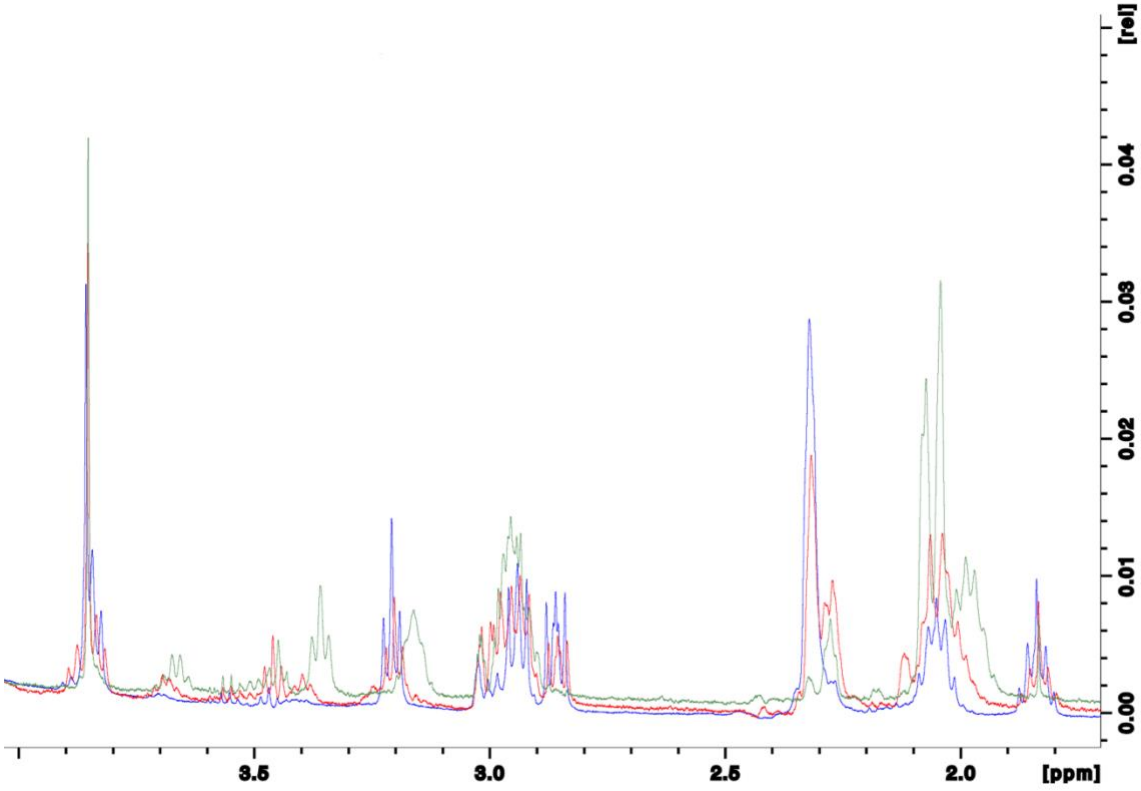

*Figure 22 – ^{1}H NMR spectra of **1** in 1 M NaOH; at 0.5 (blue line), 2 (red line), and 8 (green line) hours respectively. Zoomed in on the alkyl proton region.*

It can be seen from *Figure 21* and *Figure 22*, over the 8 hour timed period the chemical structure of **1** has undergone an undesired chemical change, but that this is not consistent with the spectrum of **lumichrome** in 1 M NaOH, therefore ruling out the possibility of only a Hoffman degradation as speculated. It can be seen in *Figure 21* that the two aryl protons on the lumichrome backbone of **1** had disappeared and the four other new peaks appeared upfield. It was suspected that the stronger base conditions were forming a ring open derivative of **1**/**lumichrome**[43] with a possible partial de-alkylation giving rise to new aryl proton peaks. For these reasons, all flow cell testing was performed under acidic conditions and basic conditions were not explored.

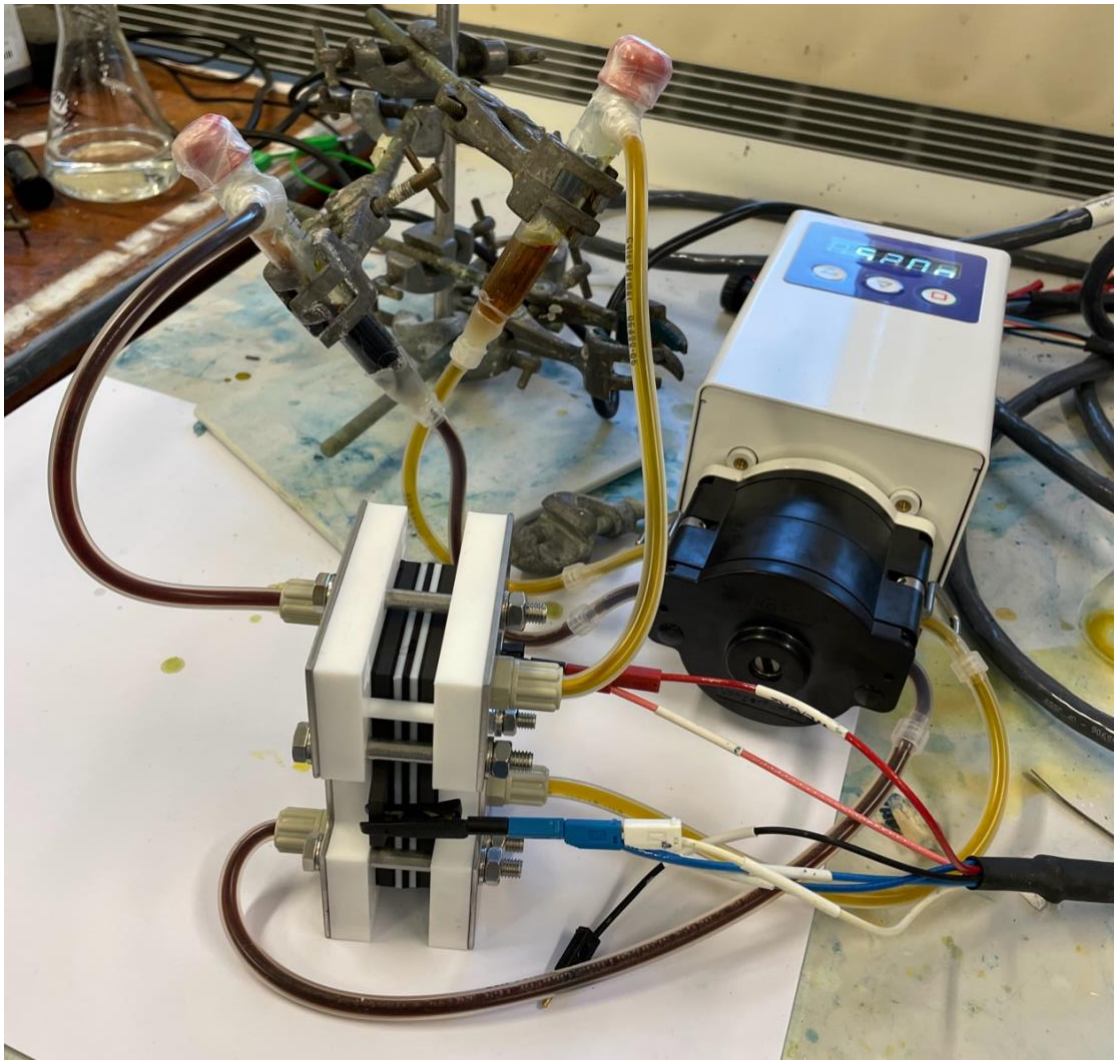

Figure 23 – Picture of flow cell set up using re-engineered falcon tubing as the electrolyte reservoirs and masterflex® peristaltic and transfer tubing.

3.3 Flow Cell Testing with Tiron Couple

A BioLogic VMP-3 multi-channel potentiostat was used to collect all electrochemical testing data. A small, bench-top size Micro Flow Cell® with an internal electrode surface area of 10 cm^2, supplied by Electro Cell (Europe) was used for all tests performed throughout the project. The cell housing, tubing connectors, and all gaskets are made of Teflon or derivatives of Teflon which are highly chemical resistant which is vital for the intended use of this flow cell. The endplates, nuts and bolts are

all composed of stainless steel and have no means to interact with any of the active electrochemical processes (conductive interference). The electrodes used throughout the project were carbon felt (6.35 mm thick, Alfa Aesar) which are compressed against graphite current collectors (see *Figure 23* and *Figure 24* for schematic and image of flow-cell). The carbon felt electrodes were pre-treated by sonication in the supporting electrolyte solution used for any given run. Fumatech FS-930 cation exchange membranes were used for all flow cell tests in this project.

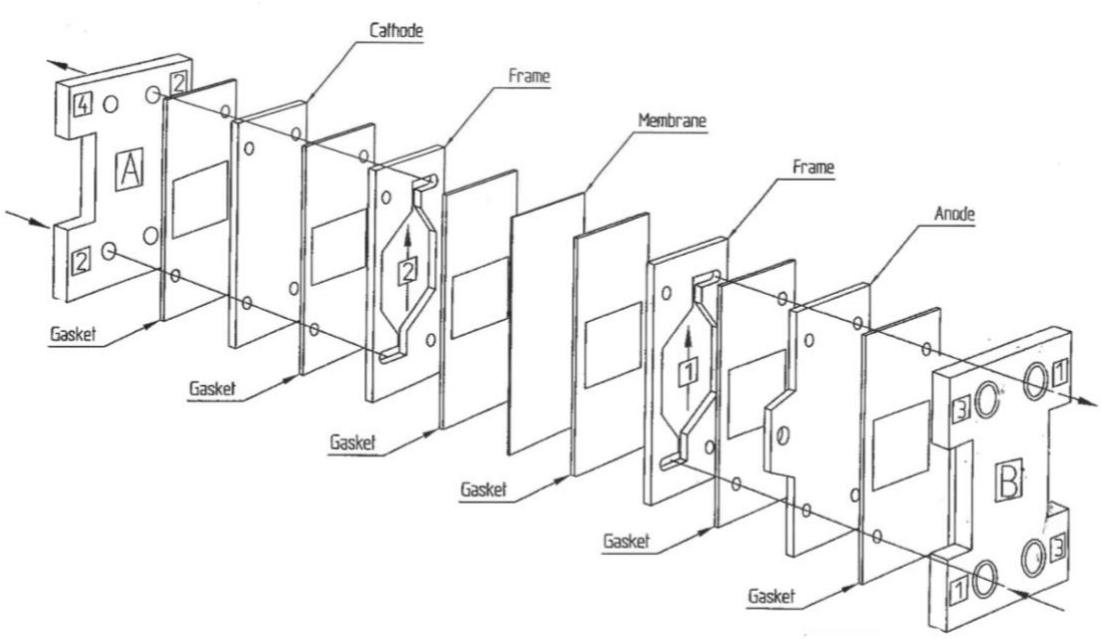

Figure 24 – Schematic showing the individual components of the Micro Flow Cell used throughout this project (original document obtained from the user manual supplied with the flow cell).

For initial flow cell testing, Tiron (trade name) (see structure **A,** *Figure 25*) was used as a positive couple against the novel riboflavin derivative, **1**. This couple was chosen as it has previously been used as a positive couple in a Lead/Tiron RFBs and, more relevantly, used as a positive couple for an AQDS/Tiron system which was expected to exhibit very closely the electrochemical properties of **1**.[17,44] These initial tests were performed with equal concentration (0.1 M) of **1** and Tiron on each side in

1 M H_2SO_4 supporting electrolyte. Preliminary results revealed there was an unwanted side reaction occurring during the charging cycles of the flow cell testing and that this in turn led to a rapid loss in capacity and a failed system (see *Figure 26*). The side reaction is believed to be most likely a Michael addition (see *Figure 25*) of Tiron, which has been seen on multiple occasions in similar studies.[17,25,44,45]

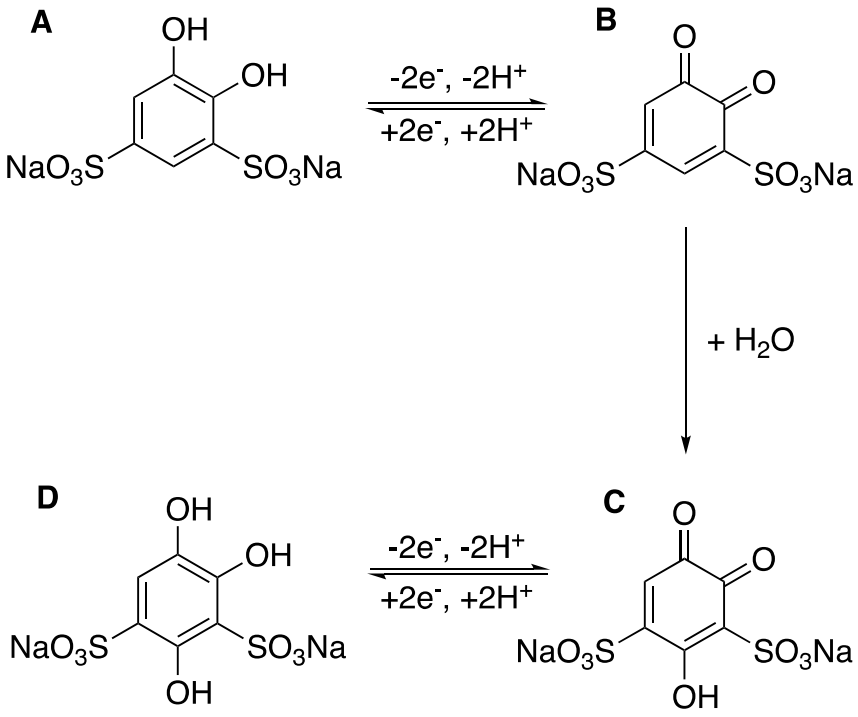

Figure 25 – Schematic showing Michael addition of water to tiron.

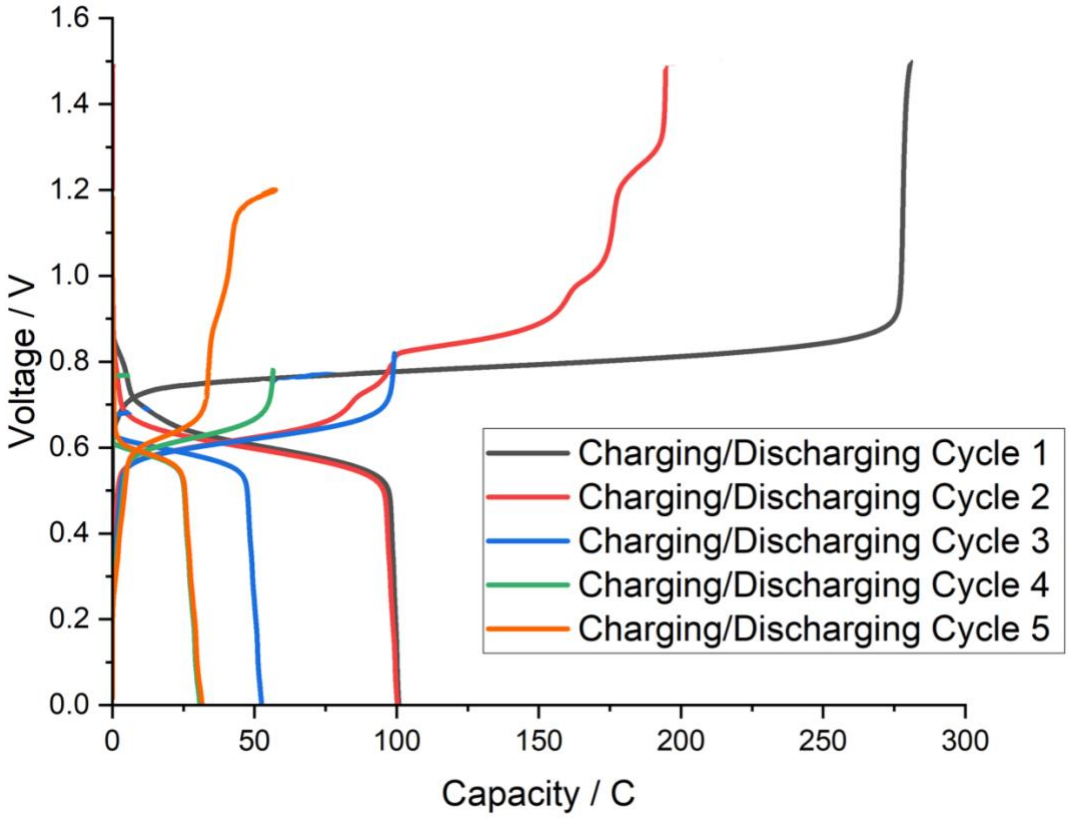

*Figure 26 – Graph showing the results of the first 5 cycles for the initial flow cell test with compound **1** and tiron. Anolyte: 0.1 M compound **1** (0.562 g) in 1 M H_2SO_4 (15 cm^3). Catholyte: 0.1 M tiron (0.314 g) in 1 M H_2SO_4 (15 cm^3). 42 $cm^3.min^{-1}$ flow rate, 1.5 $mA.cm^{-2}$ charge/discharge current.*

As it can be seen from *Figure 26,* the system rapidly lost capacity in its first 5 cycles; the shoulders on the curves for cycles 2 and 5 indicate unwanted side reactions occurring during the charging phase. Cycles 1, 2 and 5 all charge to a higher voltage than cycles 3 and 4, this was because the voltage cut-off was set at different values to observe the changes throughout each cycle. There was no consistency with the cycling of this cell and when the extra shoulders/unwanted side reactions occur, this leads to the cell rapidly losing capacity. The cause of this may have been from either the hydrolysis of Tiron (Michael addition) or could have been due to possible active electrolyte crossover in the system which is highly destructive to cell function.

3.4 Flow Cell Testing with Thioether Quinone Couple

Since the oxidised form of Tiron apparently undergoes an adverse structural change during flow cell testing, synthesising a similar, more structurally inert quinone compound was attempted. The desired compound would retain the quinone functionality of Tiron, while ensuring that all the aryl proton positions were replaced with an alternative, unreactive substituent to improve stability and lifetime of the electrolyte. Compound **4** (see *Figure 28*), taken from the literature[18] matches the structural requirements listed above and has previously been used as a couple for AQDS, for flow cell testing (see *Figure 27)*.

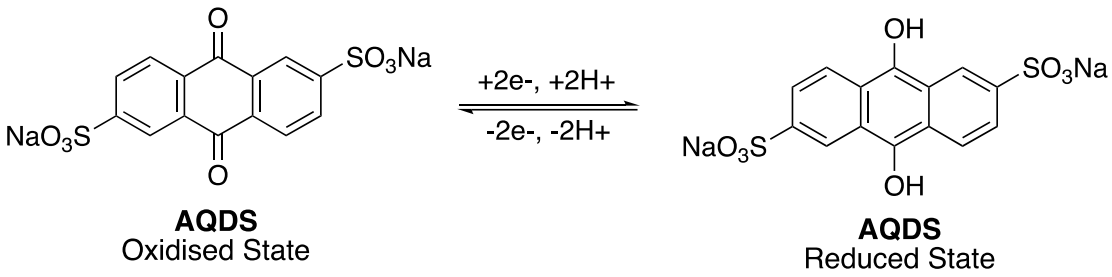

Figure 27 - The electrochemical process AQDS undergoes when a current is applied to it.

An added benefit of compound **4** is that the sulfonic acid chains which enhance the stability of the compound, should result in high water solubility. Whilst the synthesis of compound **4** is a one pot, straightforward electrochemical oxidation/conjugate addition according to the literature, [46] there are a few drawbacks. Firstly, the thiolating agent, MESNa (see *Figure 28*), is a moderately expensive compound (~ £908/mole) which is unsuitable for the purposes of this project which would have required large quantities to produce (~15 g +) of compound **4**. Secondly, during attempted synthesis of compound **4** the ^{1}H NMR spectrum contained unknown

peaks not accounted for in previous reports. Upon further investigation, comparing both the ^{1}H and ^{13}C NMP spectra of compound **4** and spectra from literature[47] it appeared that there were large amounts of the oxidized form of compound **4**. At first, it was suspected that the ElectraSyn apparatus was run for too long and over-oxidized the reaction. Treatment of compound **4** in water with a strong reducing agent such as $NaBH_4$ resulted in the solution changing from brown to pale yellow in colour briefly and then back to the original brown colour after ~2 minutes. This was a clear indication that the reduced form of compound **4** was air sensitive and susceptible to aerial oxidation.

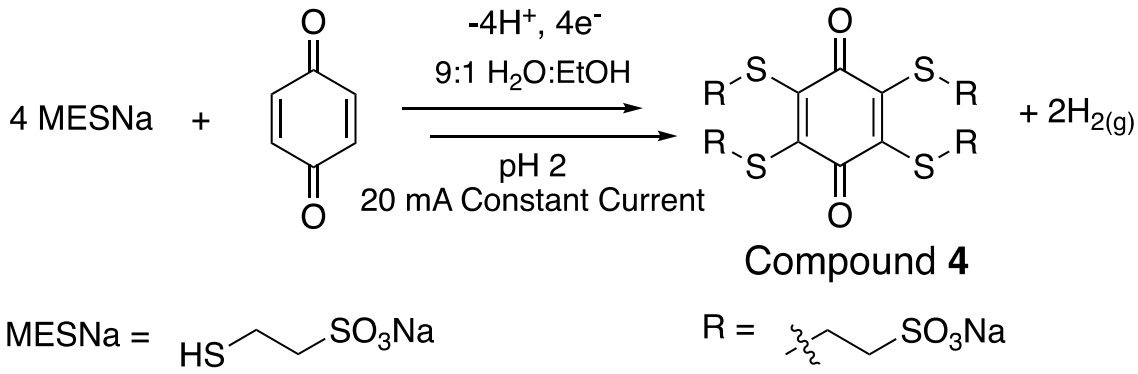

*Figure 28 - Synthetic route of compound **4**.*

Sodium hydrosulphite was used under a $N_{2(g)}$ atmosphere to reduce a sample of **4** to the hydroquinone, making it possible to use as a positive couple against **1** in flow cell testing (see methods section below for details). Once the reduced form of **4** was obtained, flow cell testing was conducted on it and **1**, with initial results suggesting that the system was charging and discharging but that it was rapidly losing capacity through each full cycle. A replicate system was carefully set up ensuring all joints and fittings were correctly sealed, to test if there had been an air leak in during

the initial test, leading to rapid capacity loss observed. Once more, rapid capacity loss of the cell was observed, and the battery ceased to work after ~7 cycles (see *Figure 29*).

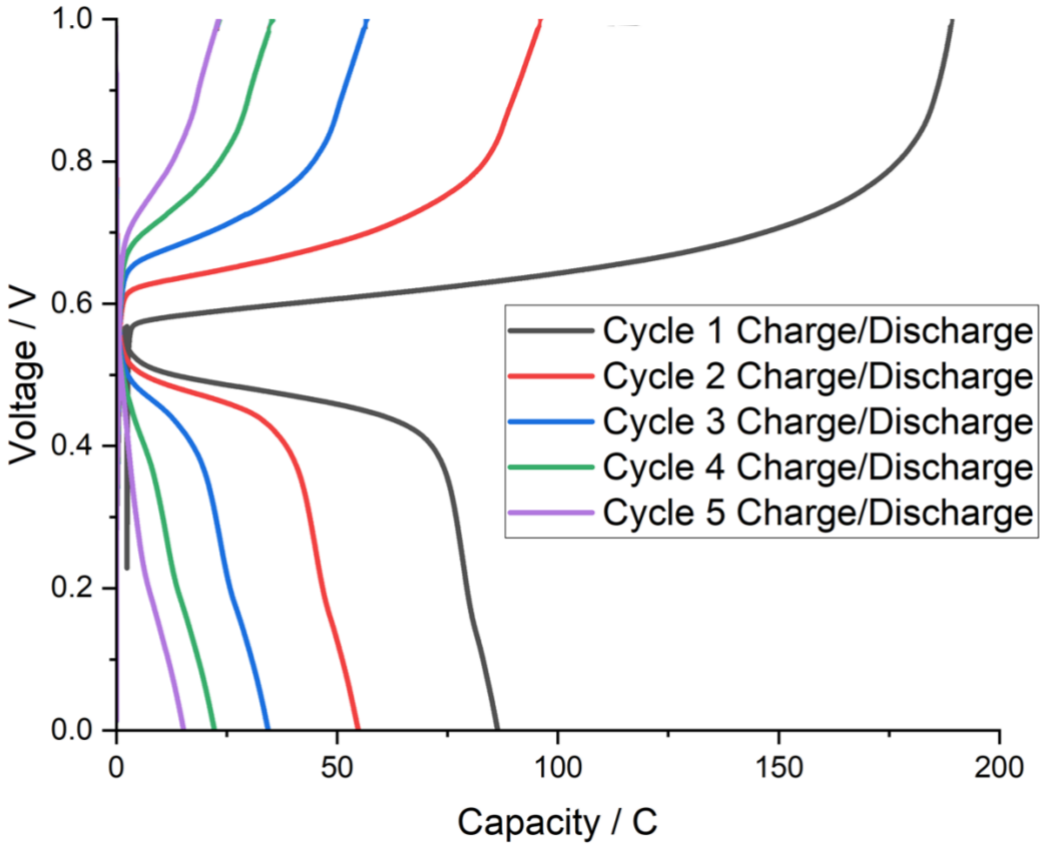

*Figure 29 – Graph showing the results of the first 5 cycles of a flow cell test of; 0.1 M **1** (0.675 g) in 2 M H_2SO_4 (12 mL) as the anolyte, and 0.1 M **4** (0.91 g) in 2 M H_2SO_4 (12 mL) as the catholyte. 42 $cm^3.min^{-1}$ flow rate, 1.5 $mA.cm^{-2}$ charge/discharge current.*

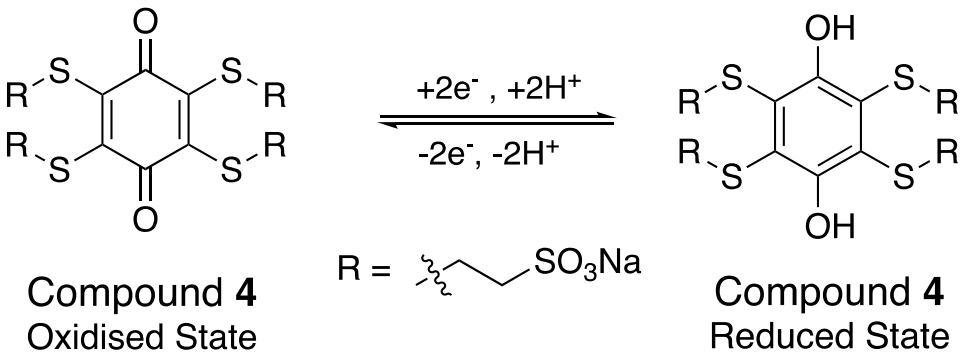

*Figure 30 – Electrochemical redox process, PCET, which compound **4** undergoes.*

Previously mentioned, the reagent for the thiol sidechains, MESNa, has a higher price point than most of the used reagents used in this project and, due to budget constraints, more of this compound could not be synthesized. As a result, no further flow cell testing with this compound was explored. Given more research time, a more air-stable, highly water-soluble derivative of benzoquinone would be explored using, cheaper and more common, commercially available thiol reagents such as mercaptoscuccinic acid, which is ~£68/mol.

3.5 Flow Cell Testing with HBr Couple

Inspired by the concepts in the literature [28,48,49] and from previous unpublished work within the research group, another flow cell set-up was attempted following the Tiron and thioether quinone coupled tests. For this cell HBr was to be used as a couple against **1**, moving away from an all-organic system to an organic/inorganic hybrid system. To begin with the cell was set up such that there was a 5:1 ratio of HBr:**1** present in the electrolyte tanks with 1 M H_2SO_4 as the supporting electrolyte. This system presented multiple issues upon cycling for battery testing. Firstly, a large degree of osmotic crossover was observed from the HBr to the flavin side, which inevitably caused major changes in the electrolyte concentrations. The second issue was that capacity was lost very rapidly throughout each cycle and the columbic efficiency was ~15 % during the first cycle. Present within the flow cell data was a shoulder on the discharge cycles indicating that there was a side reaction occurring which was presumed to be leading to the rapid capacity loss of the system (see *Figure 31*). Numerous attempts were made to optimise this system to avoid the side reaction, each time changing different parameters: the concentration of the acid electrolyte to

combat osmotic crossover, the concentration ratio of electrolytes, and use of a bromine complexing agent to combat adverse reactions.

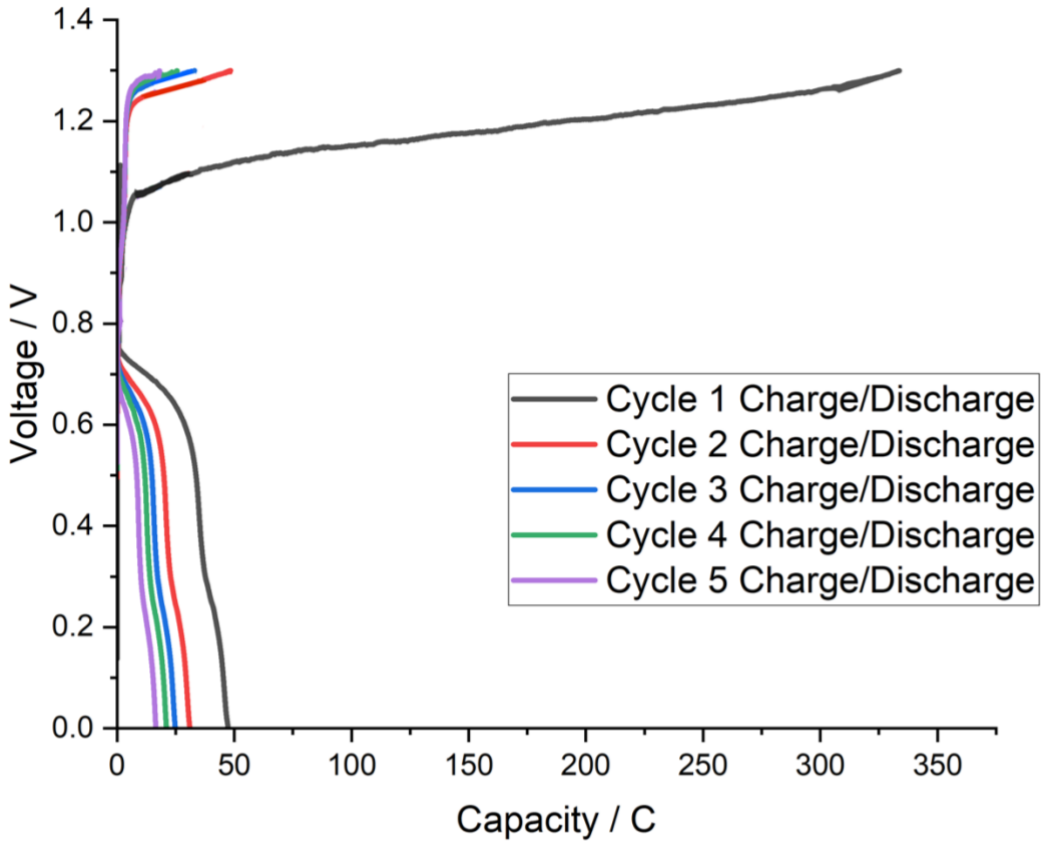

*Figure 31 – Graph showing the first 5 cycles for a flow cell of; 0.1 M **1** (0.675 g) in 2 M H_2SO_4 (15 cm^3) as the anolyte and 0.5 M HBr (0.89 cm^3) in 1 M H_2SO_4 (15 cm^3). 42 $cm^3.min^{-1}$ flow rate, 1 $mA.cm^{-2}$ charge/discharge current.*

As it can be seen from *Figure 31* the cell charges to around 325 C in the first charge cycle which is unexpected given the theoretical maximum capacity of the cell is ~230 C). After the first charge cycle a major drop in discharge capacity was seen and thereafter the cell rapidly lost capacity until it ceased to function, forcing serious consideration of the optimizations required to make the cell functional.

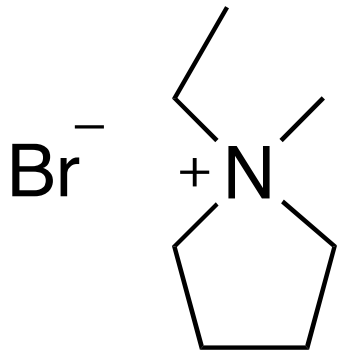

Figure 32 – Structure of MEP, a bromine complexing agent.

During flow cell testing with HBr, it was found that the transparent, flexible peristaltic tubing used had formed a solid while layer within the tubing, becoming brittle and unusable. This was suspected to be due to the formation of Br_2 (as expected in a cell of this type) and this segregating from the electrolyte to react with the tubing as it has low solubility in aqueous conditions. In the literature[50] a similar organic/inorganic system with Viologens and HBr was found which was used with the complexing agent, 1-ethyl-1-methylpyrrolidinium bromide (MEP) (see *Figure 32*). Here, MEP was used as a bromine complexing agent to stop the formation of a viologen-Br_2 adduct which was insoluble in water; this was possible as the MEP-Br_2 binding energy was higher than that of viologen-Br_2. While there was no indication that the flavin (**1**) was crossing over and binding to Br_2, the initial suspicions were that Br^{3-} was releasing Br_2 in an irreversible reaction, damaging the cell performance and hardware. Upon introduction of MEP into the **1**/Br_2 system, it was immediately apparent that the use of the complexing agent was beneficial, as higher coulombic efficiency was observed and the cell did not lose capacity as fast the initial tests. The cell was manipulated a further 5 times (see *Figure 33*), in each case the amount of

substance changed until a system was ran which held capacity for 13 cycles with a coulombic efficiency of ~70 % (see *Figure 34* for further details).

HBr Conc.	**1** Conc.	H_2SO_4 Conc.	MEP Conc.	Outcome
0.25 M	0.25 M	2 M	N/A	High amounts of osmotic crossover to **1** electrolyte side, cell failed within 5 cycles
0.5 M	0.2 M	3 M	N/A	Less osmotic crossover than previous, cell seemed to be performing slightly better yet still failed within 5 cycles.
0.5 M	0.2 M	3 M	N/A	Same cell as before but testing of membrane pre-treatments from literature. Cell performed even worse.
0.8 M	0.2 M	3 M	0.4 M	Cell performed much better than before with the capacity not fading as quick, higher coulombic efficiency observed
0.8 M	0.2 M	3 M	0.6 M	This cell was successful and retained capacity (see *Figure 34*) for the 13 cycles it ran for.
1.2 M	0.3 M	3 M	0.9 M	This cell was an attempted scale-up of the previous, successful cell to increase capacity but was unsuccessful and did not retain capacity as expected.

*Figure 33 – Table showing the various parameters changed to optimise the HBr/**1** cell.*

As can be seen from *Figure 33,* an increase of supporting acid electrolyte concentration helped to mitigate the osmotic crossover issue within the cells. It can also be seen that the use of MEP aided as a bromine stabilizer and allowed the cell to run more efficiently and retain capacity throughout the cycles during which it ran (see *Figure 34*).

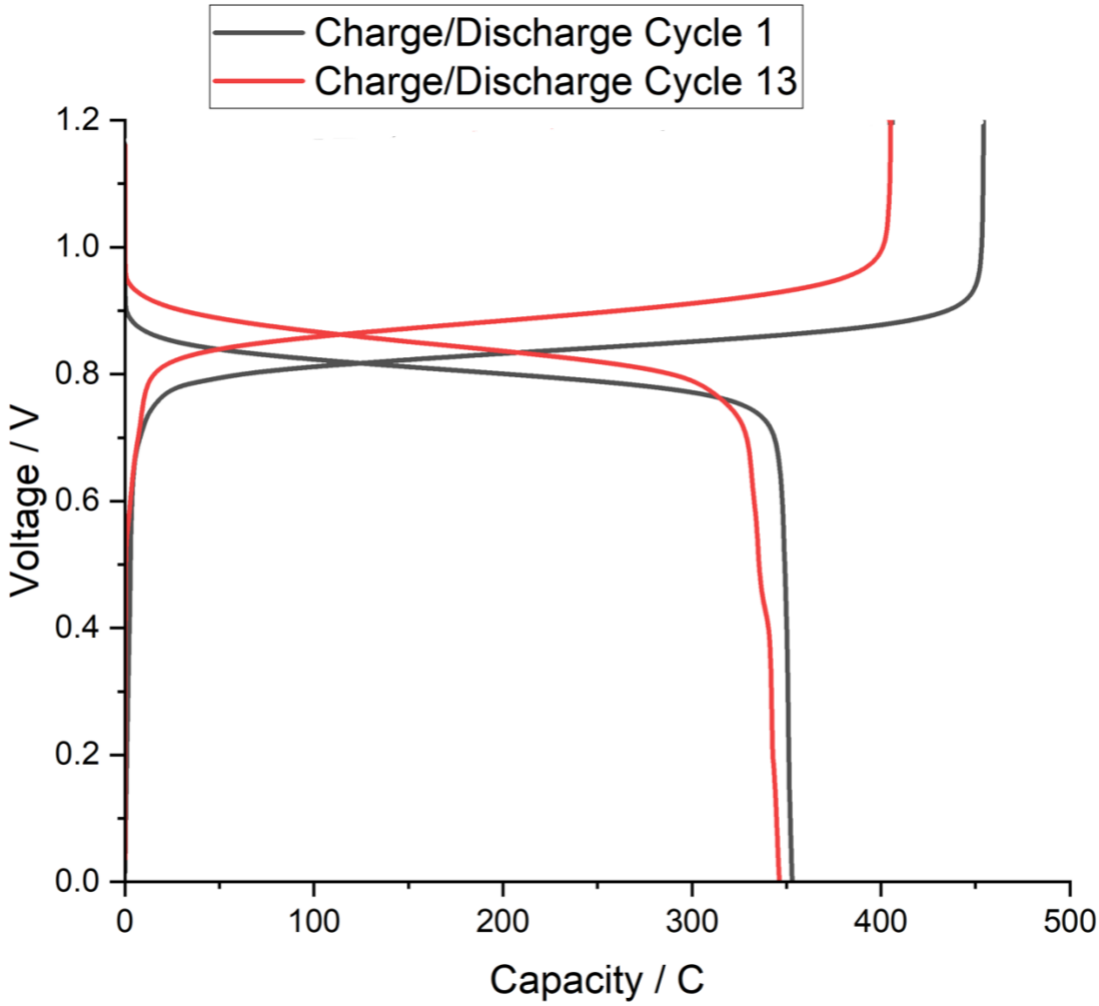

*Figure 34 – graph showing the flow cell results of a cell containing; Anolyte: 0.2 M compound **1** (1.75 g) in 3 M H_2SO_4 (15 cm^3). Catholyte: 0.8 M HBr (1.43 cm^3) + 0.6 M MEP (1.75 g) + 1 mM $Br_{2(aq)}$ (0.5 cm^3) all in 3 M H_2SO_4 (14 cm^3). 42 $cm^3.min^{-1}$ flow rate, 3 $mAcm^{-2}$ charge/discharge current.*

3.6 Peristaltic Pump Issues

Shortly after the promising stable flow cell result with HBr and MEP, (*Figure 34*) the peristaltic pump used by the research group sustained water and acid damage and ceased functioning usefully. Due to this and budget constraints at the time, coupled with the pump not being repairable, flow cell testing could not be carried out until a suitable alternative was found. Work on a potential suitable alternative was immediately carried out (see chapter 4 below), but unfortunately the immediately available alternative was not suitable for this project. During this time, the group was

awarded an RSC Research Enablement grant which allowed us to purchase two new pumps and a further flow cell to allow for more efficient flow cell testing. However, these issues and delays spanned over a total of four months with no functioning pump, and so valuable time for flow cell testing was lost.

Following the arrival of replacement equipment, the promising **1**/HBr system was set up in an attempt to reproduce results from the previous good run. The cell was run overnight to collect results and upon inspecting the cell in the morning, there was discolouration of the lubricant on the pump head rollers along with what appeared to be a formation of metal filings.

Figure 35 – Image of suspected rust formation on new pump head due to suspected bromine/HBr leeching from tubing.

There was no evidence of tubing ruptures or leakage from any part of the system, which lead to the conclusion that bromine was leeching out of the system *via* the peristaltic tubing and damaging the equipment. Shortly after the visual inspection the pump head was carefully being cleaned, but during this process it was apparent the suspected bromine leak was so significant that it had leeched into the plastic housing and had completely deteriorated the housing structure leaving it crumbling to the softest touch (see *Figure 36*). This discovery not only explained the deterioration of the previous peristaltic pump but also to why in previous experiments the system did not give reproducible results for identical parameters. As this system was causing damage to the equipment and incurring high-cost repairs, this cell system was set aside until an experimental set-up which was suitable for working with bromine could be arranged.

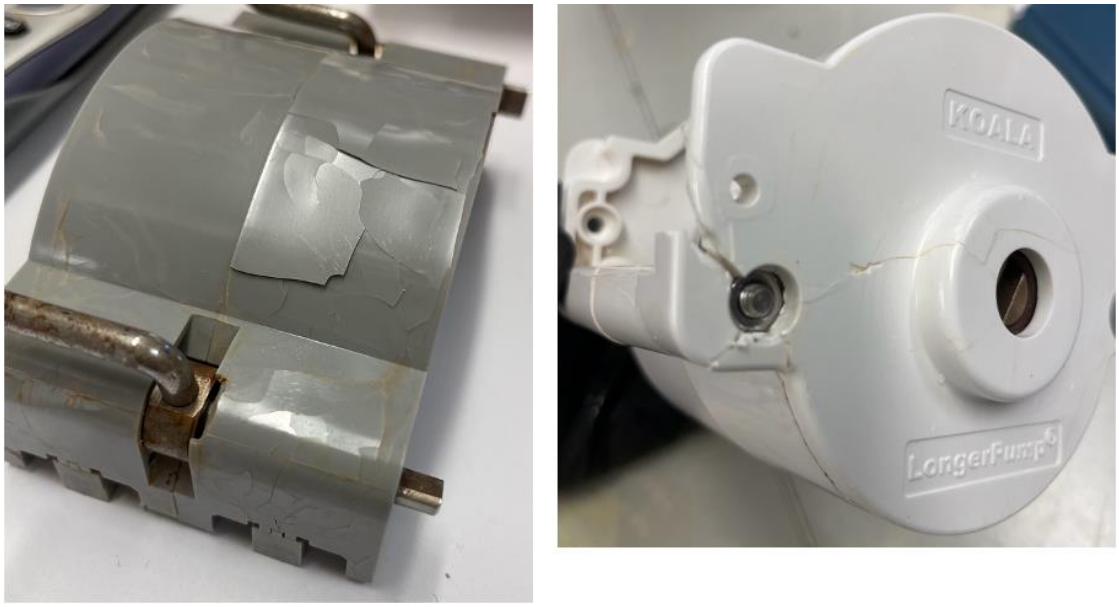

Figure 36 – images of damaged pump head due to suspected bromine damage.

3.7 Flow Cell Testing with Iron (II) Couple

With Tiron and HBr disqualified as redox couples for **1**, the literature was again explored to find a suitable couple for a sustainable, cost-effective system. Seen within this area of research,[51] was a study was found which used AQDS as an anolyte coupled to an Fe^{2+} complex, $FeSO_4$, as the catholyte. With **1** acting as an AQDS alternative, this study's AQDS/Fe couple was highly attractive as flow cell couple for compound **1**. Firstly, $FeSO_4$ is a waste by-product of the steel industry allowing for this compound to be part of a highly sustainable and eco-friendly system by valorising waste products. Secondly, $FeSO_4$ is commonly found as a medicinal supplement for humans and used in soil as a means of a pH regulator, indicating that this compound is less toxic and safer for the environment compared to traditional metal based RFBs. Finally, this system is also far more straightforward and contains fewer components than that of the HBr coupled cell, so fewer variables need to be taken into consideration when troubleshooting and optimising the system.

Figure 37 – Suspected air bubbles containing $O_{2(g)}$ throughout peristaltic and transfer tubing.

This $FeSO_4$ system was set up as both a symmetrical and unsymmetrical system (see methods below for more information). The results were consistent with one another, with both rapidly losing capacity through each charging-discharging cycle with the capacity loss consistent throughout each cycle (see *Figure 38*). Upon further inspection on the flow cell, there appeared to be a build-up of trapped air bubbles (presumed to be either air or arising from water oxidation/reduction) throughout the transfer and peristaltic tubing (see *Figure 37*). When the system was first setup, all visible trapped air bubbles were eliminated before the potentiostat was started, and so the formation of bubbles is something that occurred over the course of cell testing. Every effort was made to ensure that the system was a closed-loop and air-tight, and

therefore it was suspected that the tubing used was oxygen permeable, leading to ingress and side reactions which are the cause of the air bubbles and hence the rapid loss in capacity, destroying the battery.

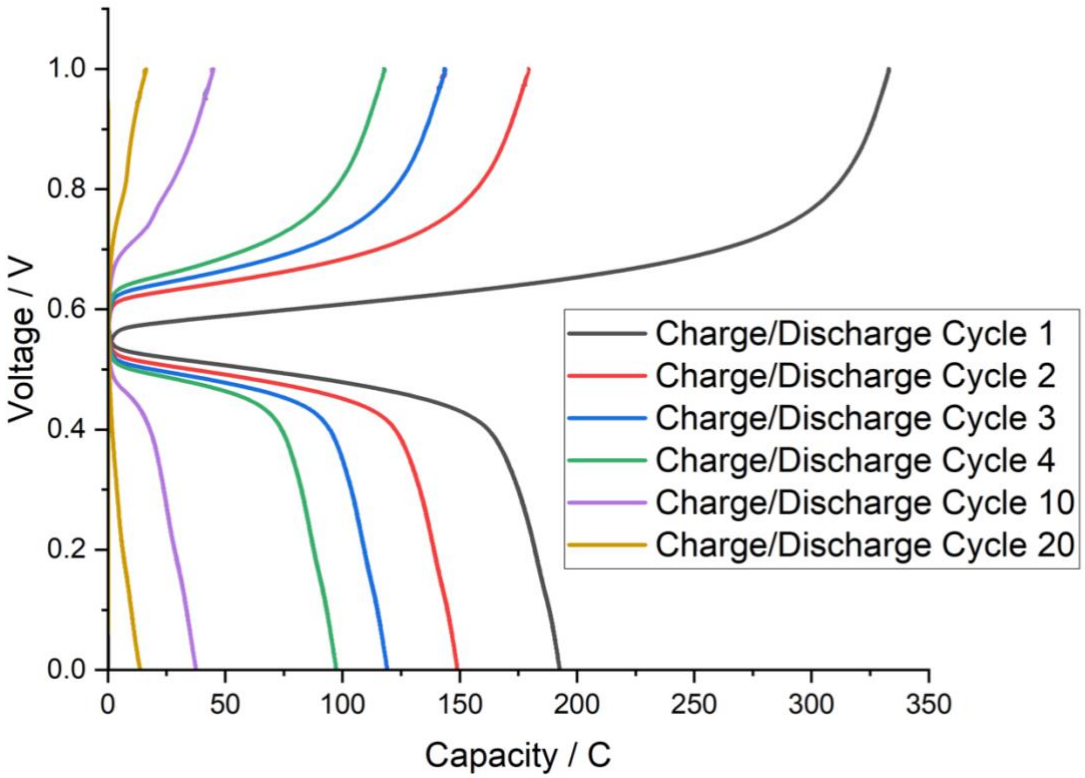

*Figure 38 – Graph showing the flow cell results of the unsymmetrical Iron (II) coupled cell. Anolyte: 0.2 M **1** (1.35 g) in H_2SO_4 (12 cm^3), catholyte: 0.4 M $FeSO_4.7H_2O$ (1.33 g) in H_2SO_4 (12 cm^3). 50 $cm^3.min^{-1}$ flow rate, 3 $mA.cm^{-2}$ charge/discharge current.*

3.8 Tubing Air Permeability Testing

Throughout the project and within the lab group, many flow cell tests were performed with consistent capacity loss observed during each cycle. At the time, this was assumed to be due to unfavourable chemical and electrochemical changes in the systems during testing. A cell test employing of the well-known, all-vanadium cell was set up to obtain benchmark performance for the system under our usual cell

conditions and parameters. The all-vanadium cell charged to a reasonable capacity on its first charge cycle (to ~470 C, theoretical limit of 724 C) but when moving on to the discharge cycle, only 3 C of capacity was observed, and the cell essentially died off thereafter. Given that the vanadium (II) and (III) species used in the flow-cell testing are a highly air sensitive compounds, this was another clear indication of an air leak within the system. When setting up the flow cell, all efforts were made to ensure that all the joints, fittings and potential air-leak susceptible areas were covered and sealed. Given these precautions, it became more apparent that the air leak may have been due to both the used transfer and peristaltic tubing used being O_2 permeable. To test this hypothesis, a static, closed loop system comprising the electrolyte reservoirs along with the different tubing types were set up containing a highly air sensitive $VOSO_4$ (*i.e.,* V(II)) solution, and left to stand to observe if any colour changes which might take place. This crude but simple test relies on the fact that aqueous V(II) salts are an intense purple colour, but V(III) is green – provided diffusion within the liquid is slow, this was expected to allow easy determination of the sites of any leaks.

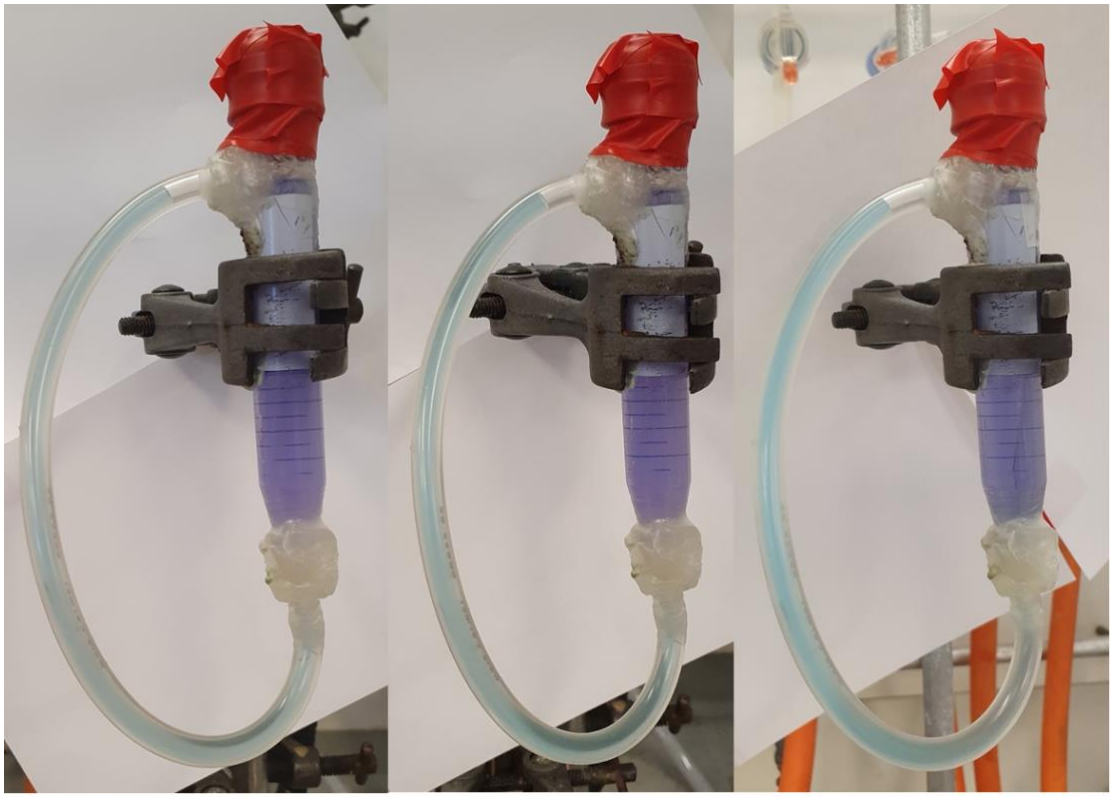

Figure 39 - static closed-loop test of transfer tubing at; 1, 24 and 96 hours respectively.

The results were clear within hours, where all the V(II) solution was sitting within the tubing, there was an explicit colour change from purple to blue-green giving a clear indication for formation of a V(III)/V(IV) solution and showing oxidation is occurring within these O_2 permeable tubing (see *Figure 39* and *Figure 40*). The outcome of this test was a breakthrough in potentially understanding why the many previous flow-cell results throughout the run of this project (and others) saw similar trends with consistent capacity loss since all involved redox active compounds are susceptible to aerial oxidation.

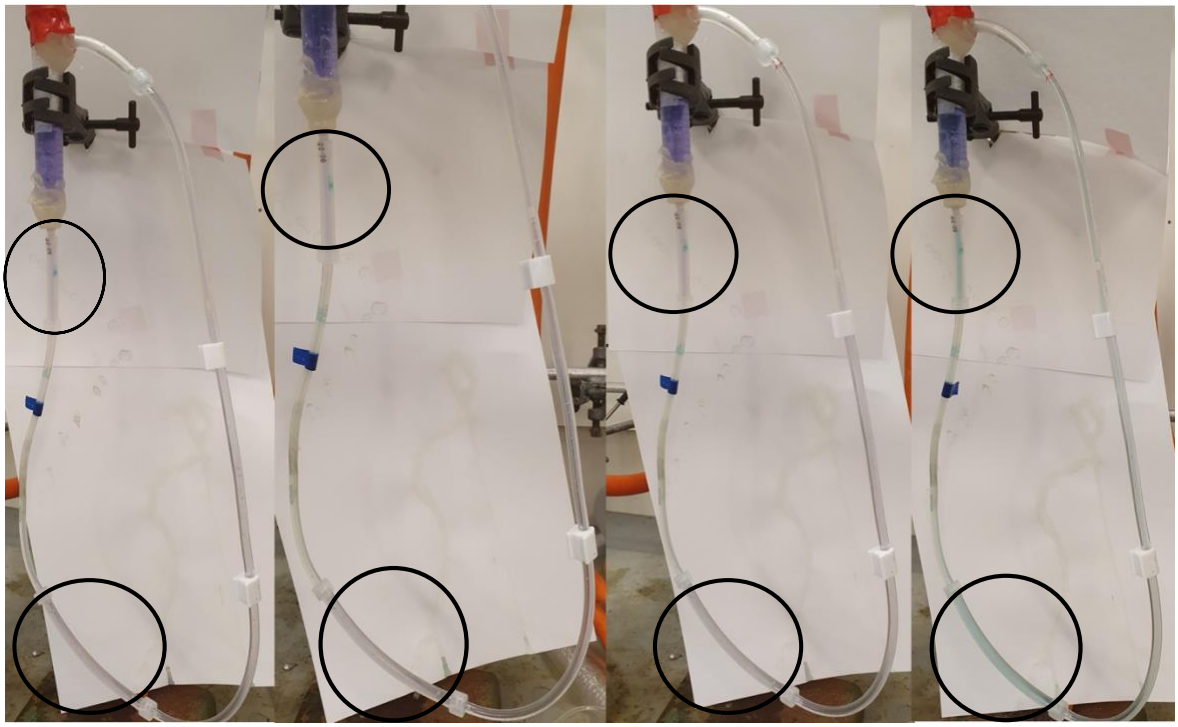

Figure 40 – Static closed-loop test of 2 variations of peristaltic tubing at; 0, 1, 3 and 50 hours respectively. Black circles indicating the silicone-oxide cured tubing and the remainder of tubing being a different formulation of transfer tubing.

3.9 Methods and Discussion

Synthesis of compound **4**:

Benzoquinone (0.303 g, 3.5 mmol) and MESNa (1.839 g, 11.2 mmol) in H_2O (10 cm^3) and EtOH (0.6 cm^3) spiked with 2 M H_2SO_4 (0.1 cm^3) was added to the Electrasyn reaction vessel and cycled at constant current (20 mA) unstirred for 70 hours. After 70 hours the reaction mixture was decanted into a beaker filled with EtOH (60 cm^3) to allow the product to crash out overnight. Filtered at pump, **4** collected as a brown solid (1.851 g, 87.1 %). This prep was copied from that of ideas in the literature [46] with alterations to obtaining the fully reduced form of **4** for flow cell testing due to its air-sensitive nature.

The reduction process to obtain the reduced form of **4** involved dissolving crude **4** in water, degassing with $N_{2(g)}$ followed by adding the reducing agent to the solution. Once the reduction was complete, **4** was precipitated with degassed EtOH to try minimizing any re-oxidation, once precipitated the compound was reduced to a solid. Throughout this process all efforts were attempted to minimize contact with the air to avoid re-oxidation but there were still room for human error and the need to transfer the suspended solid to be reduced, which involved some contact to air.

Base (NaOH) NMR stability testing:

1 (~10 mg) was dissolved in 1 M NaOH (~1 cm^3) (stock solution) with ^1H NMR spectra taken at 0.5, 1, 1.5, 2, 3, 5, and 8 hours respectively. The same procedure was repeated for a 0.01 M solution of NaOH which was made by diluting the 1 M NaOH stock solution with a 1 M brine solution. A control NMR sample of **1** (~10 mg) in 1 M NaCl (~1 cm^3) and a control NMR sample of **lumichrome** (~10 mg) in 1 M NaOH (~1 cm^3) were made up. All NMR samples scanned using a DMSO-d^6 capillary.

N.B, for all flow cell tests in this project electrolyte solutions were degassed using $N_{2(g)}$ and then further purged again with $N_{2(g)}$ once employed into the flow cell electrolyte tanks. For all CV testing, analyte solutions were also purged with $N_{2(g)}$ to ensure no oxygen peaks are present in the data.

4. Alternative, Cost Effective Pump Testing

4.1 Motivation

Following the failure of the peristaltic pump used for flow cell testing in the middle of the of the research project, a viable alternative to allow testing to continue was sought. Variable flow rate peristaltic pumps tend to have a high price point, in the region of £1000 and above, and due to budget constraints, a cost-friendly solution was rapidly required in short order. The idea was proposed by taking the simple principle that a peristaltic pump is closed loop system and given we need an inert, oxygen-free atmosphere within the cell, another pump type capable of operating in this way may be suffice. Browsing online retailers, it was decided to attempt to use a small fish tank pump (£ 9.99 per pump at time of purchase) as a cost-effective alternative. It is essential for the flow cell testing that the pump can be easily manipulated to give a variable flow rate, which was expected to be achieved by varying the power supply to the fish tank pumps. In order to achieve this, the pump was wired up to a variable voltage power source, sourced from the University of Kent Physics teaching labs – the power supply in question is hardwired to supply 3.3, 4.2, 6.5, 7.0, 7.8, or 8.4 volts on demand. Home-made modifications and attachments such as; different sized tubing, zip-ties, parafilm, and blu-tack were all used to achieve a closed loop system like that of using a peristaltic pump for testing purposes. This was all to ensure the solutions were running at a correct flow rate and under an inert atmosphere.

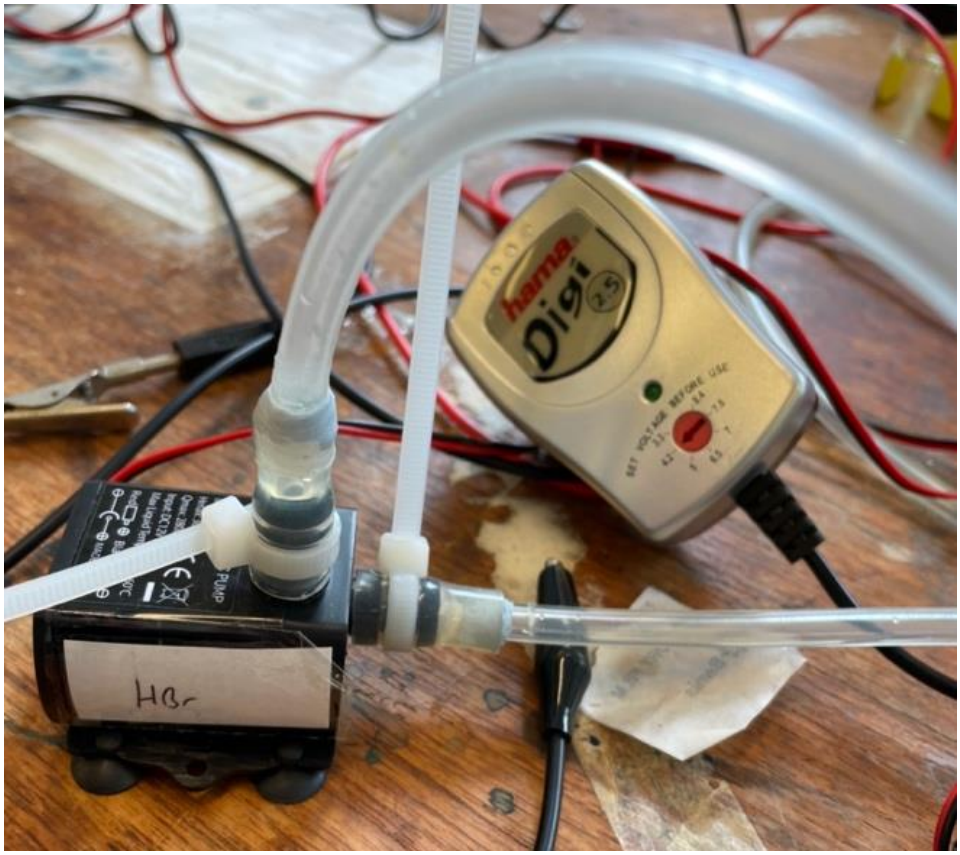

Figure 41 – image of fish pump and variable voltage power supply used for all testing throughout this chapter.

4.2 Experimental Procedure

A simple experiment was set-up to measure the flow rate of the pumps at a given voltage on the power supply. The tests were conducted by flowing water through a single pump from a large reservoir into a graduated beaker. This was also repeated with 2 identical pumps wired up in parallel *via* the same power supply to determine the effect of additional load on pump speed. In addition to these parameters, the system was set up using the transfer tubing used in earlier peristaltic tests as most narrow point (size 16, inner diameter 1/8th inch), this quantity is important as this dictates the restricting flow rate above a certain threshold. The time

required to transfer either 50 cm^3 or 100 cm^3 was recorded with 4 replicates, and an average flow rate determined. This was repeated for all 7 voltage settings on the power supply. Using the collected data, the flow rate (in cm^3/min) at a given voltage was calculated using the equation:

$$y = 50\left(\frac{60}{t}\right) \quad (Equation\ 8)$$

Where, y = flow rate (cm^3/min), t = average time taken to dispense 50 cm^3 from pump. 50 and 60 are both constants, 50 to denote the volume of liquid dispensed and 60 to allow the conversion of one minute to seconds.

4.3 Results and Discussion

Single Pump Flow Rate Test		
Voltage / V	t_{ave} / s	Flow rate / cm^3/min
3.30	8.22	365
4.20	6.34	473
5.00	5.54	542
6.50	4.69	640
7.00	4.35	690
7.80	4.04	743
8.40	4.01	748

Figure 42 – table to show the collected time data used to calculate the flow rate at a given voltage for a single pump.

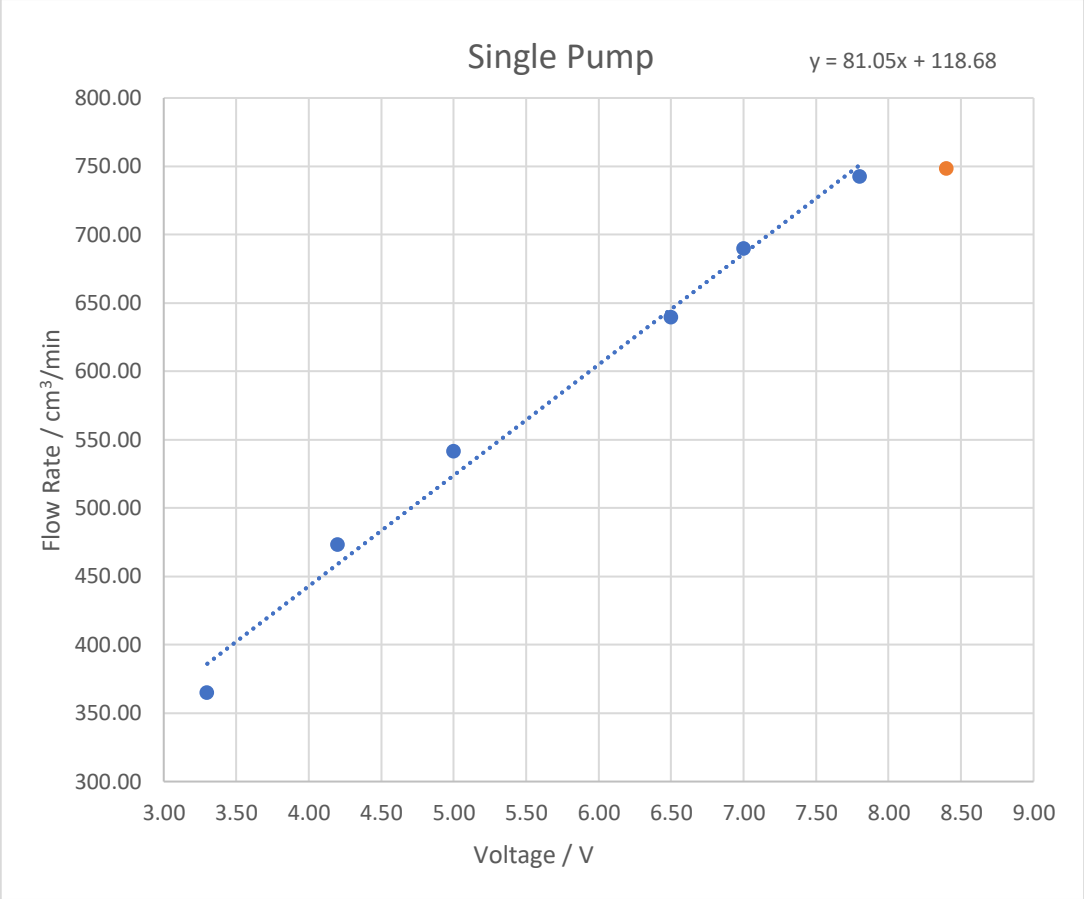

Figure 43 – graph presenting the data presented in Figure 42, showing a plot of flow rate against voltage.

Dual Pump Flow Rate Test		
Voltage / V	t_{ave} / s	Flow rate / cm^3/min
3.30	9.02	665
4.20	7.13	842
5.00	6.10	984
6.50	5.59	1070
7.00	5.29	1130
7.80	4.82	1244
8.40	4.75	1263

Figure 44 – table to show the collected time data used to calculate the flow rate at a given voltage for two pumps wired in parallel.

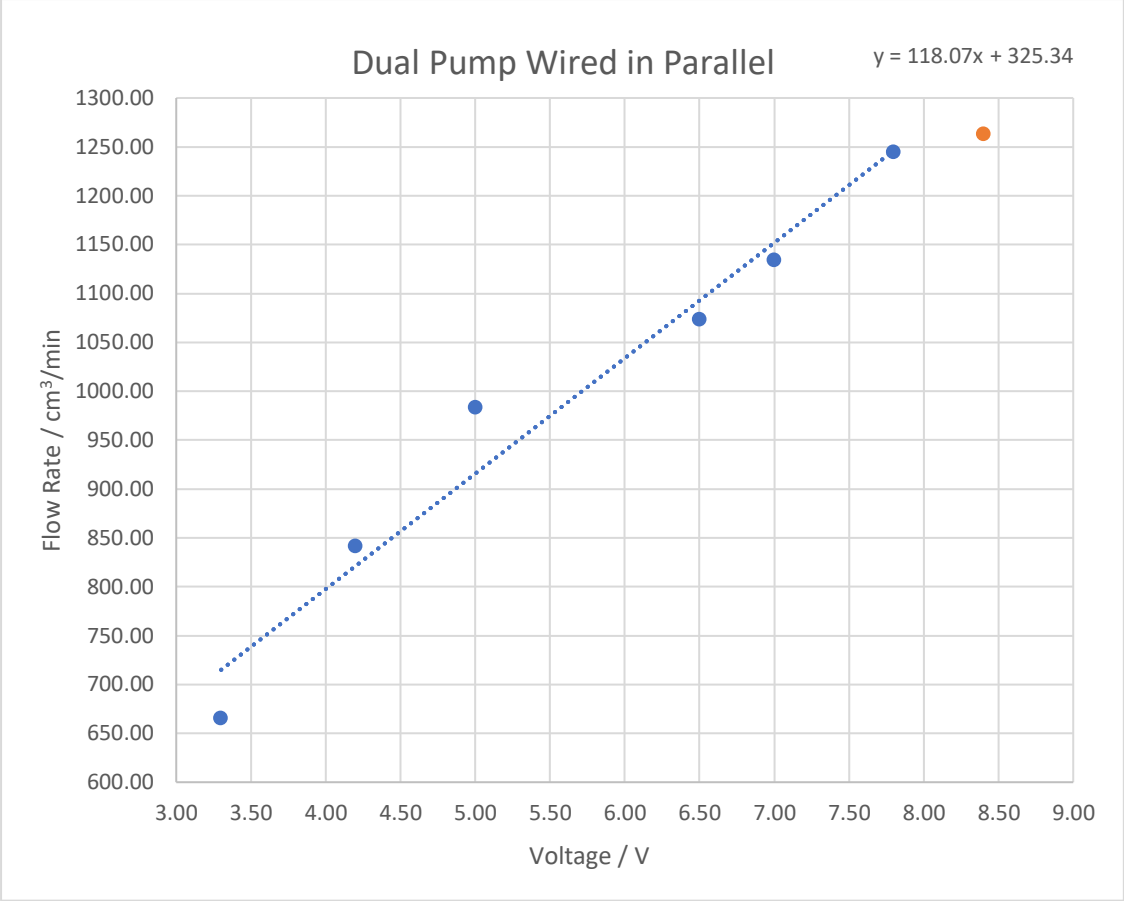

Figure 45 - graph presenting the data presented in Figure 44, showing a plot of flow rate against voltage for two pumps wired in parallel.

The results show that for both the set up with single and dual pumps, there is a linear relationship between the flow rates and drive voltage below 7.80 V. Both data points for the 8.40 V setting on the graphs (denoted by the orange data points in graphs on both Figure 43 and *Figure 45*) were left out the line of best fit as it was found to be plateauing off after the 7.80 V setting. This is attributed to the size restriction width of the tubing only allowing a set amount of fluid through it above a certain voltage value. These data points were excluded from the line of best fit as the flow rate only increased by about ~1 % in the final voltage value test for both experiments, and the desired flow rates for the flow cell testing are much lower than this.

Even at the lowest voltage settings, the flow rates were too high for the purposes of this project (previous flow rates using the peristaltic pump before it failed were 40 – 100 $mL.min^{-1}$) The flow rate test experiment was therefore conducted again using another variable voltage source capable of supplying lower drive voltages. However, this found that the lowest possible drive voltage at which the pump would dispense liquid was 2.80 V; at any lower voltage the pump would cut off. From the fit to data previously obtained (see graph at *Figure 43*), this results in a minimum flow rate of 345.65 $cm^3.min^{-1}$.

This is perhaps unsurprising given that the y-intercept of the graph at *Figure 43* is 118.68 $cm^3.min^{-1}$ at 0 V. Ultimately, these values are too high for the purposes of this project as flow rates in the region of 40 – 120 $cm^3.min^{-1}$ are required given the dimensions of the flow cell used.

5. Collaborative Studies

5.1 Identification of Prospective Collaborators

Once it was determined that the tubing used for flow cell testing was oxygen permeable and that this was causing additional issues and setbacks for the project, we reached out to Ana Sobrido (AS) at Queen Mary University London (QMUL) to collaborate on testing. AS and her research group have extensive knowledge working with RFBs and specifically with AQDS and vanadium-based systems, so collaboration with them is expected to be highly advantageous to both groups with the prospects of future joint publications using our novel flavin, **1**. Arrangements were made to perform our flow cell tests on their set-up to acquire the necessary results using a known, functioning system, and so allowing us to identify issues specific to our testing rig whilst also characterising the battery system properly until such time that the Kent set-up was repaired and redesigned.

As mentioned earlier, AQDS has similar electrochemical properties to those of **1** and throughout this project we have explored various couples reported in the literature which have been used as couples for AQDS. This, coupled with AS' extensive knowledge around AQDS and vanadium RFB systems, prompted us to set up a flow cell of vanadyl sulphate ($VOSO_4$) as a couple against **1** giving a benchmark against that of a known AQDS/$VOSO_4$ cell.

5.2 Flow Cell Testing

During the initial visit to QMUL, we discussed and planned out a test cell of 0.2 M compound **1** and 0.4 M $VOSO_4$ in 3 M H_2SO_4 supporting electrolyte, as these were similar conditions to those which we had previously tested with **1** in our laboratory. This experiment was set up to run for 30 cycles with a flow rate of ~7.5 $cm^3.min^{-1}$. This system failed as blockages formed within the transfer tubing and electrode channel (see *Figure 46*).

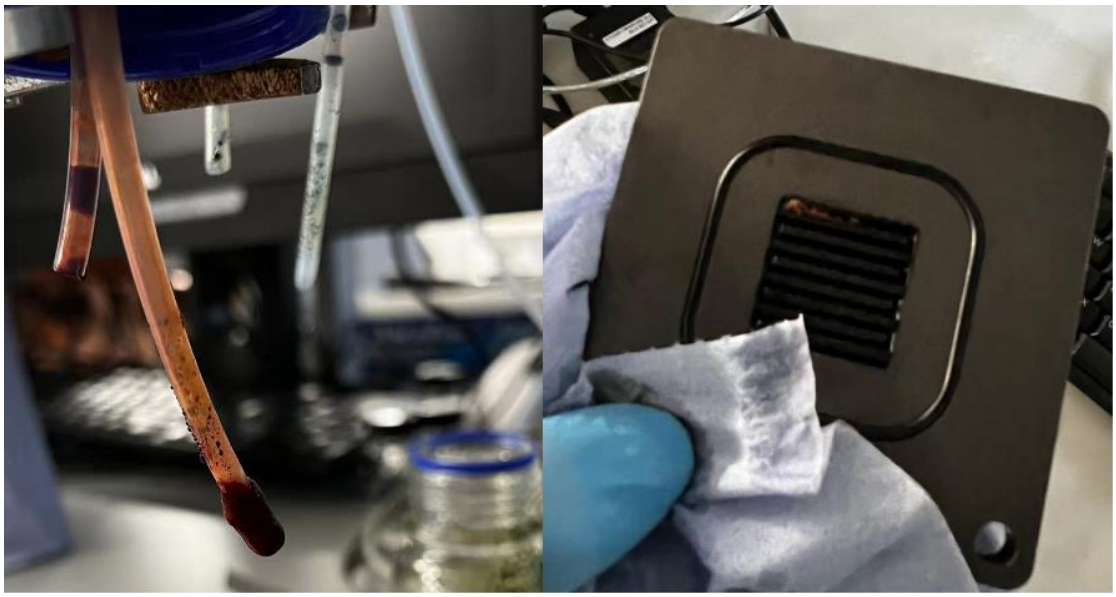

Figure 46 – images showing the blockages formed in the transfer tubing and throughout the current collector in the flow cell respectively.

The key differences between AS' groups cell and ours is that their cell has a surface area of 5 cm^2, uses a different membrane material with a pre-treatment protocol, and they use a different electrode pre-treatment protocol to ours. In addition, their cell operates under a constant flow of nitrogen into the electrolyte tanks rather than working as a sealed system. The constant flow of nitrogen is believed to have contributed towards the blockage during the initial test because **1** was at a high concentration (close to its maximum concentration in water (~0.3 M)); the flow

of nitrogen would have concentrated the solution, in turn precipitating **1** out of solution to cause the blockage in the pipes (see *Figure 46*).

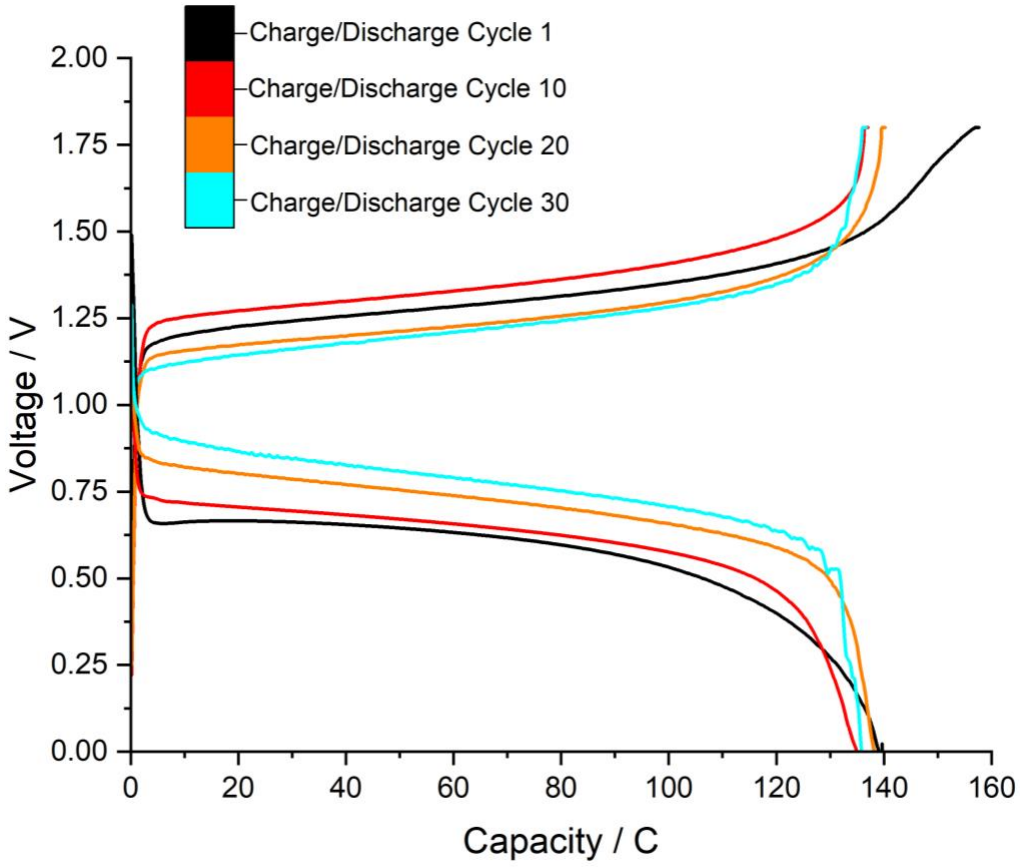

*Figure 47 – Results of flow cell using 0.05 M compound **1** (0.563 g) in 3 M H_2SO_4 (20 cm^3) and 0.1 M $VOSO_4.6H_2O$ (0.542 g) in 3 M H_2SO_4 (20 cm^3). Cycled at ~7.5 $cm^3.min^{-1}$ with a charge/discharge current of 30 $mA.cm^{-2}$ for 30 cycles.*

The system was set up again but this time around using the electrolyte solutions at a quarter of the original concentrations. Electrolytes comprising 0.05 M compound **1** and 0.1 M $VOSO_4$ solutions in 3 M H_2SO_4 supporting electrolyte were used, with the same cell set-up, pre-treatment protocols and flow rate (~7.5 $cm^3.min^{-1}$) as the previous run. The results were positive and as expected from a control experiment using **1**. The cell proved to be highly reversible and stable for the 30 cycles in which it cycled for showing minimal signs of capacity loss and <97% coulombic

efficiency. These results were very similar to that of an AQDS/$VOSO_4$ cell which AS' group have previously studied and collected data for (see *Figure 47* for cell cycling results).

Once the benchmark cell had been established and **1** had proven to work as part of a reversible and stable cell, the couples with $FeSO_4$ were revisited (see chapter 3). The asymmetric system was replicated but to avoid blockages as per the initial vanadium coupled test the concentrations were kept lower. Using a 0.05 M **1** and 0.1 M $FeSO_4$ solutions, the flow cell was set up as per the previous two tests with vanadium and the data collected. However, in this case the results were nearly identical to those seen during earlier flow cell testing as during every cycle there was a major consistent capacity loss until the cell died off after ~15 cycles.

5.3 Beyond the Scope This Project

The beginning of this collaboration was nearing the submission of this research project, and therefore there was not sufficient time to study the previously tested HBr coupled system. Nevertheless, this collaboration will be continued further within the research group with the aim of optimizing the battery performance of **1** and investigating optimal positive redox couples to pair **1** with in a RFB system.

Appendices

Appendix 1: Spectra and Analysis

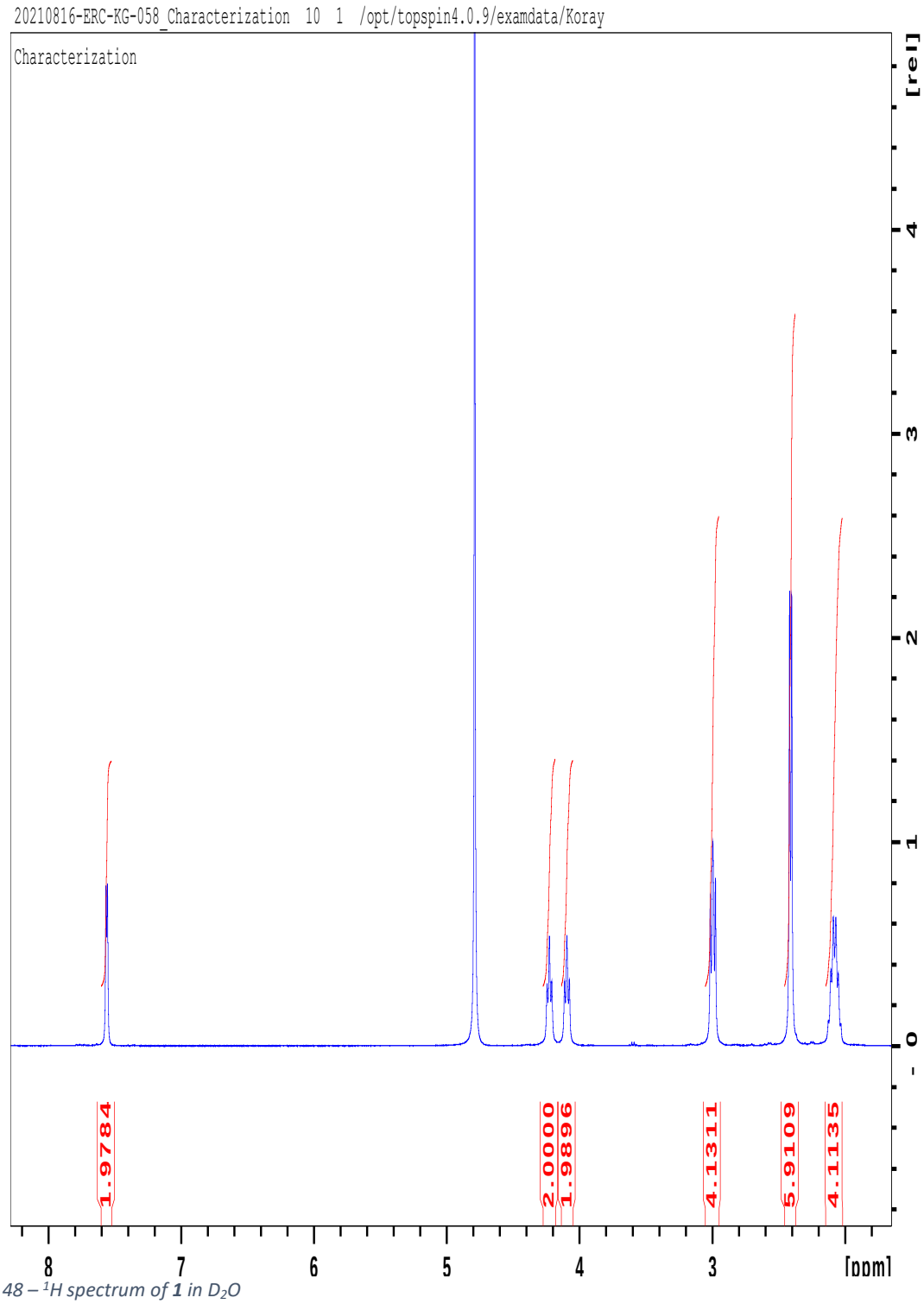

*Figure 48 – ^{1}H spectrum of **1** in D_2O*

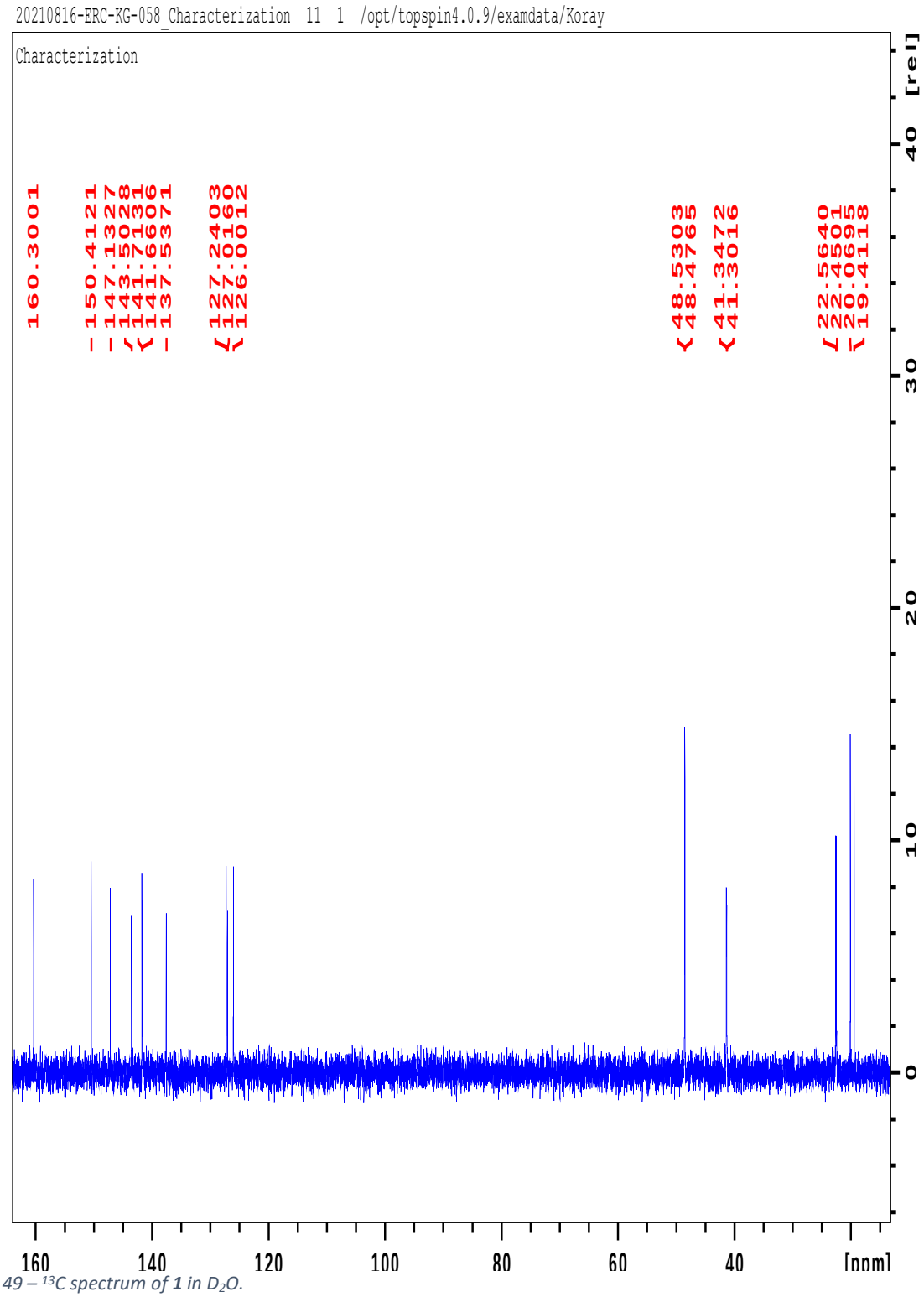

*Figure 49 – ^{13}C spectrum of **1** in D_2O.*

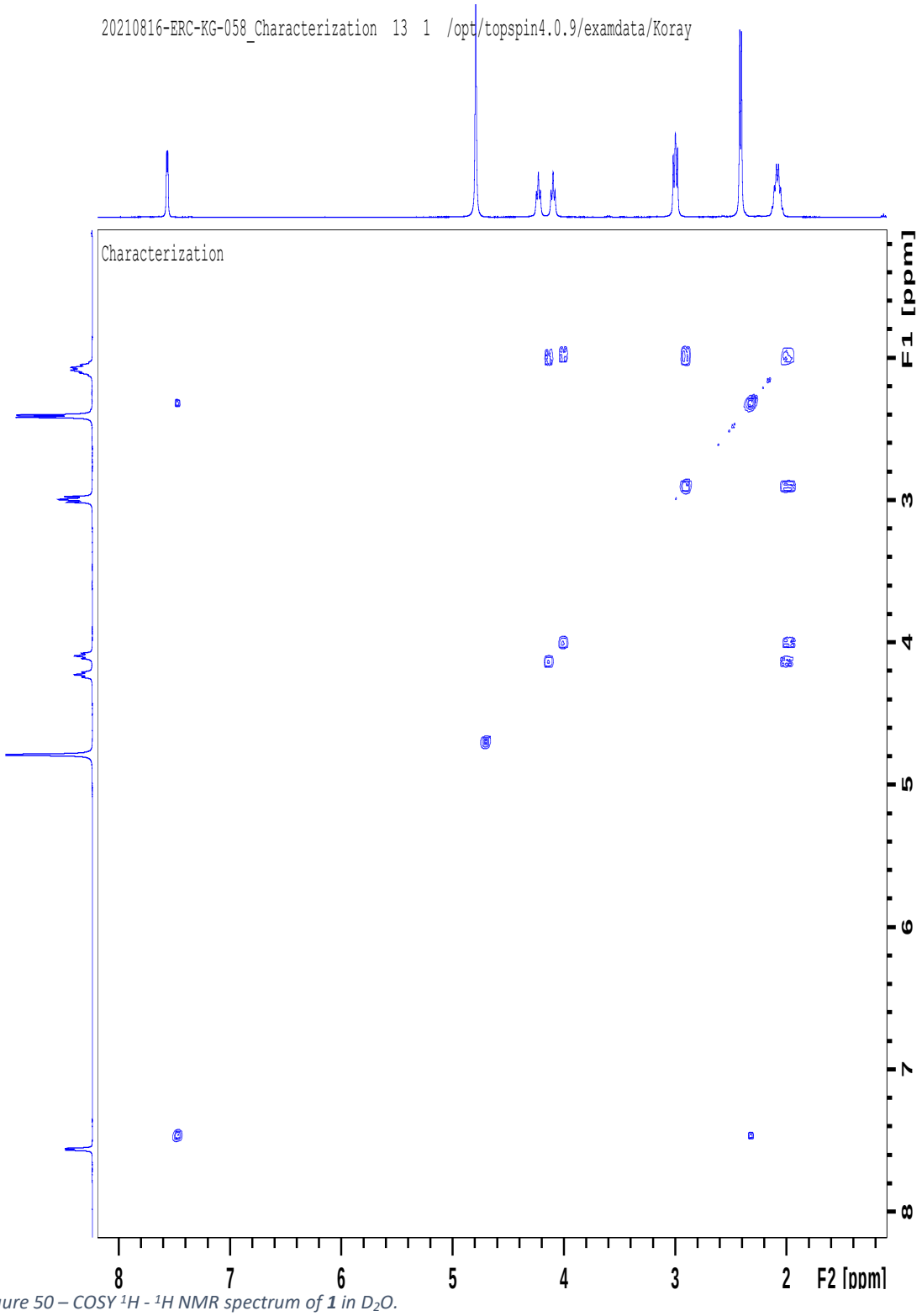

*Figure 50 – COSY ^{1}H - ^{1}H NMR spectrum of **1** in D_2O.*

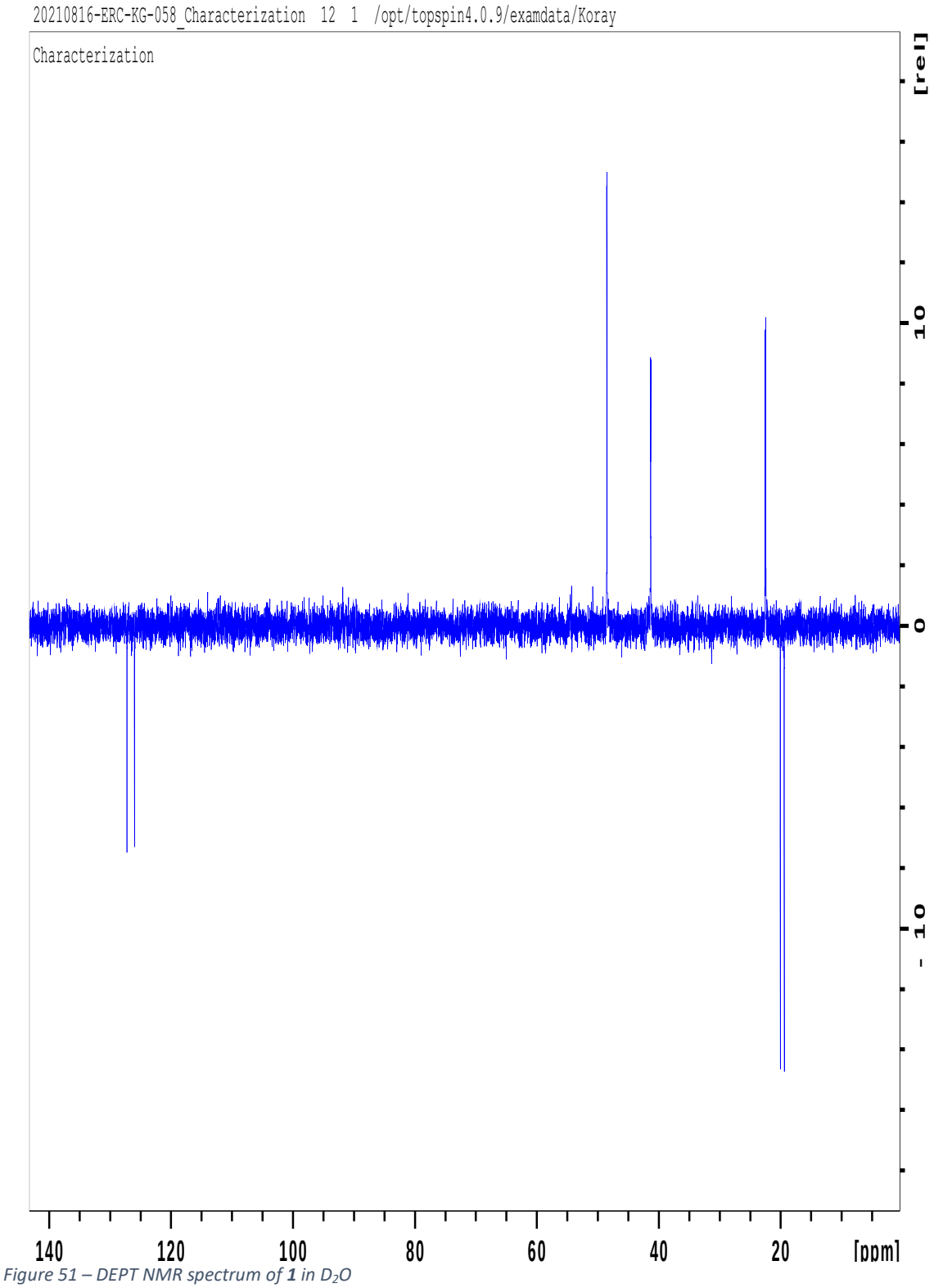

*Figure 51 – DEPT NMR spectrum of **1** in D_2O*

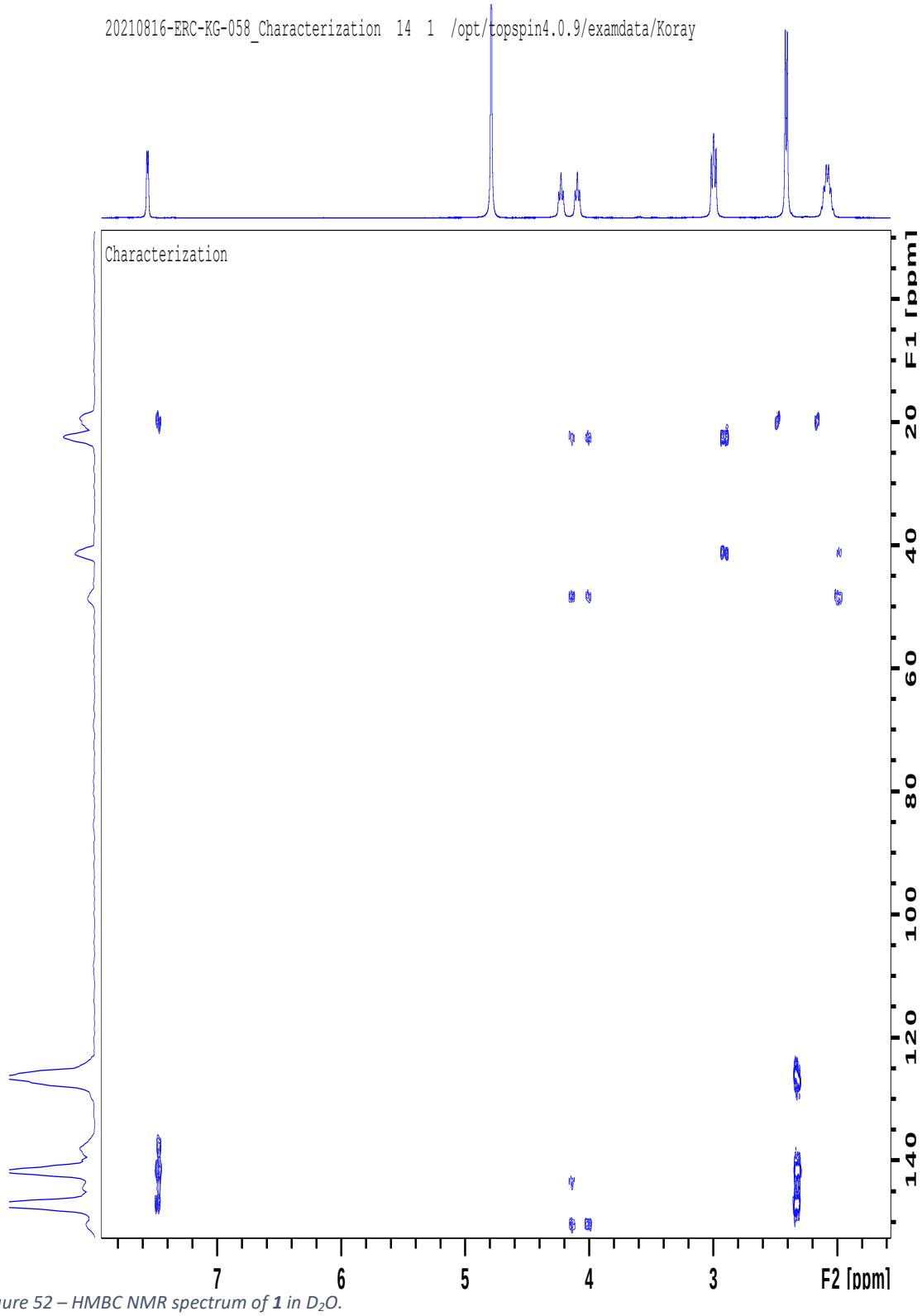

*Figure 52 – HMBC NMR spectrum of **1** in D_2O.*

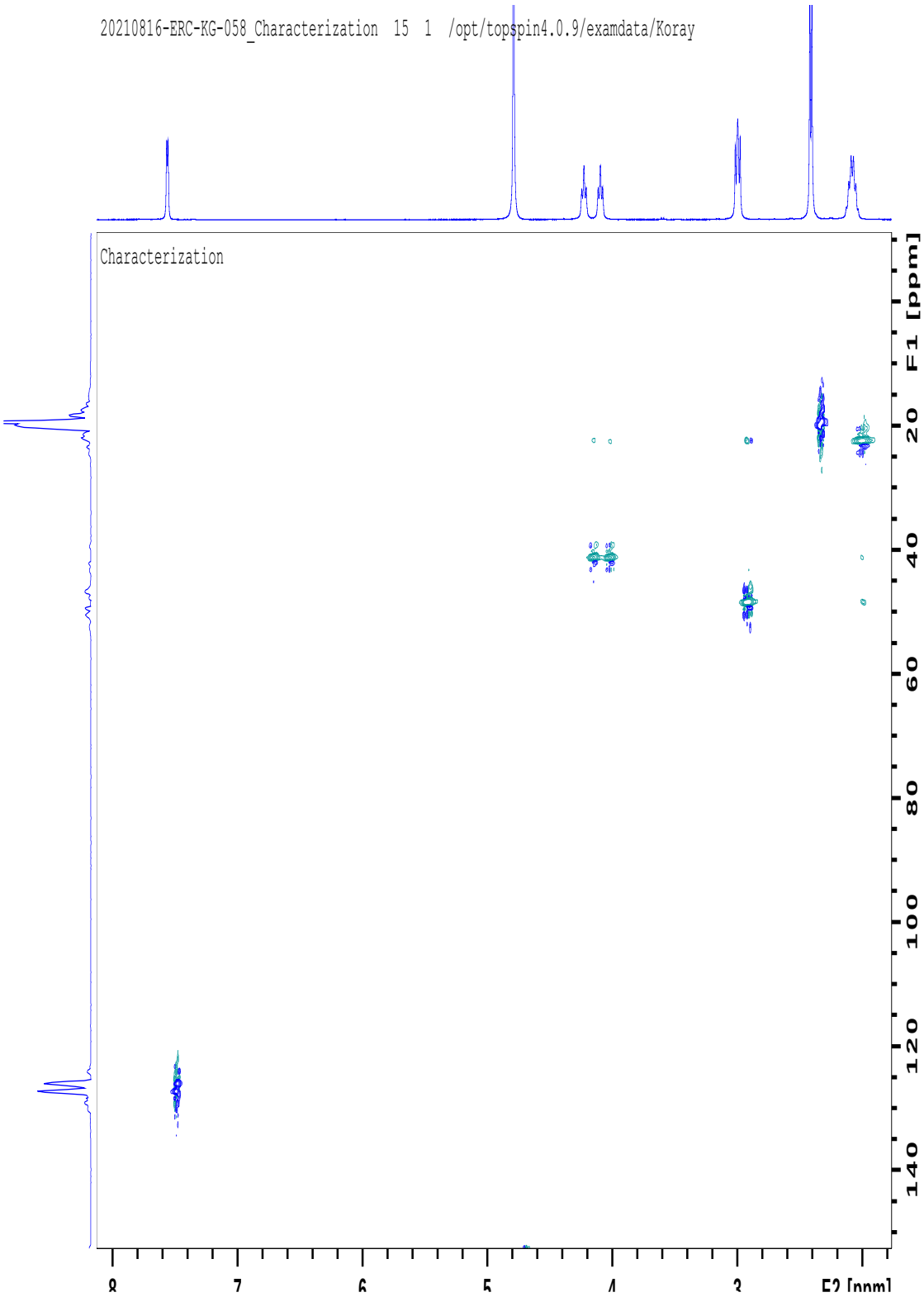

*Figure 53 – HSQC NMR spectrum of **1** in D_2O.*

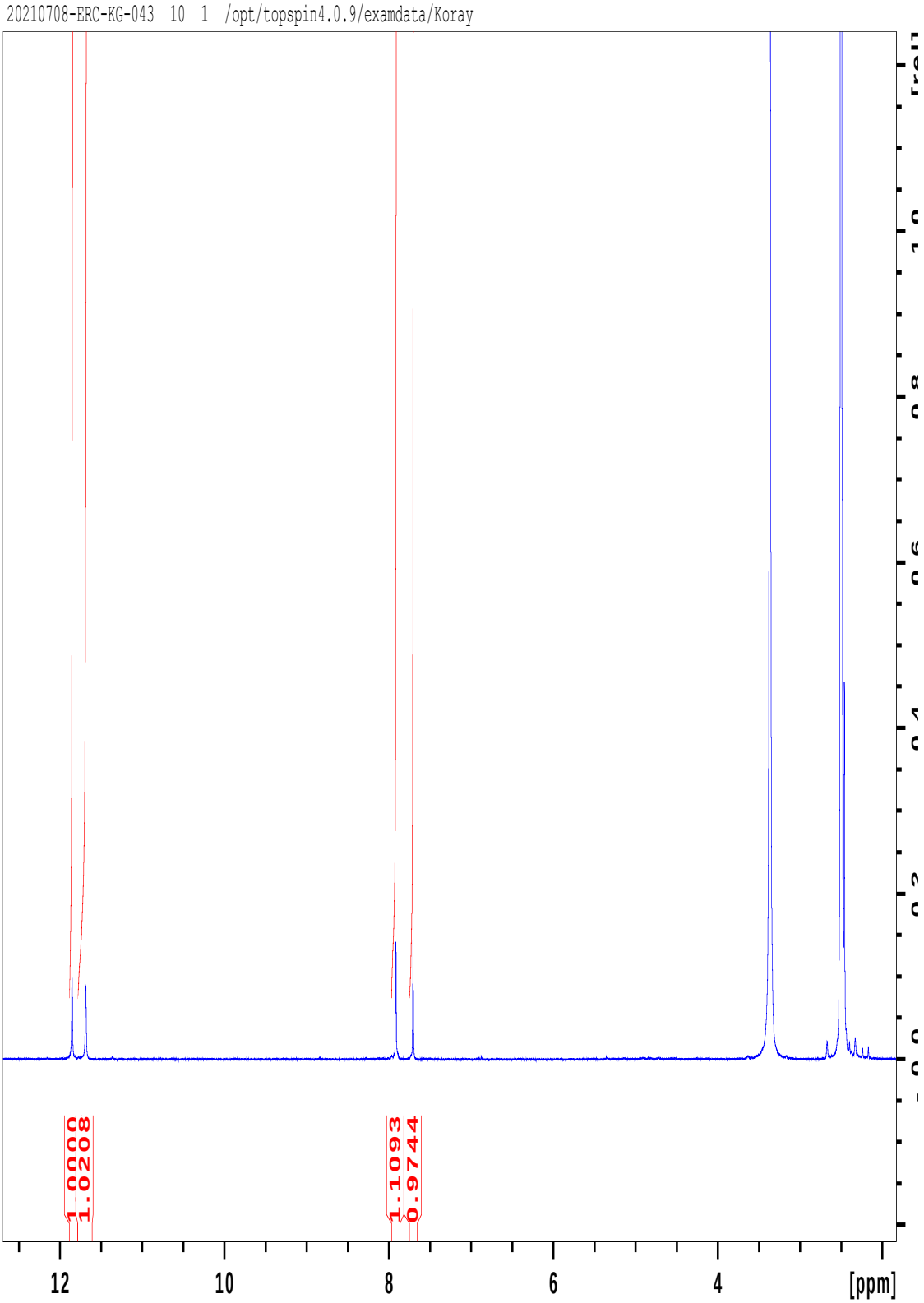

*Figure 54 – ^{1}H spectrum of **lumichrome**.*

LONDON METROPOLITAN UNIVERSITY
HUMAN SCIENCES

Elemental Analysis Sample Results

Name	Koray Gumus
Organisation Name	University of Kent
Purchase order number	807048

Standard – Acetanilide		
Element	**Expected %**	**Found**
Carbon	71.06 (+/- 0.26)	71.03
Hydrogen	6.70 (+/- 0.09)	6.64
Nitrogen	10.36 (+/- 0.18)	10.34

Analysis – KG-058			
Element	**Expected %**	**Found (1)**	**Found (2)**
Carbon	38.4	34.64	34.70
Hydrogen	3.6	3.74	3.78
Nitrogen	10.0	8.72	8.84

Date completed	23.09.2021
Signature	O. McCullough
Comments	

*Figure 55 – CHN elemental analysis results for **1** from an external laboratory.*

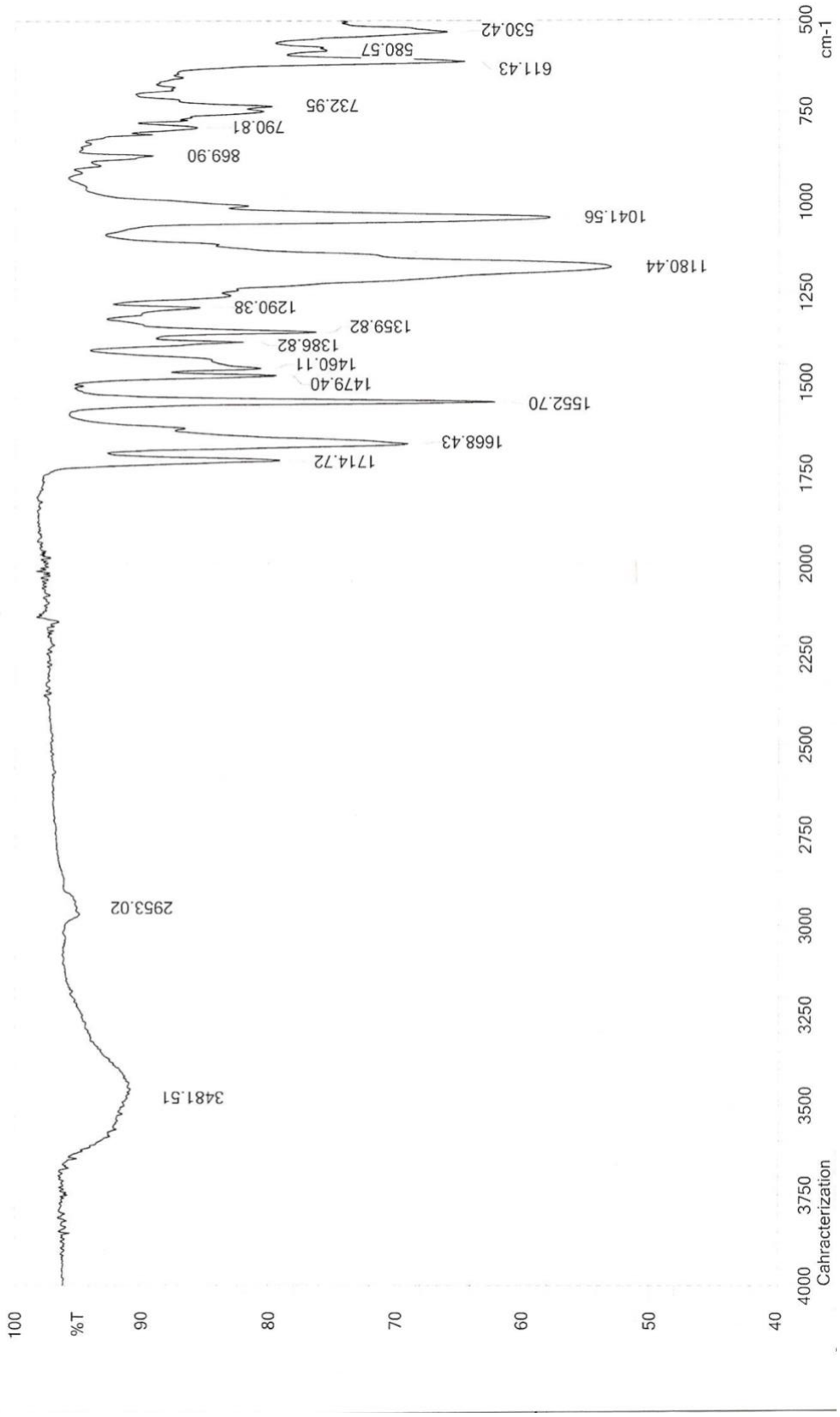

*Figure 56 – FTIR spectrum of **1**.*

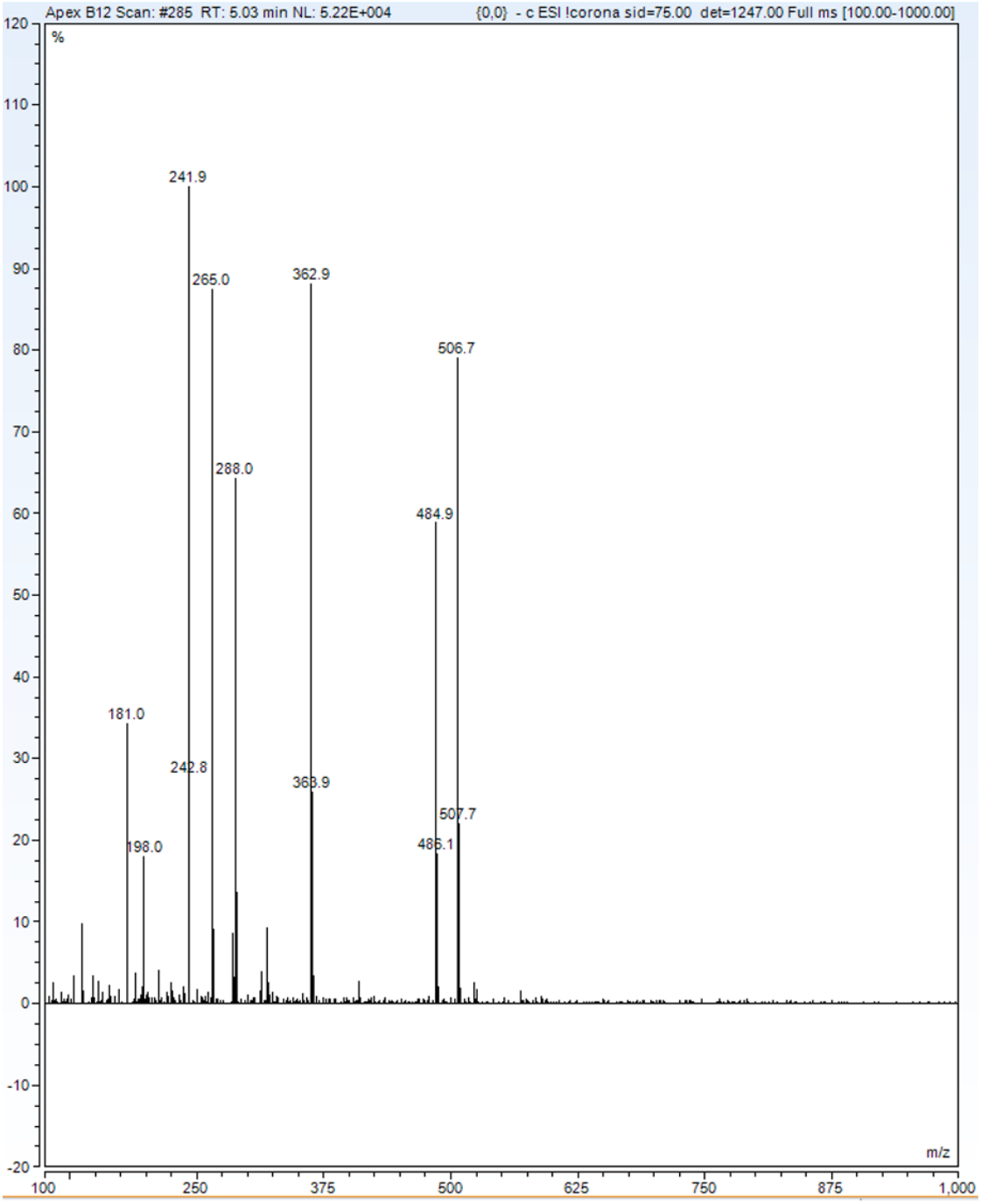

*Figure 57 – LC-MS spectrum of **1**. Isocratic mobile phase H20 + 0.1% Formic Acid : MeOH + 0.1% Formic Acid (v/v 1:1). UV 353. Negative ionisation.*

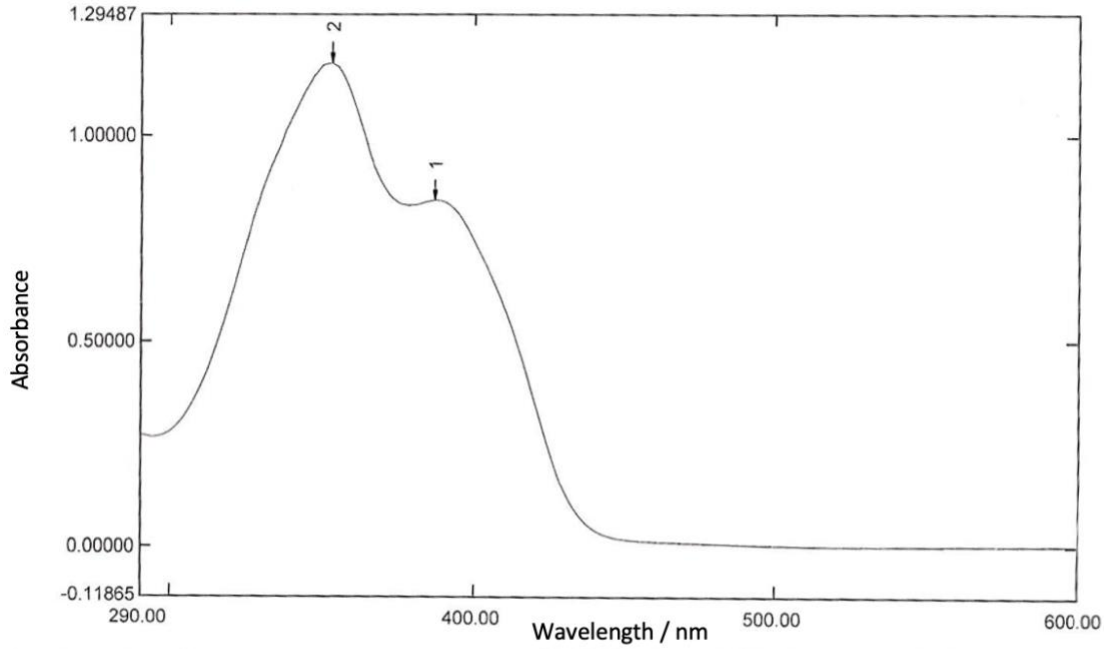

Measurement Properties	
Wavelength Range (nm.):	290.00 to 600.00
Scan Speed:	Fast
Sampling Interval:	1.0
Auto Sampling Interval:	Disabled
Scan Mode:	Single

Instrument Properties	
Instrument Type:	UV-1800 Series
Measuring Mode:	Absorbance
Slit Width:	1.0 nm
Light Source Change Wavelength:	340.0 nm
S/R Exchange:	Normal

No.	Wavelength	Absorbance	Description
1	387.00	0.84055	
2	353.00	1.17708	
3			

*Figure 58 – UV-Vis spectrum of 0.005 M **1** in H_2O.*

Appendix 2: Additional Flow Cell Testing Data

N.B, all flow cell graphs shown here are with all cycles present, whereas for flow cell tests shown in the main body of text are remade and simplified for clarity.

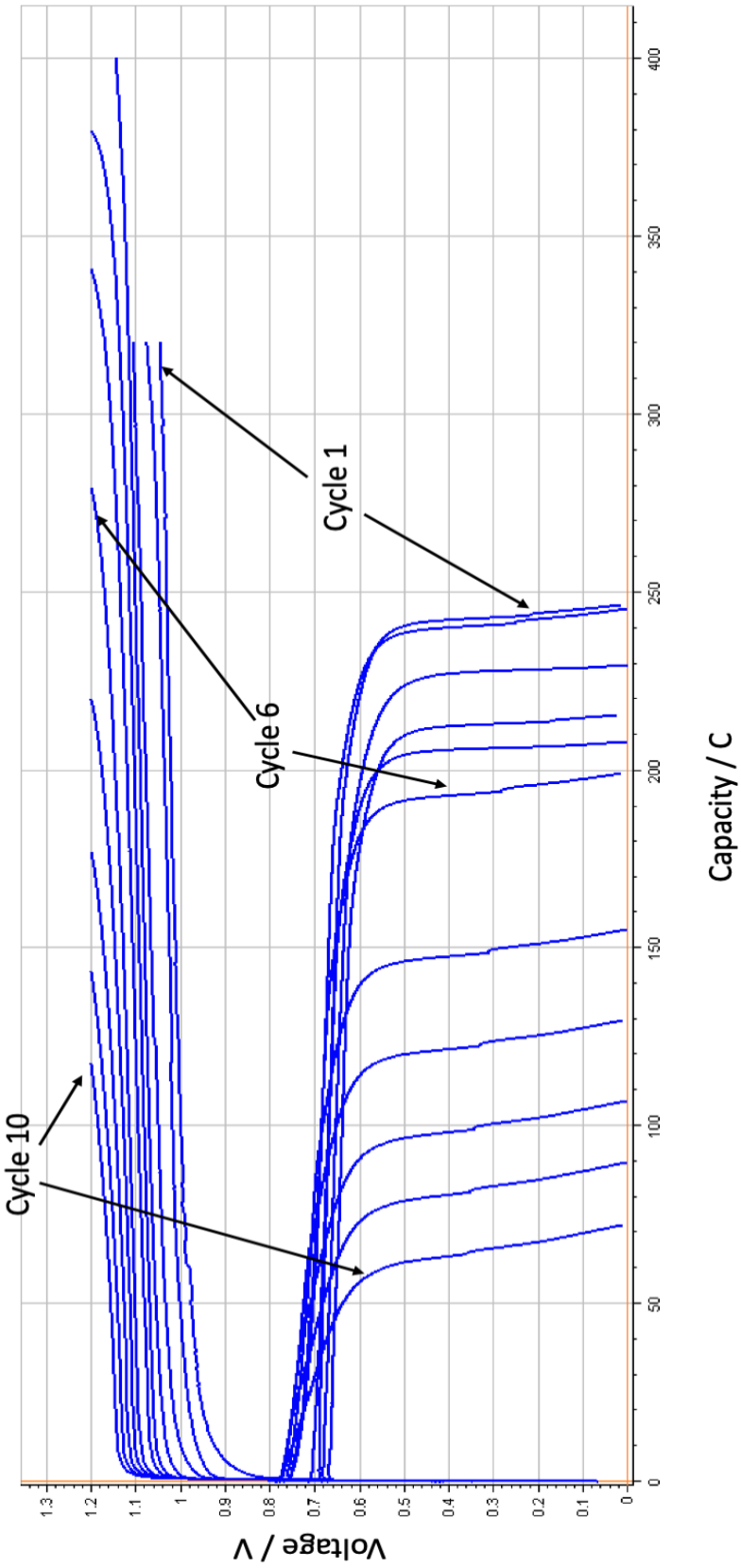

*Figure 59 – Graph showing a flow cell test of 10 cycles. Anolyte: 0.2 M compound **1** (1.75 g) in 3 M H_2SO_4 (15 cm^3). Catholyte: 0.8 M HBr (1.43 cm^3) + 0.4 M MEP (1.17 g) + 1 mM $Br_{2(aq)}$ (0.5 cm^3) all in 3 M H_2SO_4 (14 cm^3). 42 $cm^3.min^{-1}$ flow rate, 2 $mA.cm^{-2}$ charge/discharge current.*

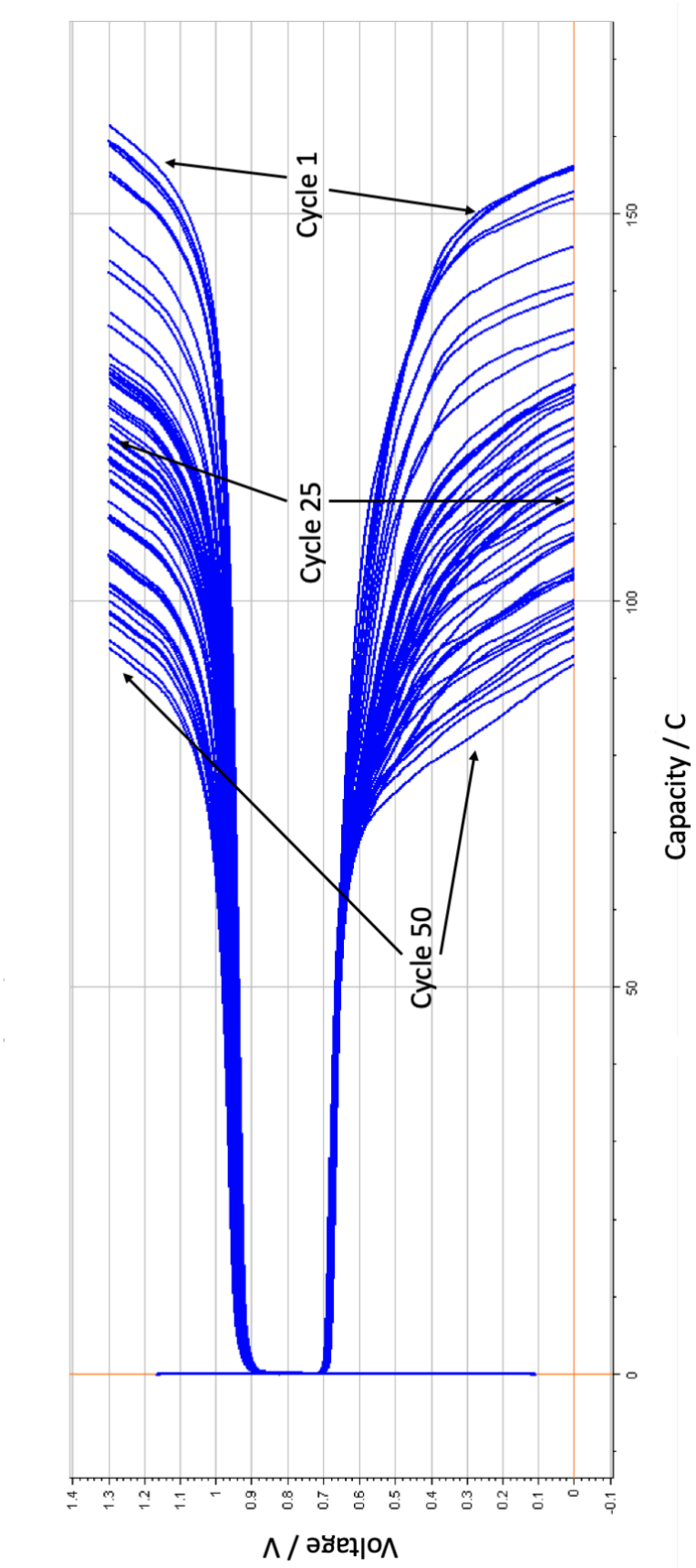

*Figure 60 - Graph showing a flow cell test of 50 cycles. Anolyte: 0.3 M compound **1** (2.02 g) in 3 M H_2SO_4 (12 cm^3). Catholyte: 1.2 M HBr (1.75 cm^3) + 0.9 M MEP (2.27 g) + 1 mM $Br_{2(aq)}$ (0.75 cm^3) all in 3 M H_2SO_4 (11 cm^3). 42 $cm^3.min^{-1}$ flow rate, 4 $mA.cm^{-2}$ charge/discharge current.*

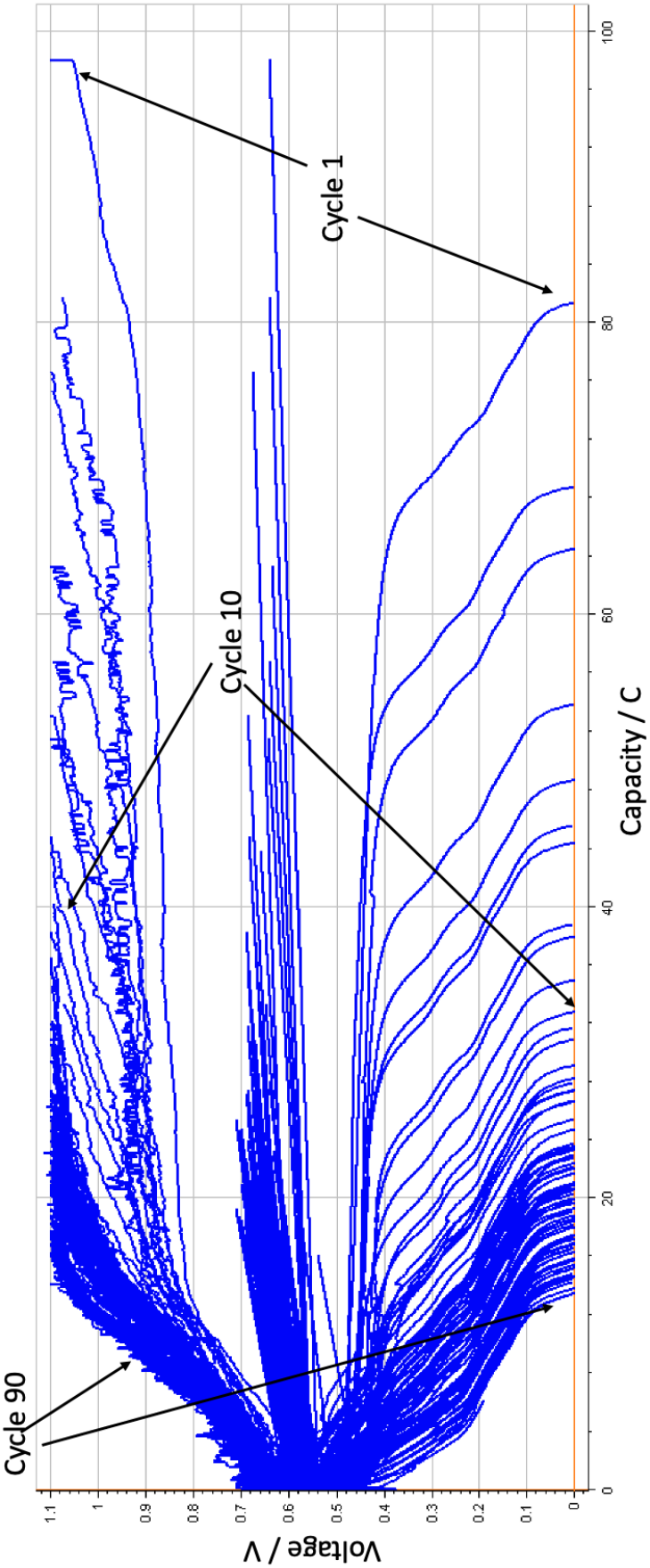

*Figure 61 – Graph showing a flow cell test of 90 cycles. Anolyte: 0.2 M **1** (1.688 g) in 3 M H_2SO_4 (15 cm^3). Catholyte: 0.2 M Tiron (1.245 g) in 3 M H_2SO_4 (15 cm^3). 42 $cm^3.min^{-1}$ flow rate, 2.5 $mA.cm^{-2}$ charge/discharge current.*

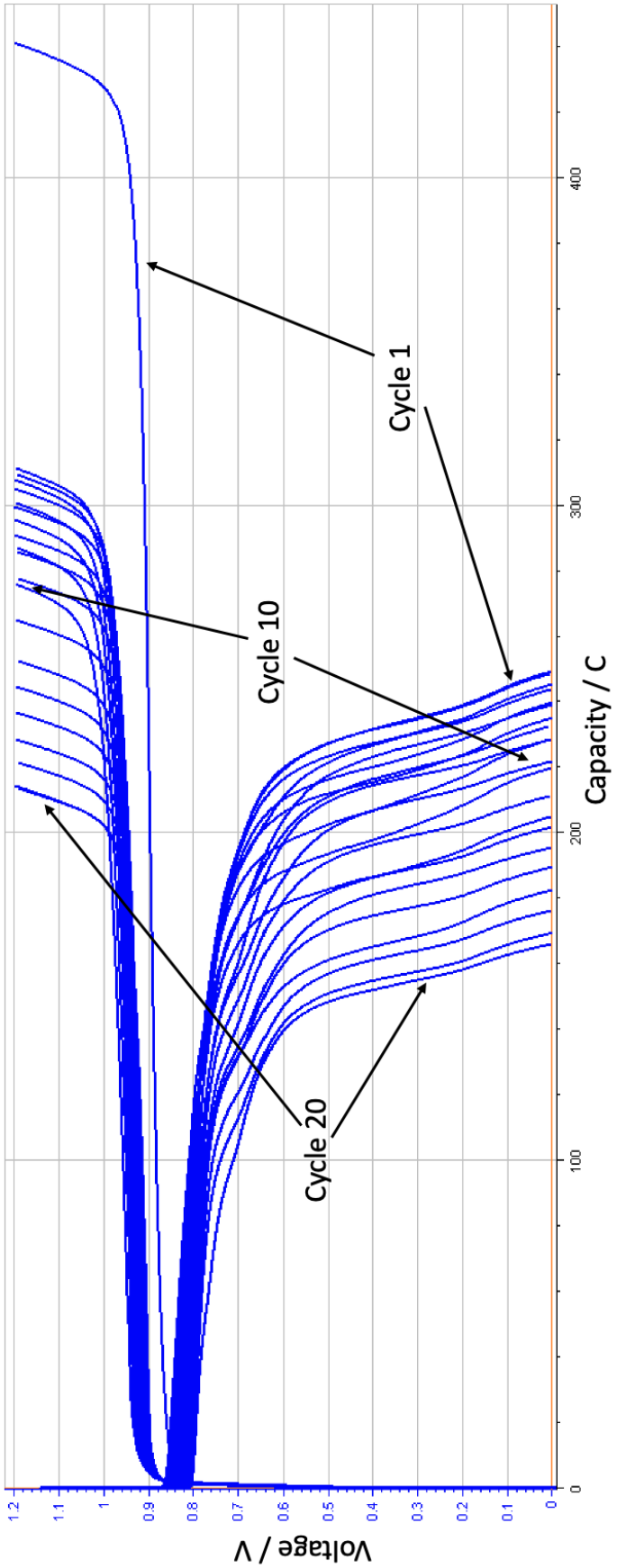

Figure 62 – Graph showing a flow cell test of 20 cycles. Repeat of run reported in Figure 34.

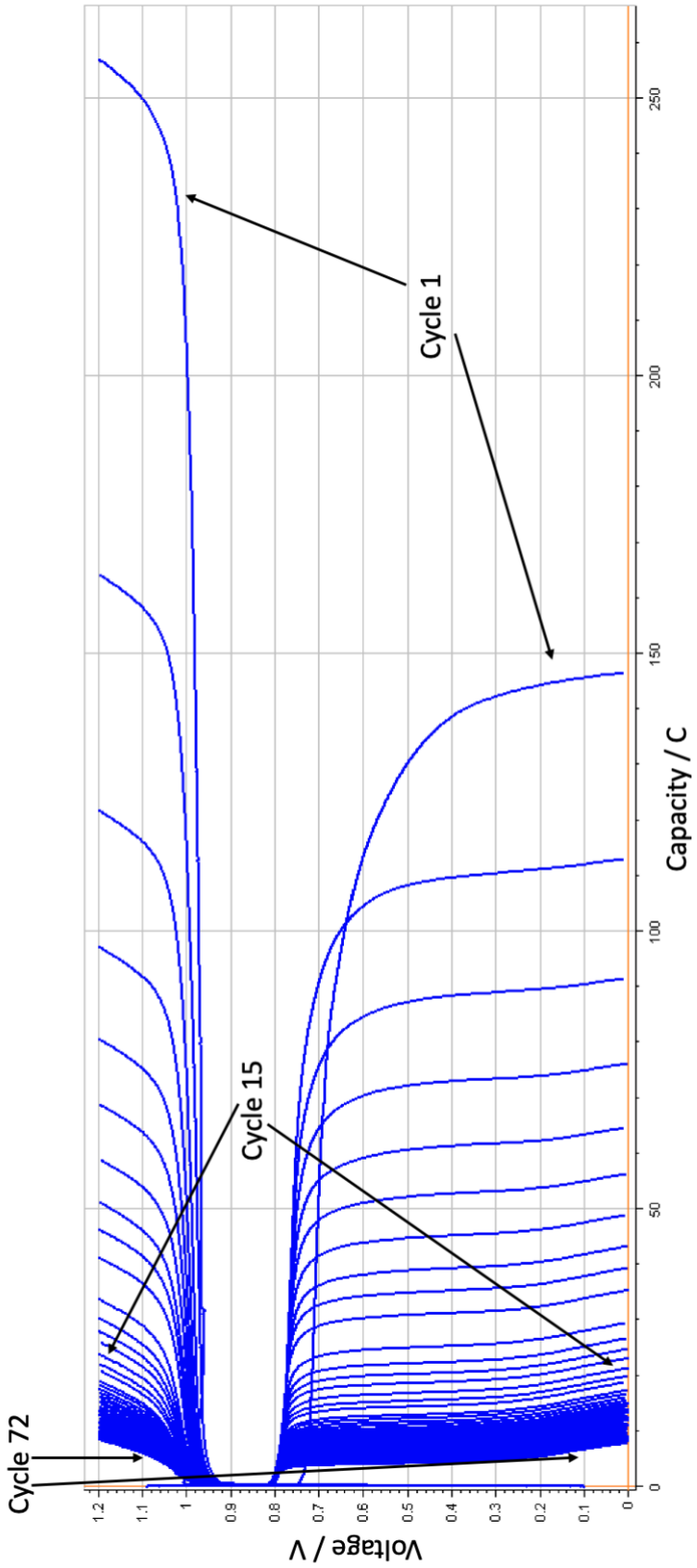

*Figure 63 – Graph showing a flow cell test of 72 cycles. Anolyte: 0.2 M compound **1** (1.75 g) in 3 M H_2SO_4 (12 cm^3). Catholyte: 0.8 M HBr (1.12 cm^3) + 0.6 M MEP (1.38 g) + 1 mM $Br_{2(aq)}$ (0.25 cm^3) all in 3 M H_2SO_4 (11 cm^3). 42 $cm^3.min^{-1}$ flow rate, 5 $mA.cm^{-2}$ charge/discharge current.*

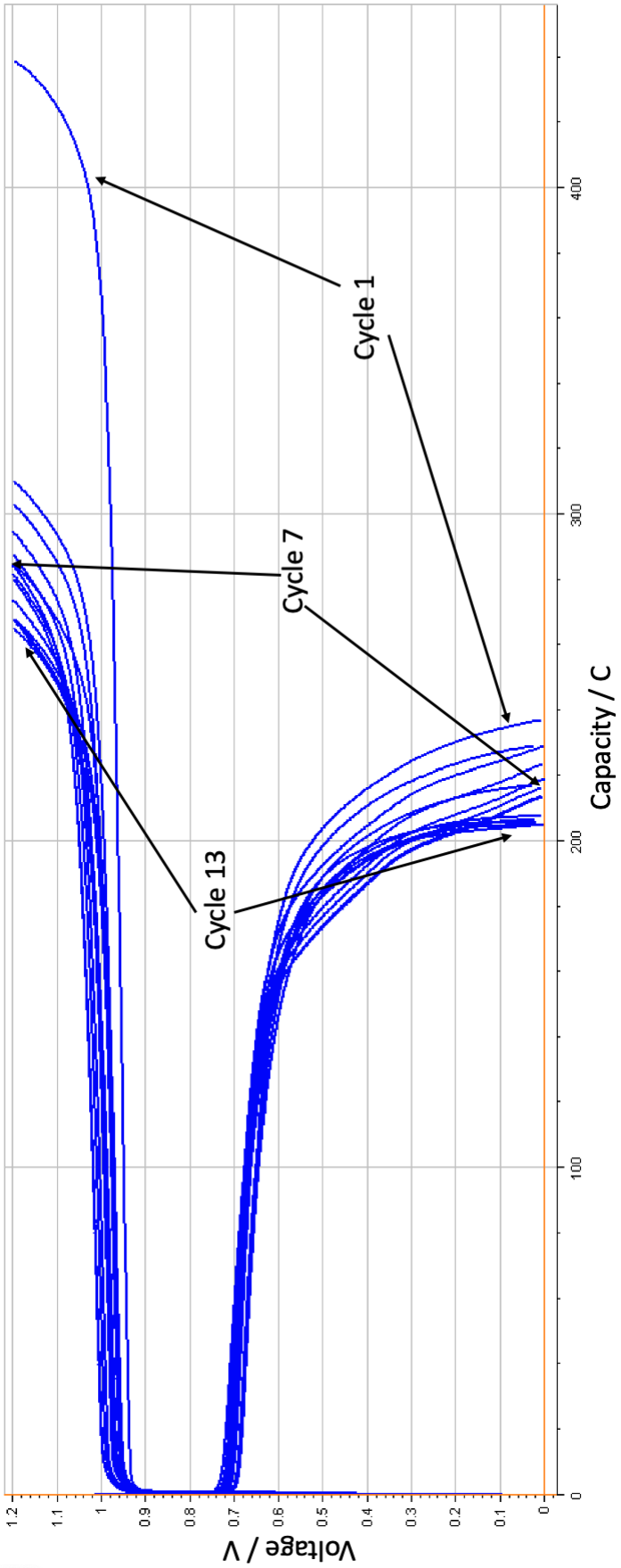

Figure 64 – Graph showing a flow cell test of 13 cycles. Repeat of run reported in Figure 34, only differences are new peristaltic pump and 50 $cm^3.min^{-1}$ flow rate used.

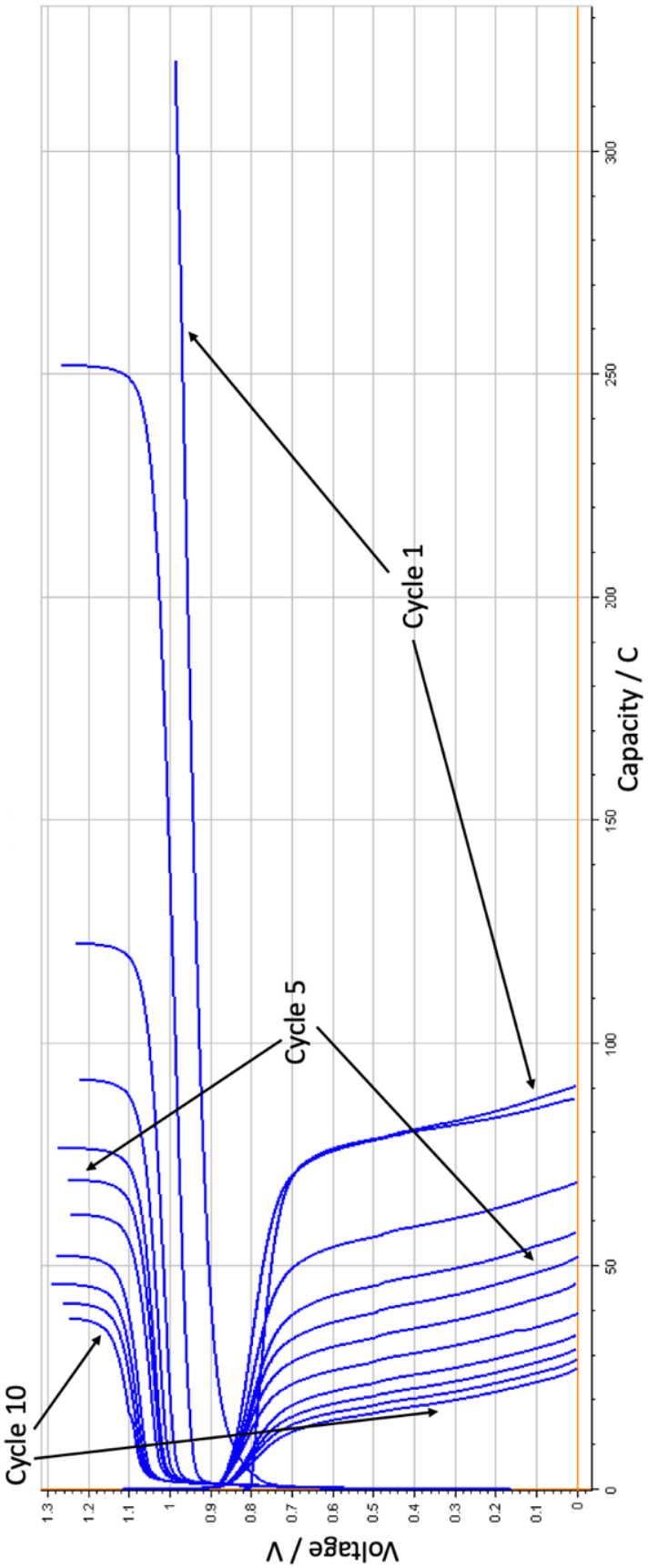

*Figure 65 – Graph showing a flow cell test of 10 cycles. Anolyte: 0.25 M **1** (1.41 g) in in 2 M H_2SO_4 (15 cm^3). Catholyte 0.25 M HBr (0.45 cm^3) in in 2 M H_2SO_4 (15 cm^3). 42 $cm^3.min^{-1}$ flow rate, 1.5 $mA.cm^{-2}$ charge/discharge current.*

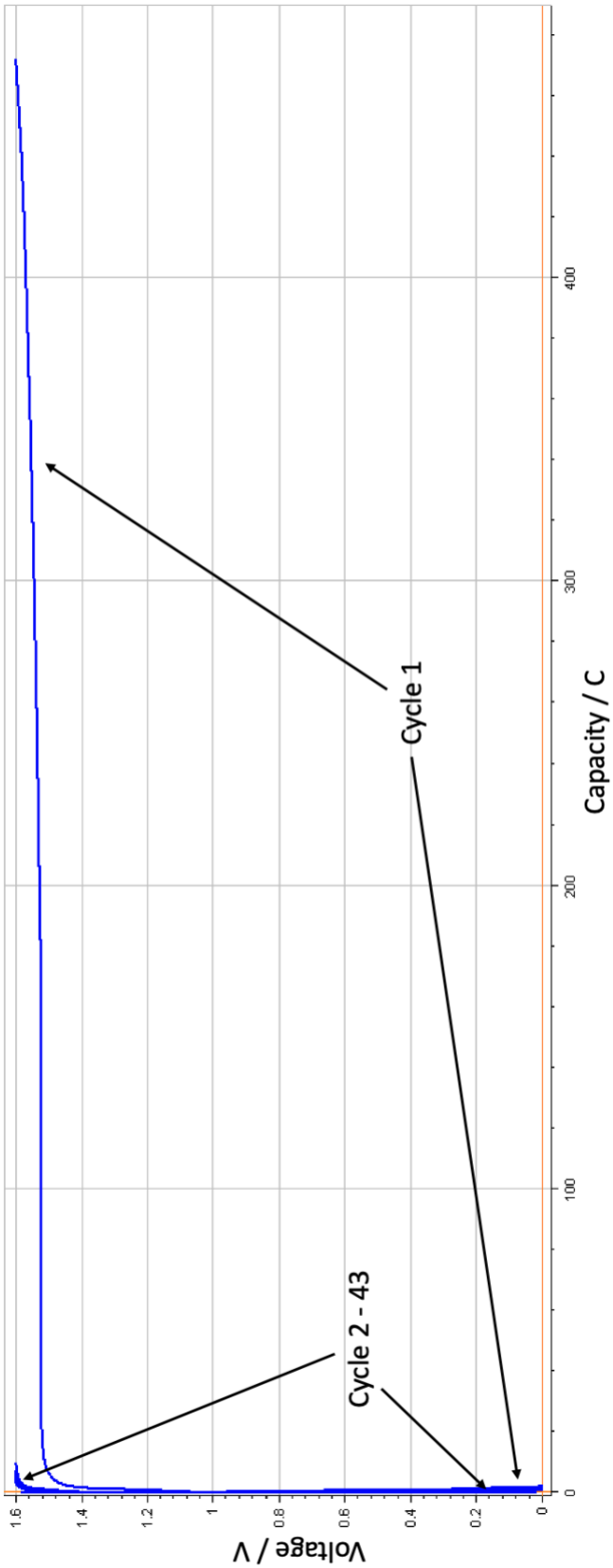

Figure 66 – Graph showing flow cell test of 43 cycles. Anolyte and catholyte, equal parts of 0.25 M $V^{3.5+}$ complex in 2 M H_2SO_4 (15 cm^3) on both sides. 50 $cm^3.min^{-1}$ flow rate, 4 $mA.cm^{-2}$ charge/discharge current

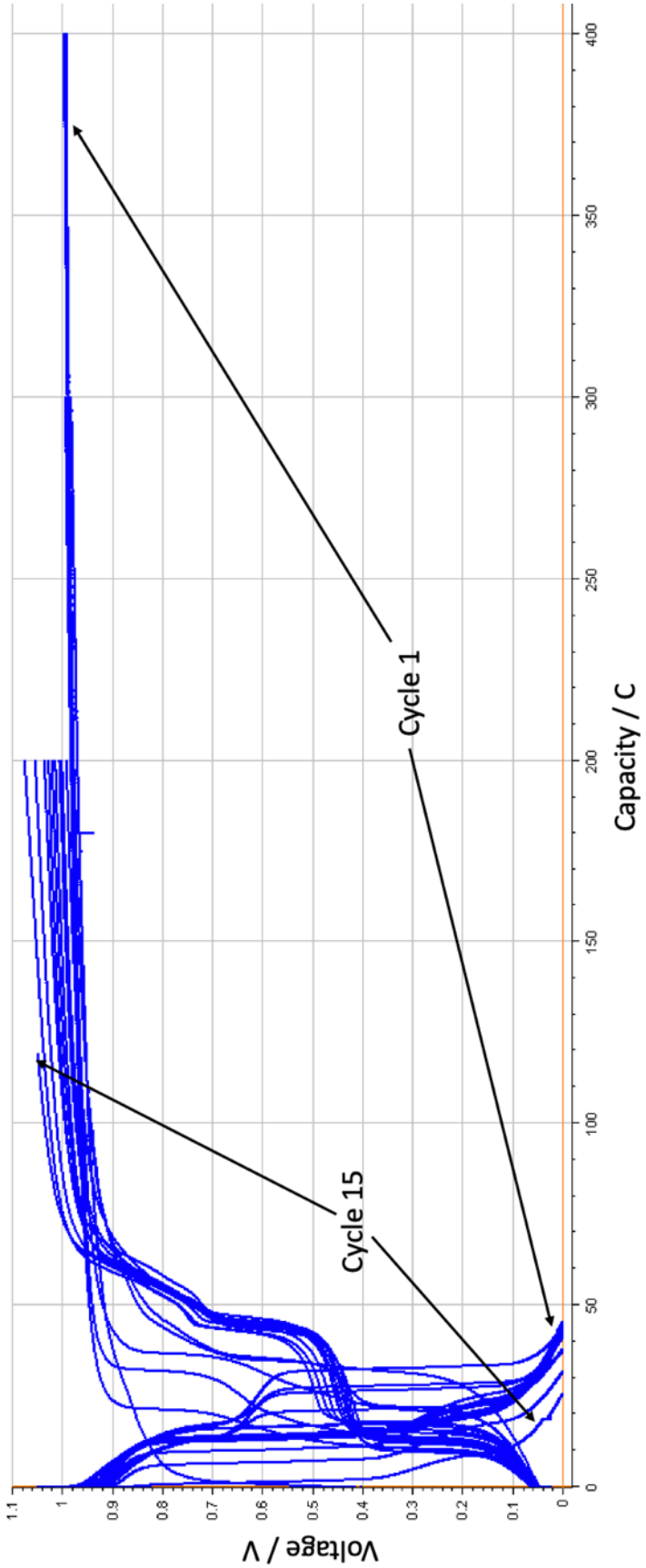

*Figure 67 – Graph showing a flow cell test of 15cycles. Anolyte 0.1 M **1** (0.675 g) in 1 M H_2SO_4 (15 cm^3) as the anolyte and 0.5 M HBr (0.89 cm^3) in 1 M H_2SO_4 (15 cm^3). 42 $cm^3.min^{-1}$ flow rate, 1 $mA.cm^{-2}$ charge/discharge current*

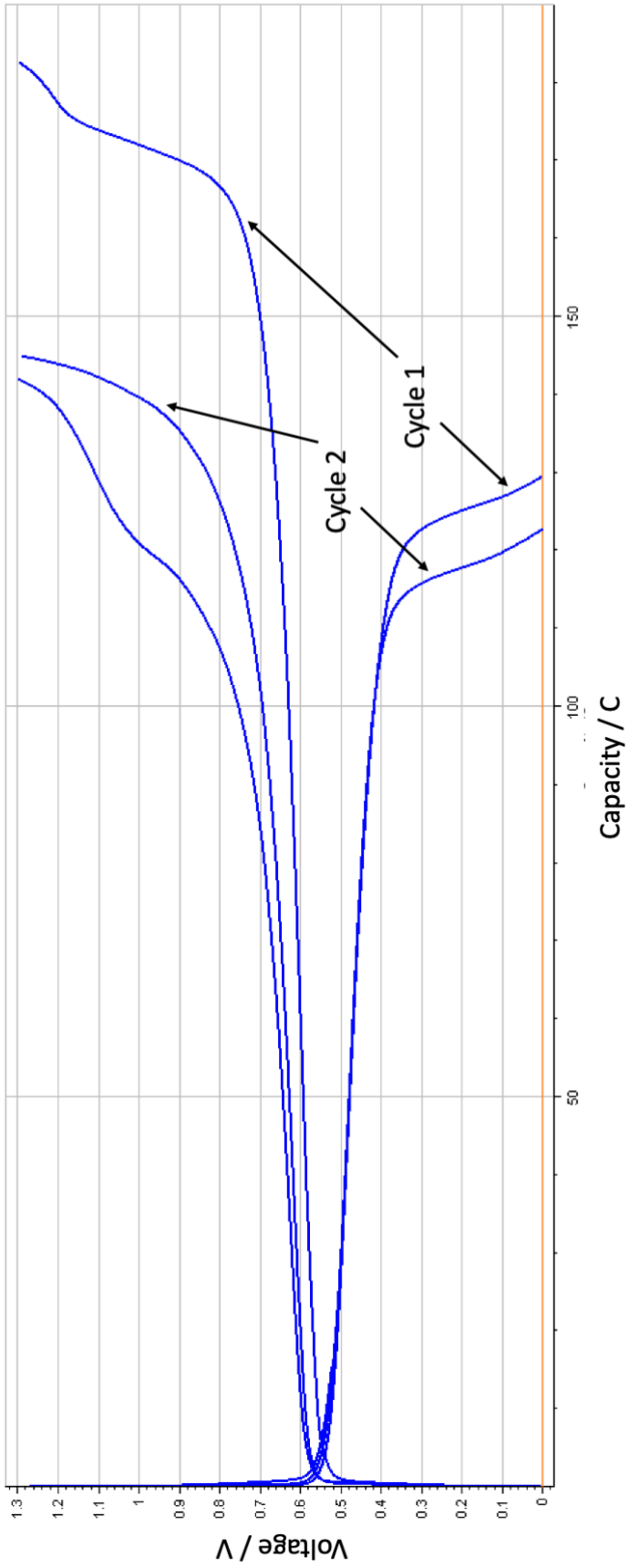

Figure 68 – Identical repeat of flow cell test described in Figure 29.

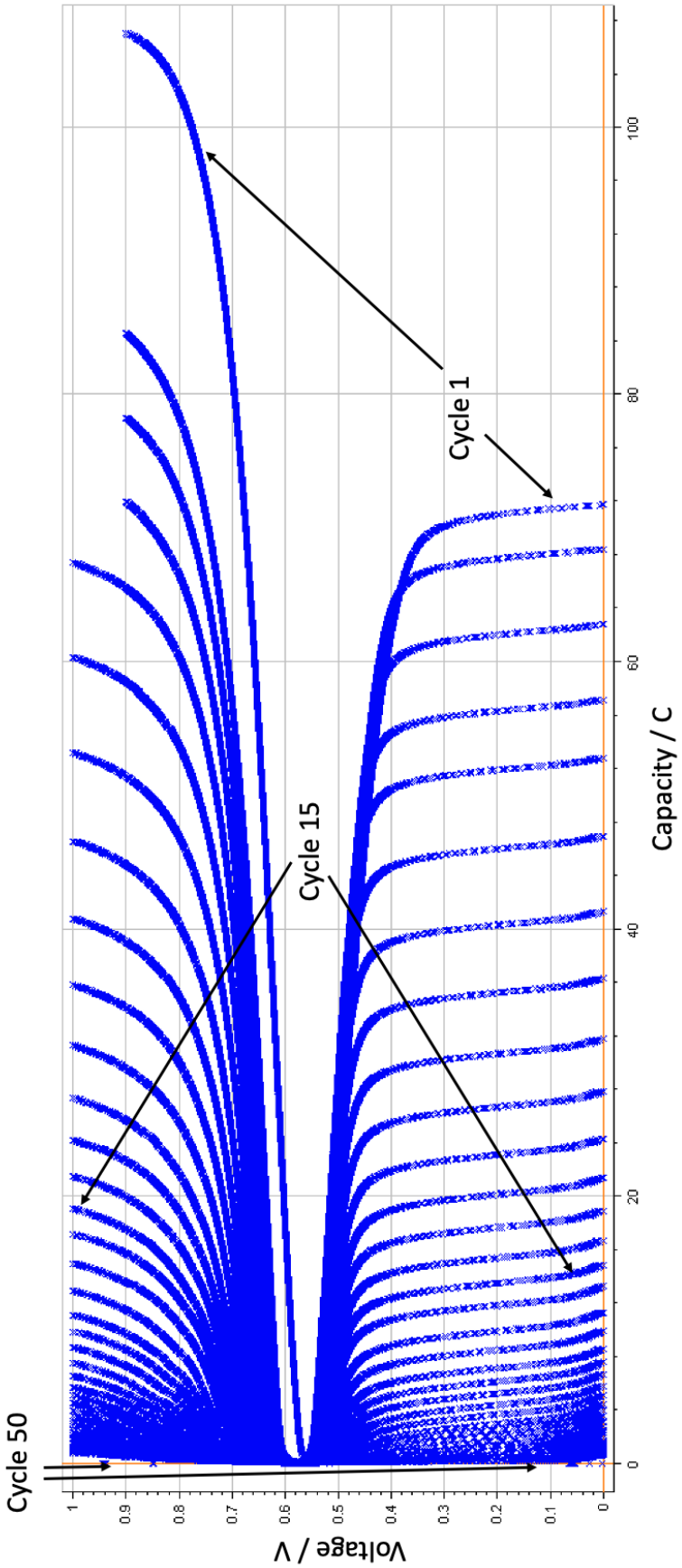

*Figure 69 – Graph showing a flow cell test of 50 cycles. Anolyte and catholyte identical on both sides: 0.2 M **1** (1.35 g) and 0.4 M $FeSO_4.7H_2O$ (1.33 g) in 2 M H_2SO_4 (12 cm^3). 50 $cm^3.min^{-1}$ flow rate, 3 $mA.cm^{-2}$ charge/discharge current. Graph reported in mA.h. mA.h x 3.6 = capacity in Coulombs.*

References

1 J. T. Stock and M. V. Orna, *Electrochemistry, Past and Present*, ACS, Washington, DC, 1989, vol. 1.

2 W. R. Browne, *Electrochemistry*, Oxford University Press, Oxford, 1st edn., 2019.

3 C. M. A. Brett and A. M. Oliveira. Brett, *Electrochemistry : principles, methods, and applications*, Oxford University Press, 1993.

4 J. B. Goodenough and A. Manthiram, *MRS Commun*, 2014, **4**, 135–142.

5 J. Noack, N. Roznyatovskaya, T. Herr and P. Fischer, *Angewandte Chemie*, 2015, **127**, 9912–9947.

6 N. H. Hagedorn, *NASA Redox Storage System Development Project*, 1984.

7 E. Sánchez-Díez, E. Ventosa, M. Guarnieri, A. Trovò, C. Flox, R. Marcilla, F. Soavi, P. Mazur, E. Aranzabe and R. Ferret, *J Power Sources*, 2020, **481**, 1–23.

8 M. Rychcik and M. Skyllas-Kazacos, *J Power Sources*, 1988, **22**, 59–61.

9 V. Singh, S. Kim, J. Kang and H. R. Byon, *Nano Res*, 2019, **12**, 1988–2001.

10 J. M. Cameron, C. Holc, A. J. Kibler, C. L. Peake, D. A. Walsh, G. N. Newton and L. R. Johnson, *Chem Soc Rev*, 2021, **50**, 5863–5883.

11 Y. Chen, S. A. Freunberger, Z. Peng, O. Fontaine and P. G. Bruce, *Nat Chem*, 2013, **5**, 489–494.

12 K. Lin, R. Gómez-Bombarelli, E. S. Beh, L. Tong, Q. Chen, A. Valle, A. Aspuru-Guzik, M. J. Aziz and R. G. Gordon, *Nat Energy*, 2016, **1**, 1–8.

13 P. S. Guin, S. Das and P. C. Mandal, *International Journal of Electrochemistry*, 2011, 1–22.

14 D. G. Kwabi, K. Lin, Y. Ji, E. F. Kerr, M. A. Goulet, D. De Porcellinis, D. P. Tabor, D. A. Pollack, A. Aspuru-Guzik, R. G. Gordon and M. J. Aziz, *Joule*, 2018, **2**, 1894–1906.

15 M. Burgess, E. Chénard, K. Hernández-Burgos, G. Nagarjuna, R. S. Assary, J. Hui, J. S. Moore and J. Rodríguez-López, *Chemistry of Materials*, 2016, **28**, 7362–7374.

16 S. Jin, E. M. Fell, L. Vina-Lopez, Y. Jing, P. W. Michalak, R. G. Gordon and M. J. Aziz, *Adv Energy Mater*, 2020, **10**, 1–10.

17 A. Permatasari, W. Lee and Y. Kwon, *Chemical Engineering Journal*, 2020, **383**, 1–8.

18 J. B. Gerken, C. W. Anson, Y. Preger, P. G. Symons, J. D. Genders, Y. Qiu, W. Li, T. W. Root and S. S. Stahl, *Adv Energy Mater*, 2020, **10**, 1–7.

19 B. Huskinson, M. P. Marshak, C. Suh, S. Er, M. R. Gerhardt, C. J. Galvin, X. Chen, A. Aspuru-Guzik, R. G. Gordon and M. J. Aziz, *Nature*, 2014, **505**, 195–198.

20 Q. Xu, Y. N. Ji, L. Y. Qin, P. K. Leung, F. Qiao, Y. S. Li and H. N. Su, *J Energy Storage*, 2018, **16**, 108–115.

21 S. H. Shin, S. H. Yun and S. H. Moon, *RSC Adv*, 2013, **3**, 9095–9116.

22 H. J. Powers, *Am J Clin Nutr*, 2003, **77**, 1352–1360.

23 A. C. S. de Souza, L. Kodach, F. R. Gadelha, C. L. Bos, A. D. M. Cavagis, H. Aoyama, M. P. Peppelenbosch and C. V. Ferreira, *Apoptosis*, 2006, **11**, 1761–1771.

24 N. Jürgensen, M. Ackermann, T. Marszalek, J. Zimmermann, A. J. Morfa, W. Pisula, U. H. F. Bunz, F. Hinkel and G. Hernandez-Sosa, *ACS Sustain Chem Eng*, 2017, **5**, 5368–5372.

25 D. G. Kwabi, Y. Ji and M. J. Aziz, *Chem Rev*, 2020, **120**, 6467–6489.

26 Y. Ji, M. A. Goulet, D. A. Pollack, D. G. Kwabi, S. Jin, D. De Porcellinis, E. F. Kerr, R. G. Gordon and M. J. Aziz, *Adv Energy Mater*, 2019, **9**, 1–7.

27 K. Lin, R. Gómez-Bombarelli, E. S. Beh, L. Tong, Q. Chen, A. Valle, A. Aspuru-Guzik, M. J. Aziz and R. G. Gordon, *Nat Energy*, 2016, **1**, 1–8.

28 B. Huskinson, M. P. Marshak, C. Suh, S. Er, M. R. Gerhardt, C. J. Galvin, X. Chen, A. Aspuru-Guzik, R. G. Gordon and M. J. Aziz, *Nature*, 2014, **505**, 195–198.

29 A. J. Bard and L. R. Faulkner, *Electrochemical methods: Fundamentals and Applications*, 2000, vol. 1.

30 N. Elgrishi, K. J. Rountree, B. D. McCarthy, E. S. Rountree, T. T. Eisenhart and J. L. Dempsey, *J Chem Educ*, 2018, **95**, 197–206.

31 R. S. Nicholson and I. Shain, *Anal Chem*, 1964, 706–723.

32 S. Chen, M. S. Hossain and F. W. Foss, *Org Lett*, 2012, **14**, 2806–2809.

33 K. Yamamoto and Y. Asano, *Appl Environ Microbiol*, 2015, **81**, 7360–7367.

34 R. Huang, J. K. Hyun and D. B. Min, *J Agric Food Chem*, 2006, **54**, 2359–2364.

35 K. Gumus, *Unpublished Work Within Research Group*.

36 A. Kormányos, M. S. Hossain, G. Ghadimkhani, J. J. Johnson, C. Janáky, N. R. de Tacconi, F. W. Foss, Y. Paz and K. Rajeshwar, *Chemistry - A European Journal*, 2016, **22**, 9209–9217.

37 A. A. Lindén, M. Johansson, N. Hermanns and J. E. Bäckvall, *Journal of Organic Chemistry*, 2006, **71**, 3849–3853.

38 T. Sakai, T. Kumoi, T. Ishikawa, T. Nitta and H. Iida, *Org Biomol Chem*, 2018, **16**, 3999–4007.

39 M. A. Gamal-Eldin and D. H. Macartney, *Org Biomol Chem*, 2013, **11**, S1–S18.

40 T. Sakai, T. Kumoi, T. Ishikawa, T. Nitta and H. Iida, *Org Biomol Chem*, 2018, **16**, 3999–4007.

41 S. Bauer, J. C. Namyslo, D. E. Kaufmann and T. Turek, *J Electrochem Soc*, 2020, **167**, 110522.

42 A. W. Hoffman, *Philosophical Transactions*, 1851, **141**, 357–398.

43 W. S. MCNUTT, *J Biol Chem*, 1956, **219**, 365–373.

44 Y. Xu, Y. H. Wen, J. Cheng, G. P. Cao and Y. S. Yang, *Electrochim Acta*, 2010, **55**, 715–720.

45 Y. Xu, Y. H. Wen, J. Cheng, G. P. Cao and Y. S. Yang, *Adv Mat Res*, 2012, **396–398**, 1730–1735.

46 J. B. Gerken, A. Stamoulis, S. E. Suh, N. D. Fischer, Y. J. Kim, I. A. Guzei and S. S. Stahl, *Chemical Communications*, 2020, **56**, 1199–1202.

47 J. B. Gerken, A. Stamoulis, S.-E. Suh, N. D. Fischer, Y. J. Kim, I. A. Guzei and S. S. Stahl, *Chemical Communications*, 2020, **56**, S1–S36.

48 J. Noack, N. Roznyatovskaya, T. Herr and P. Fischer, *Angewandte Chemie*, 2015, **127**, 9912–9947.

49 J. Cao, J. Tian, J. Xu and Y. Wang, *Energy and Fuels*, 2020, **34**, 13384–13411.

50 W. Liu, Y. Liu, H. Zhang, C. Xie, L. Shi, Y. G. Zhou and X. Li, *Chemical Communications*, 2019, **55**, 4801–4804.

51 B. Yang, A. Murali, A. Nirmalchandar, B. Jayathilake, G. K. S. Prakash and S. R. Narayanan, *J Electrochem Soc*, 2020, **167**, 1–9.